Design and Fabrication of Rylene Diimide Based Active Materials, Devices and Applications

A thesis submitted by

Anamika Kalita

Roll No. 136153004

to

Indian Institute of Technology Guwahati

for the award of the degree of

Doctor of Philosophy

Centre for Nanotechnology
Indian Institute of Technology Guwahati
Guwahati - 781039
India

August-2017

Design and Fabrication of Rylene Diimide Based Active Materials, Devices and Applications

A thesis submitted by

Anamika Kalita

Roll No. 136153004

to

Indian Institute of Technology Guwahati

for the award of the degree of

Doctor of Philosophy

Centre for Nanotechnology
Indian Institute of Technology Guwahati
Guwahati - 781039
India

August-2017

Dedicated to……….

My Parents…

INDIAN INSTITUTE OF TECHNOLOGY
GUWAHATI
Centre for Nanotechnology

STATEMENT

I do hereby declare that the work contained in the thesis entitled "**Design and Fabrication of Rylene Diimide Based Active Materials, Devices and Applications**" is the result of investigations carried out by me in the Centre for Nanotechnology, Indian Institute of Technology Guwahati, Assam, India under the supervision of Prof. Parameswar Krishnan Iyer, Professor, Department of Chemistry, Centre for Nanotechnology, Indian Institute of Technology Guwahati, Assam, India. This work has not been submitted elsewhere for the award of any degree.

August, 2017 **Anamika Kalita**
IIT Guwahati

INDIAN INSTITUTE OF TECHNOLOGY GUWAHATI
Centre for Nanotechnology

CERTIFICATE

This is to certify that the work contained in the thesis entitled **"Design and Fabrication of Rylene Diimide Based Active Materials, Devices and Applications"** by **Anamika Kalita**, a Ph.D. student of Centre for Nanotechnology, Indian Institute of Technology Guwahati, for the award of degree of Doctor of Philosophy has been carried out under my supervision and this work has not been submitted elsewhere for any degree.

August, 2017
Guwahati

Prof. Parameswar Krishnan Iyer
Thesis Supervisor
Centre for Nanotechnology
Indian Institute of Technology Guwahati
Guwahati -781039
Assam, India.

Acknowledgements

First and foremost, the endless thanks goes to Almighty God for all the blessings he has sprinkled onto me, which has empowered me to write this final note of my research work. During the period of my research, I have been blessed with some extraordinary people who have turn a web of support around me. Words can never be sufficient in expressing how thankful I am to those people in my life who made this thesis possible.

I am extremely grateful to my thesis supervisor, Professor Parameswar Krishnan Iyer for his expert guidance, appreciable suggestions and constant help during my research work. I would like to thank him for encouraging me a lot in the academic life and also further extending my knowledge in many fields. It was a great pleasure for me to have a chance of working with him.

I would also like to mention my deep gratitude towards Prof. Anil Kumar Saikia, Dr. Chivukula V Sastri, Dr. Garan Kumar, Prof. Aditya Narayan Panda, Dr. Kalyan Raidongia and Prof. Mohd. Qureshi for all the support provided to me during my thesis work.

I am grateful to all faculty members in the Centre for Nanotechnology and Department of Chemistry, IIT Guwahati for their help and encouragement and also the non-teaching staff of both the Centre and Department for their technical support. I am thankful to the Central Instruments Facility (CIF) and Department of Physics, IIT Guwahati for various characterization facilities.

I take this opportunity to dedicate this work to my family members, Deuta (Dhiren Kalita), Maa (Bibharani Kalita) and my younger brother (Phanindra Kalita) for their consistent support and sacrifices throughout my research work that made me what I am today. I am grateful to my dear friend Pranjal Barman for his emotional support and cooperation that assisted me a lot to complete this thesis.

I convey my special thanks to Sameer Hussain, Akhtar Hussain Malik and Nehal Zehra for their emotional support, affection, respect, continuous encouragement, invaluable advices in my thesis work. I am fortunate to have them who helped me a lot in the research work and during ups and down of my life to get out through difficult times.

It is a pleasure to express my profound gratitude to my labmates working in synthesis lab as well as organic electronics lab, Radha bhaiya, Suresh bhaiya, Bhim bhaiya, Priyanka di, Himani di, Ekta di, Adil Afroz, Niranjan, Arvin, Sayan, Gopi, Raman, Subrata, Maimur, Debasish, Ravindra, Anamika, Ashish, Dipjyoti, Rahul, Indrani, Ramesh Babu, Ritesh, Nystha for giving me friendly atmosphere in lab and making my days memorable with them. I am thankful to my former lab members Prasanta da, Atul da, Subbarao bhaiya, Muruli bhaiya, Jupitara di, Debojit and Paran for their valuable guidance and encouragement. I am indebted to all the interns/project fellows Rajlekha, Deepika, Bikoshita, Sufiyan, Ajeet, Kamini, Sunil, Vikshit, Quammruddin, Sourav, Raj, Nayan for their love and affection.

I convey my special thanks to Sajitha, Namami, Ujjwol, Himadri, Mridusmita, Upashi, Reshma, Isha, Parthana, Bandana, Sushanta, Paban, Arnav, Sulender, Rajan, Rajarshi, Bipul da, Hemanta da, Monalisha, Romi, Pankaj, Shad, Anindya, Rather Adil for their generous support, timely suggestions and inspiration.

I would also like to express deep appreciation towards my seniors Sabera di, Ajaz bhai, Jayanta da, Dipankar da, Tridip da, Subhasish da for giving me valuable suggestions and advices.

Finally, once again I would like to thank God, family members, all well-wishers and friends for their blessings, love and wonderful support that helped me to reach my goal.

Anamika Kalita

The content of this thesis report entitled **"Design and Fabrication of Rylene Diimide Based Active Materials, Devices and Applications"** is divided into five chapters. Chapter 1 gives a brief introduction about the scope and significance of the subsequent chapters. Chapter 2 discussed the synthesis of a conjugated naphthalene diimide (NDI-CY2) derivative and its application in Organic Field-Effect Transistors (OFETs) and showing the effect of inorganic/organic polymeric dual dielectric layers on device performance. Chapter 3 discussed the development of a new conjugated naphthalene diimide (NMeCy2) derivative and its application in the field of OFETs using trilayer dielectric system. Chapter 4 described the synthesis of a histidine functionalized perylene diimide (PDI-HIS) derivative and its application in vapor mode detection of ammonia via fabricating a two electrode sensor device. Chapter 5 deals with the synthesis of a new conjugated naphthalene diimide (NDMI) derivative and its application in the detection of potent nitroexplosive picric acid both in solution as well as in vapor phase. Chapter 5 also highlighted the development of electronic prototype for visual on-site detection of nitroexplosive picric acid vapor.

Chapter I: Introduction

Chapter 1 provides a concise introduction about the concept of π-conjugated organic semiconductors and its application in organic electronic devices. They offer advantages like light weight, low cost, mechanical flexibility, possibility of fabrication on a large area and ease of solution processing compared to that of inorganic semiconductors. Extensive applications of organic semiconductors in various fields such as Organic Field-effect transistors (OFETs), Organic light-emitting diodes (OLEDs), Organic photovoltaics (OPVs), Photodetectors, Photocatalysis, Bioimaging, Sensors etc. absorbed considerable attention in recent years. Among small molecule organic semiconductors, Rylene Diimides e.g. Naphthalene Diimide (NDI) and Perylene Diimide (PDI) are excellent n-type semiconductors (electron acceptors) and have much broader applications in the field of organic optoelectronics, because of their low lying LUMO energy levels, stronger electron accepting ability, and higher stability. Furthermore, this chapter also offers a brief introduction about OFETs and Electronic sensors along with their working principle, architecture and some recent selected examples of Rylene Diimide based materials for application in both OFETs and Electronic sensors.

Chapter 2: Effect of Inorganic/Organic Dual Dielectric Layer on the Morphology and Performance of n-channel OFETs

Chapter 2 discussed the synthesis of a previously reported derivative of naphthalene diimide i.e. N,N′-bis(cyclohexyl)naphthalene diimide (NDI-CY2). Optimization of dual dielectric layers by incorporating poly(vinyl alcohol) (PVA), poly(methyl methacrylate) (PMMA), polystyrene (PS) or poly(4-vinylphenol) (PVP) in combination with Al_2O_3 were explored in this chapter. High-performance n-channel OFETs based on NDI-CY2 with low operating voltage can be successfully fabricated using four different combination of dual high-k inorganic/low-k or high-k organic polymer bilayer gate dielectric using cost-effective techniques. The use of expensive Si-substrates, SiO_2 dielectrics and Au electrodes was avoided in this study. The influence of the polymer dielectric layer on the growth morphology of NDI-CY2 and the structural characterization were investigated using atomic force microscopy (AFM) and thin film XRD analysis. The bottom-gate top-contact OFET devices fabricated on glass substrates with Al contact electrodes demonstrated excellent n-channel behavior in the presence of the Al_2O_3/PVA dual dielectric with highest electron mobility (μ_e) and I_{ON}/I_{OFF} value of 0.08 cm^2/Vs and of 10^4 respectively. Significantly improved device parameters such as a low operating and threshold voltage of 5 V and 0.5 V were obtained at 100 °C respectively with the Al_2O_3/PVA dielectric combination, which has not been realized previously with this promising molecule. The variations in the electrical characteristics of the OFET device obtained for different dual dielectric combinations have been demonstrated mainly due to the diverse properties of dielectric/NDI-CY2 interfacial layer that finally govern the accumulation of carriers and charge transport.

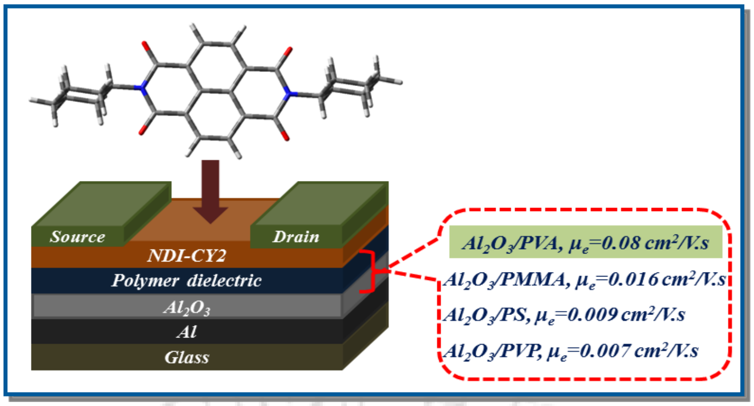

Figure 1. Schematic presentation for the effect of inorganic/polymeric dielectric layers on OFET device performance using NDI-CY2.

Chapter 3: Large-Scale Molecular Packing and Morphology Dependent High Performance Organic Field-Effect Transistor by Symmetrical Naphthalene-Diimide Appended with Methyl Cyclohexane

This chapter described the synthesis of a new derivative of naphthalene diimide appended with a methyl cyclohexane group i.e. N, N'-bis(cyclohexylmethyl)naphthalene diimide (NMeCy2). The derivative was prepared by a simple and economical method of condensation reaction. The influence of structural ordering of methyl cyclohexane appended naphthalene diimide (NMeCy2) thin films and their correlation with enhanced device performances are presented in this chapter. The vacuum-deposited thin-film microstructure and morphology of NMeCy2 have been investigated using thin-film X-ray diffraction (XRD), atomic force microscopy (AFM), and field emission scanning electron microscopy (FESEM) and were comparable with the bulk-phase crystalline structure and packing of NMeCy2. The OFET devices fabricated on a glass substrate consists of a bilayer polymer dielectric poly(methyl methacrylate) (PMMA) over poly(vinyl alcohol) (PVA) and an inorganic high-k dielectric Al_2O_3 as the third layer. NMeCy2 thermally deposited at an optimized substrate temperature (T_{sub}) of 60 °C displayed excellent molecular packing over a large area that resulted in the improved field-effect performance with electron mobility (μ_e) value of 0.6 cm^2/Vs and current on/off ratio (I_{ON}/I_{OFF}) of 10^6 via modifications in dielectric configuration. Furthermore, the device afforded an unprecedented threshold voltage of 5.23 V with this material. We have been successful in developing a facile, reliable, and cheap method to tune the dielectric features which can culminate in improved field-effect transport properties.

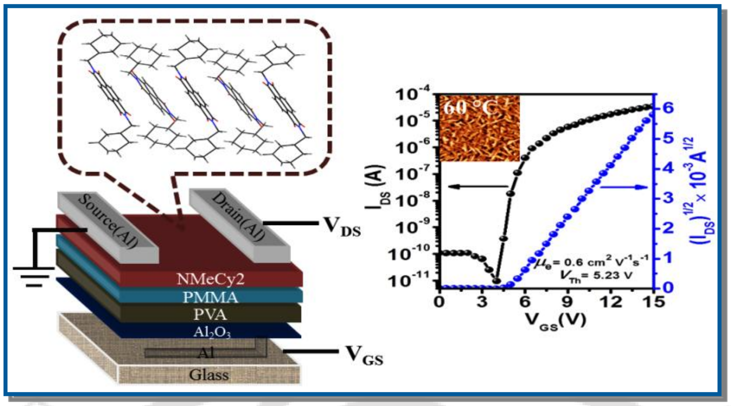

Figure 2. Schematic presentation showing the effect of molecular Packing and morphology on the performance of OFETs by using symmetrical naphthalene diimide i.e. NMeCy2 appended with methyl cyclohexane

Chapter 4: Vapor Phase Sensing of Ammonia at Sub-ppm Level Using Perylene Diimide Thin Film Device

Chapter 4 described the synthesis of a histidine substituted perylene diimide derivative i.e. PDI-HIS and its application in sensing ammonia (NH_3) vapors. A new and efficient platform for the vapor phase detection of NH_3 using a two terminal sensor device based on PDI-HIS nanostructures fabricated on a simple glass substrate by the drop-casting method has been developed in chapter 4. The sensitive detection and quantification of NH_3 vapors was carried out by monitoring the changes in its current intensity at room temperature under ambient conditions. The sensing parameters viz. sensitivity, selectivity, recyclability, response/recovery time and stability were studied that revealed the excellent performance of the device with a very low detection limit of 0.56 ppm for NH_3 which is much lower than the maximum permissible limit set for NH_3 (25 ppm) for prolonged exposure. We have also demonstrated that the molecular assemblies of PDI-HIS nanostructures, redox potential and ionic groups at the imide position are key aspects for the remarkable response of the device towards NH_3. The thin film morphological variations of the drop casted PDI-HIS films before and after exposure to NH_3 vapors are characterized by FESEM and TEM confirming the diffusion/adsorption of the NH_3 vapors. Furthermore, control sensing experiments were also performed using alkyl substituted PDI (PDI-n-octyl) demonstrated that presence of histidine groups at the imide position of PDI-HIS drastically affects the solid-state aggregation mode as well as redox potential that ultimately enhances the sensing response of the device. Thus, the ability of the as-fabricated sensor device to detect NH_3 vapors at room temperature and under ambient conditions with high sensitivity and selectivity, fast response/recovery time, recyclability and low fabrication cost makes the protocol economical and feasible for potential applications under chemical, biomedical and competitive environmental conditions.

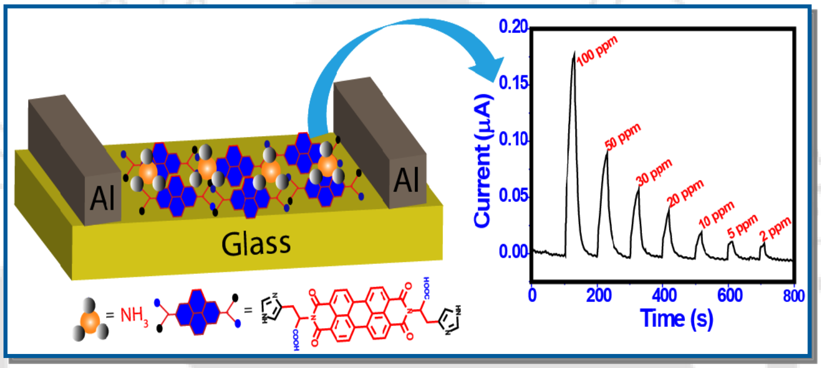

Figure 3. Schematic presentation for vapor phase sensing of NH_3 using perylene diimide derivative i.e. PDI-HIS by fabricating a two terminal sensor device.

Chapter 5: Anion-Exchange Induced Strong π-π Interactions in Single Crystalline Naphthalene Diimide for Nitroexplosive Sensing: An Electronic Prototype for Visual On-Site Detection

Chapter 5 elucidated the synthesis of a new crystalline cationic derivative of naphthalene diimide i.e. N, N′-bis(3-imidazolium-1-ylpropyl)-naphthalenediimide diiodide (NDMI) and its application in detection of most widespread nitroexplosive and highly water soluble pollutant picric acid (PA) both in aqueous medium as well as vapor phase. Synthesized NDMI derivative displayed optical, electrical, and visual changes exclusively for the nitroexplosive PA due to strong π-π interactions, dipole charge interaction and a favorable electron transfer process facilitated by coulombic attraction. The sensing mechanism and interaction between NDMI with PA is demonstrated via X-ray diffraction analysis, ^1H NMR studies, cyclic voltammetry and fluorescence spectroscopy. Single crystal X-ray structure of

NDMI revealed the formation of self-assembled crystalline network assisted by noncovalent C−H···I interactions that get disrupted upon introducing PA as a result of anion exchange and strong π-π stacking between NDMI and PA. Morphological studies of NDMI displayed large numbers of single crystalline microrods along with some three-dimensional (3D) daisy-like structures which were fabricated on Al-coated glass substrate to construct a low-cost two terminal sensor device for realizing vapor mode detection of PA at room temperature and under ambient conditions. Finally a simple, portable and cost-effective electronic prototype was developed for visual on-site detection of PA vapors in order to prevent terrorist threats rapidly under very realistic conditions.

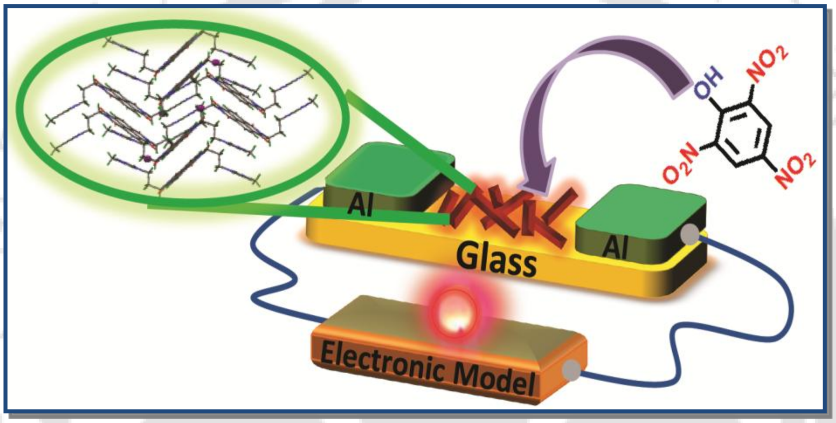

Figure 4. Schematic presentation for the visual on-site detection of nitroexplosive PA using conjugated naphthalene diimide derivative NDMI.

Conclusion and thesis overview

In conclusion, rylene diimide derivatives were synthesized using simple condesation reaction. The derivatives NDI-CY2 and NMeCy2 were successfully utilized for the OFET application using simple, cost effective fabrication techniques. The conjugated perylene diimide derivative PDI-HIS was employed for the detection of NH_3 vapors via fabricating a simple two terminal sensor device. A new derivative of naphthalene diimide i.e. NDMI was developed for its application in detection of nitroexplosive PA both in solution and vapor phase. Furthermore, an economical and portable electronic prototype was established for visual and on-site detection of PA vapors under exceptionally realistic conditions.

Chapter 1: Introduction

Page No

Chapter 2: Effect of Inorganic/Organic Dual Dielectric Layer on the Morphology and Performance of n-channel OFETs

Chapter 3: Large-Scale Molecular Packing and Morphology Dependent High Performance Organic Field-Effect Transistor by Symmetrical Naphthalene-Diimide Appended with Methyl Cyclohexane

Chapter 4: Vapor Phase Sensing of Ammonia at Sub-ppm Level using Perylene Diimide Thin Film Device

Chapter 5: Anion-Exchange Induced Strong π-π Interactions in Single Crystalline Naphthalene Diimide for Nitroexplosive Sensing: An Electronic Prototype for Visual On-Site Detection

Chapter 1

INTRODUCTION

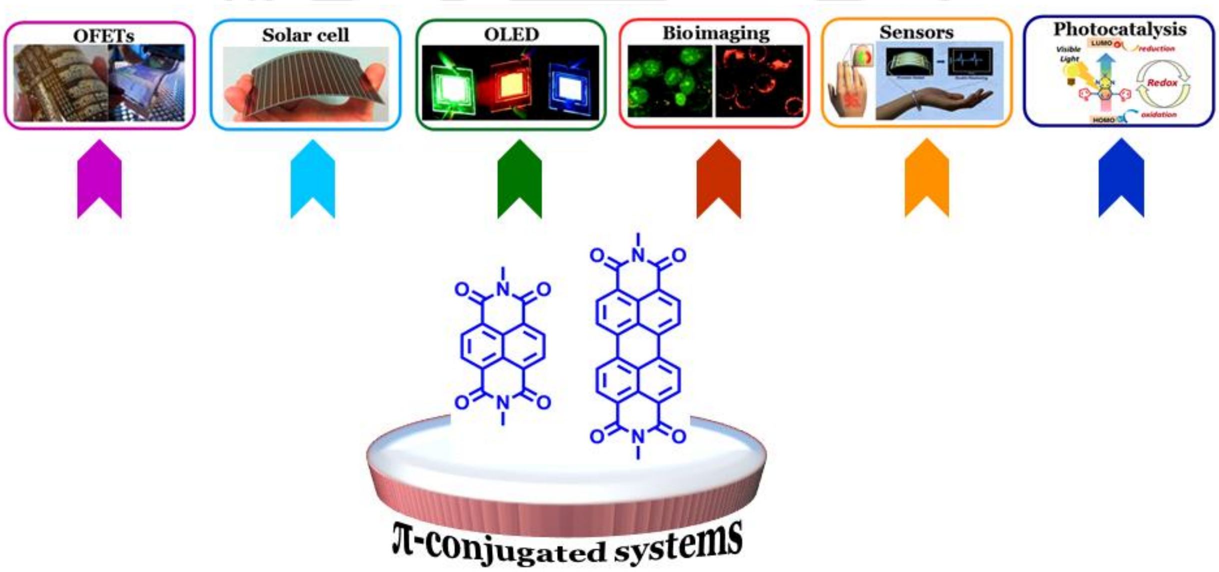

1.1 Organic semiconductor

The concept of π-conjugated organic systems have fascinated considerable attention as innovative materials for the development and advancement of next generation electronics,[1] i.e., organic electronics[2] after the discovery of conducting polyacetylene in 1977 by Shirakawa, MacDiarmid, and Heeger[3] (**Figure 1.1**). These three scientists recognized that the molecular arrangement in organic semiconductors must contain alternating single and double/triple bonds that permit the formation of delocalized electronic states which is the stimulating force for the electrical conductivity.

Figure 1.1 Scientists who received the 2000 Nobel Prize for the discovery of electrical conductivity in doped Polyacetylene.

The structural versatility in organic semiconductors allow for the fusion of functionality via molecular approach that completely separate the organic electronics from conventional inorganic ones. This flexibility stimulates to a new-fangled era in the design of organic electronic devices. So far, large number of π-conjugated semiconducting materials that have either been discovered or produced, create an interesting collection of π-conjugated organic systems (**Figure 1.2)** for use in electronics.[4-11] Nevertheless, the environmental stability, lower mobility, lack of evidence concerning structure-property relations, the essential chemical features behind the structural strategy and realization of desired effects are certain major challenges for further upgrading of organic electronics.[12] In general a conjugated pi system is the fundamental requirement for both organic polymers as well as small molecules to conduct charges under the control of an electric field. Molecular conjugation stands as an essential property for efficient passage of electronic charges along the core of conjugated molecule.[13]

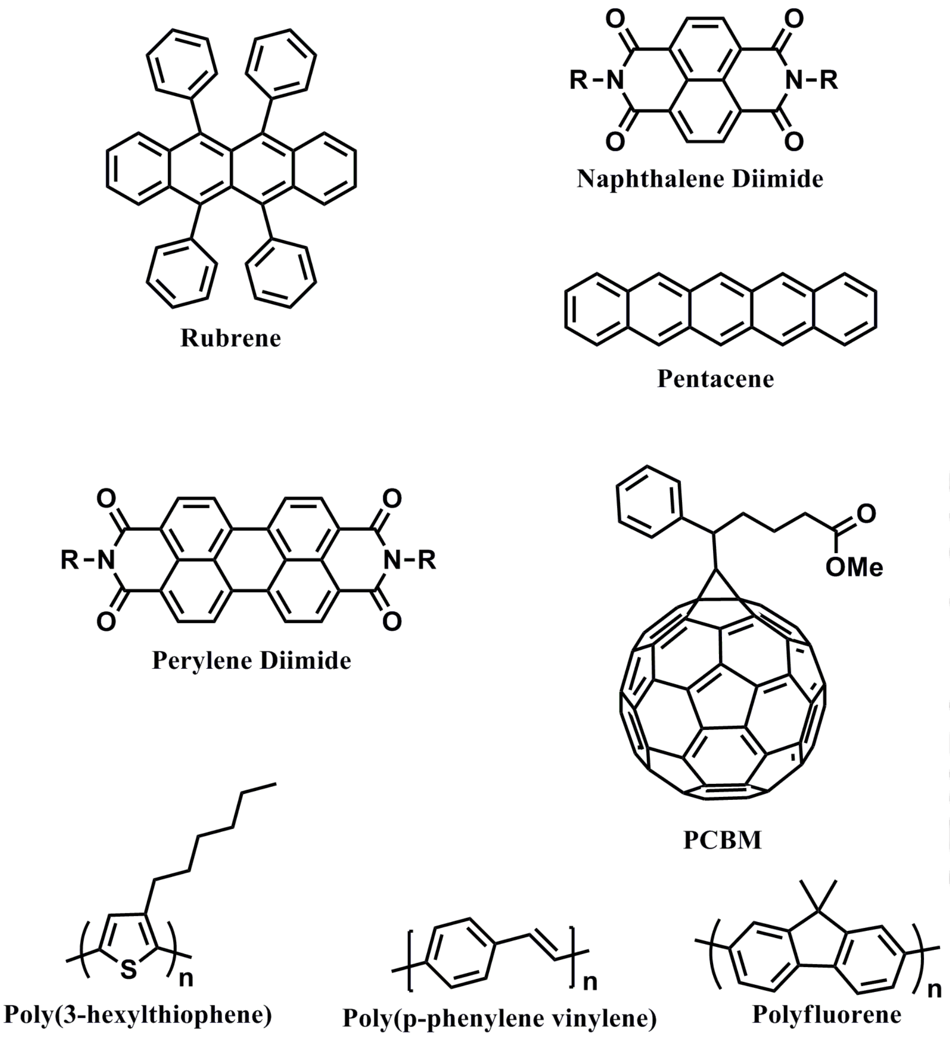

Rubrene

Naphthalene Diimide

Pentacene

Perylene Diimide

PCBM

Poly(3-hexylthiophene)

Poly(p-phenylene vinylene)

Polyfluorene

Figure 1.2 Chemical structures of organic semiconductors.

1.2 Organic semiconductor devices

Organic semiconductors are an alternative to conventional inorganic semiconductors and offer advantages e.g. light weight, low cost, mechanical flexibility, possibility of fabrication on a large area and ease of solution processing. Organic semiconducting materials have extensively applied in numerous fields including Organic Field-effect transistors (OFETs), Organic light-emitting diodes (OLEDs), Organic photovoltaics (OPVs), Photodetectors, Photocatalysis, Bioimaging, Sensors etc[14-22] (**Figure 1.3**). In general, development of high-performance electron transporting organic materials has lagged behind that of hole transporting materials despite their importance in various fields.[23,24] Even after their importance in various fields, organic semiconducting materials suffer from disadvantages like low mobility, environmental stability etc. which limit their interest academically as well as commercially. Developing new materials, device engineering with stability and enhanced performances are some of the important factors to overcome these challenges.

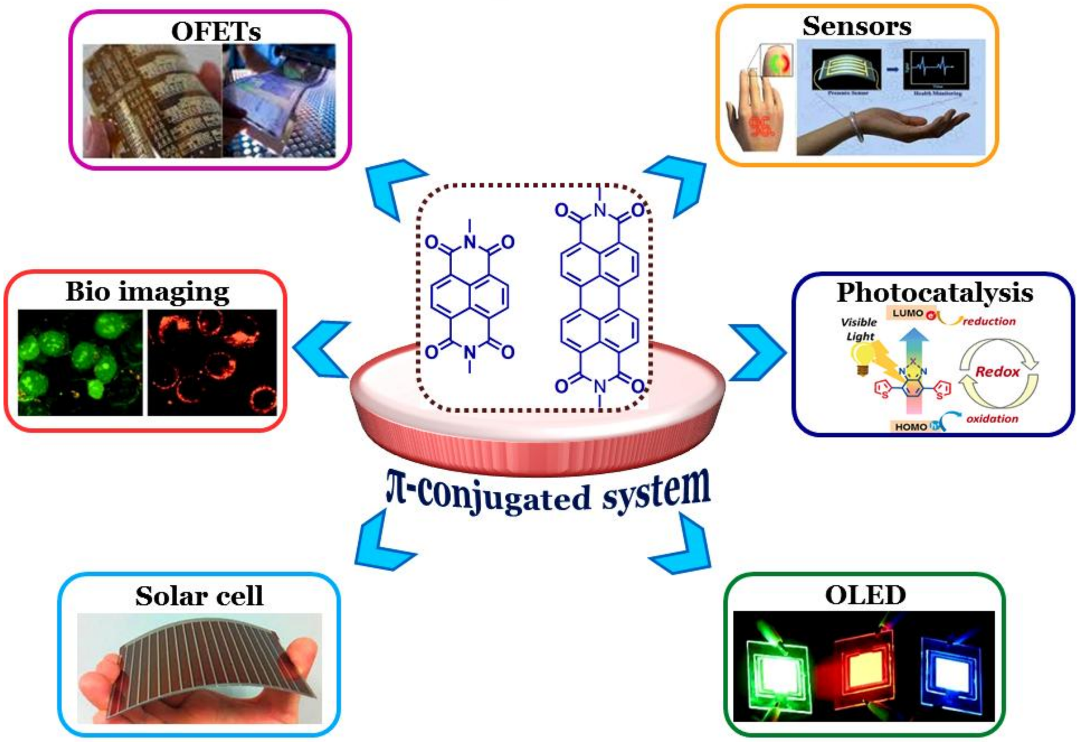

Figure 1.3 Various applications of π-conjugated systems.

1.3 Small molecule organic semiconductors

Commonly organic semiconductors come in two categories: conjugated polymers and small molecules. Remarkable advancement in organic chemistry has endorsed for the synthesis of an extensive series of π-conjugated materials with smart optoelectronic outcomes. Small organic molecules offer several inherent advantages over conjugated polymers in optoelectronic applications. They provide immense structural possibilities for refining a broad range of properties like well-defined structure and high purity along with molecular functionality, rigidity, strong intermolecular interactions, readily self-organize into well-ordered polycrystalline films upon deposition[13] for the construction of the desired devices with better performances etc. Via varying the chemical structures and functionalities, the molecular properties of such materials can easily be fine-tuned.[25] Furthermore, small molecule organic semiconductors as active layer in electronic devices have recently been received a significant attention from the perspective of potential technological applications.

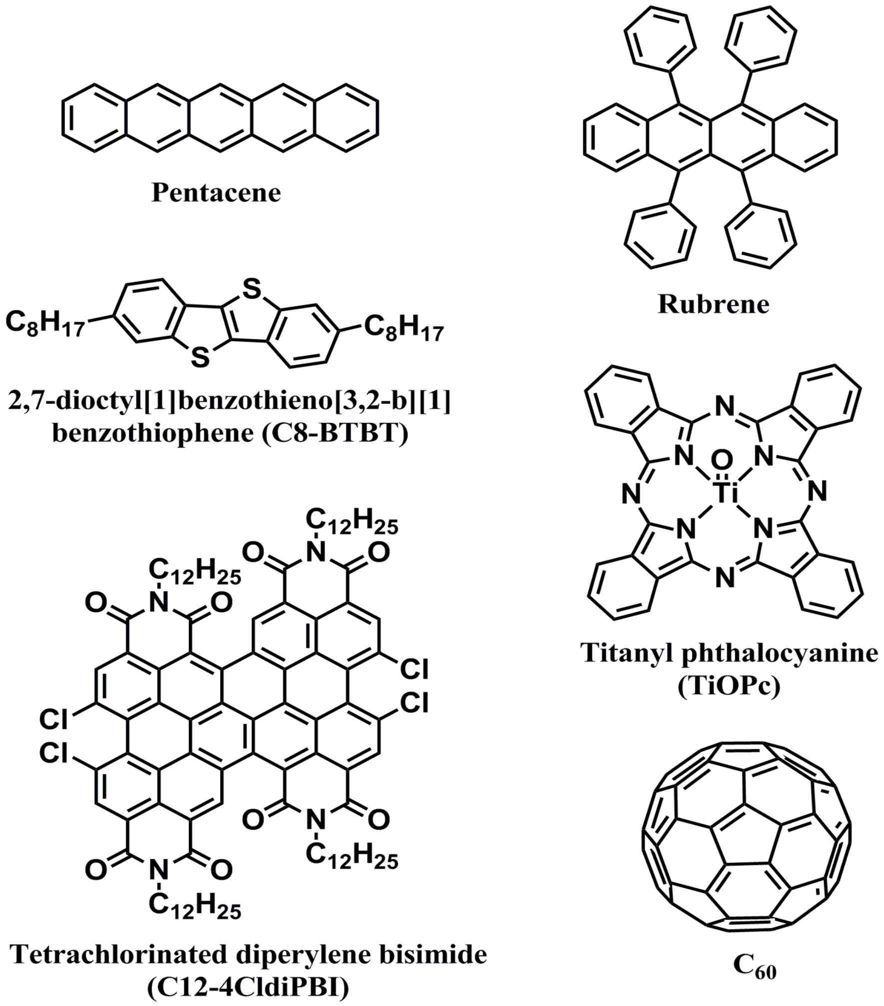

Figure 1.4 π-conjugated small molecules reported to have the highest mobilities.

Advancement of high performance organic semiconductors has been of intensive research focus[12,26,27] since the introduction of polythiophene in OFETs for the first time in 1986.[28] Indeed, till now, π-conjugated structures that are listed to have highest charge transport properties are small molecules[29] such as pentacene[30] (μ=40 cm^2/Vs), rubrene[31] (μ=43 cm^2/Vs), 2,7-dioctyl[1]benzothieno[3,2-b][1]benzothiophene (C8-BTBT)[32] (μ=31.3 cm^2/Vs), titanyl phthalocyanine (TiOPc)[33] (μ=10 cm^2/Vs), tetrachlorinated diperylene bisimide (C12–4CldiPBI)[34] (μ=4.65 cm^2/Vs) and C_{60}[35] (μ=11 cm^2/Vs) **(Figure 1.4)**.

1.4 Rylene Diimide based small molecules

Among small molecule organic semiconductors, Rylene (**R**) are extensively studied class of hydrocarbon families that are formed by connecting the peri positions of naphthalene (**R-1**).[36] Rylene Diimides (**RD**) have two diimide functionality at the end positions of rylene. Their conjugated cores are shown in **Figure 1.5**. RD are widely employed as organic semiconductors and dyes in various applications because of their large absorption coefficient, strong fluorescence, and high chemical as well as thermal stabilities.[37,38] Naphthalene Diimide, RD-1 (NDI) and Perylene Diimide, RD-2 (PDI) are excellent n-type semiconductors (electron acceptors), although only a little research has been conducted for higher rylene derivatives because the synthesis is complicated for these long conjugated compounds.[39,40] Rylene Diimides with two electron-withdrawing imide groups have much broader applications than their rylene counterparts in the field of organic electronics, because of their low lying LUMO energy levels, stronger electron accepting ability, and higher stability.[36]

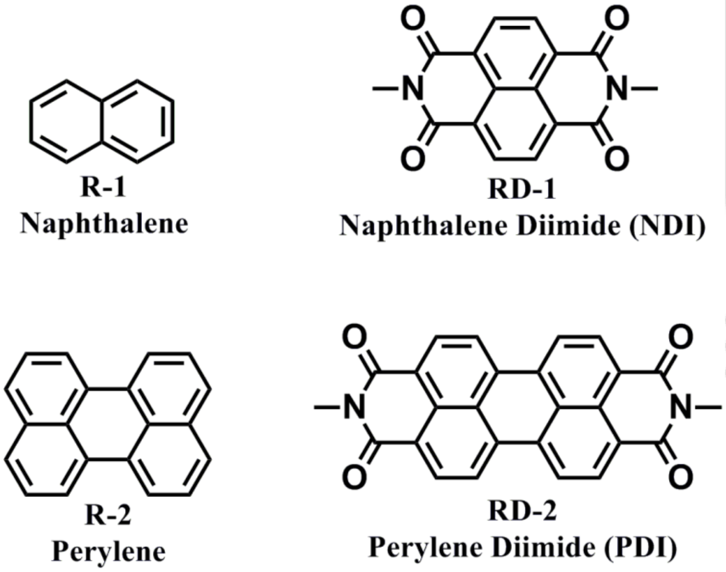

R-1
Naphthalene

RD-1
Naphthalene Diimide (NDI)

R-2
Perylene

RD-2
Perylene Diimide (PDI)

Figure 1.5 Structures of Rylene (R) and Rylene diimides (RD).

The content of present thesis basically emphasis on two immense area of research i.e. ***Organic field-effect transistors (OFETs)*** and ***Electronic sensors*** that can be discussed below:

1.5 Organic Field-Effect Transistors (OFETs)

OFETs have received extensive research attention in the past decade due to their potential applications in organic integrated circuits such as radio frequency identification (RFID) tags, smart cards, and organic active matrix displays etc.[41,42] With their mobilities approaching amorphous silicon based transistors their practical applications seems not very far. Efforts have been devoted to improve device performance and stability to reduce the power consumption and fabrication cost via developing novel organic semiconductors, optimizing device fabrication techniques etc. Typical OFETs are devices comprising of an organic semiconductor active layer, a gate insulator layer, and three terminals, viz., gate, source and drain electrodes of width *W* (channel width) separated by a distance *L* (channel length) that are in contact with the semiconducting layer. The basic components used for construction of an OFET are shown in **Figure 1.6**.

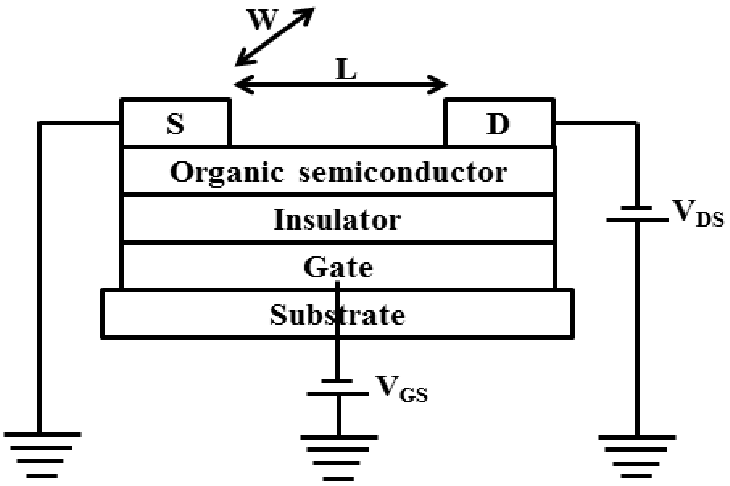

Figure 1.6. Schematic of a typical OFET structure.

1.5.1 Different architectures of OFETs

Depending on the relative position of the contacts and the dielectric/semiconductor layers, several device architectures have been proposed for the fabrication of OFETs such as Top Gate Bottom Contact (TGBC), Top Gate Top Contact (TGTC), Bottom Gate Bottom Contact (BGBC) and Bottom Gate Top Contact (BGTC) (**Figure 1.7**), but the process of operation is basically same. BGTC and TGBC configurations provide better performances than TGTC and BGBC due to the large charge injection areas and favored injection pathways between the organic semiconductor and the electrodes which leads to lower contact resistance.

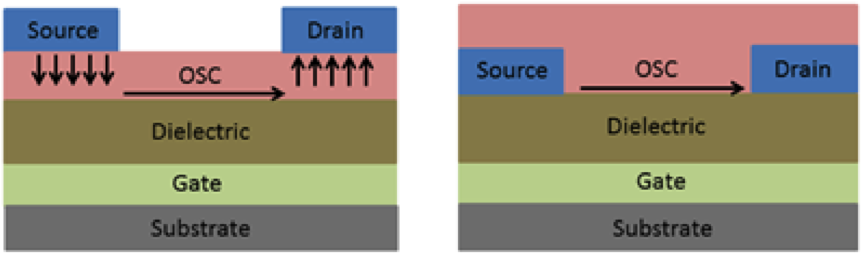

Bottom-Gate Top-Contact (BGTC) Bottom-Gate Bottom-Contact (BGBC)

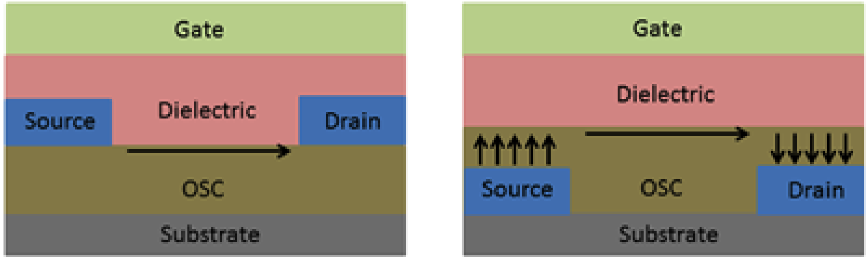

Top-Gate Top-Contact (TGTC) Top-Gate Bottom-Contact (TGBC)

Figure 1.7 Different configurations of OFETs.

1.5.2 Operating principle of OFETs

Two major processes have been involved in operation of OFETs; viz. charge injection and charge transport, at the electrode/organic layer interface and the dielectric/organic layer interface. The current between the drain and source electrodes is modulated by the applied gate voltage. When no gate voltage is applied, the drain current is very low and the transistor is normally in off state. When the gate voltage increases, a layer of mobile charges can accumulate at the dielectric/organic layer interface and form a conductive channel. Due to the increased charge carriers in the channel, the current flows and the transistor is therefore in the on state. [43]

1.5.3 Characterization of OFETs

OFETs can be characterized by the output plot (**Figure 1.8a**) that shows the gate modulating source-drain current (I_{DS}) and the transfer plot (**Figure 1.8b**) that revealed information about the important device parameters such as field-effect mobility (μ), threshold voltage (V_{TH}), current on/off ratio (I_{ON}/I_{OFF}), sub-threshold swing (SS) etc.[44]

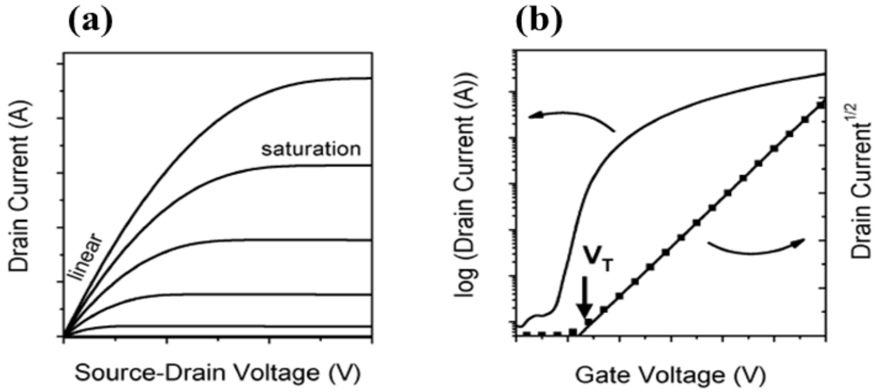

Figure 1.8 General characteristic curves of OFETs (a) Output plot and (b) Transfer plot.

1.5.4 Important parameters of OFETs

Field-effect mobility (µ)*:* The field-effect mobility measures the average charge carrier drift velocity per unit electric field.

In saturation regime (at high V_{DS} ($>V_{GS}-V_{TH}$)) and in linear regime (at low V_{DS} ($<V_{GS}-V_{TH}$)), µ (which has units of cm^2/Vs) can be calculated from the following eqns:

$$I_{DS,\,Sat} = \frac{\mu C_i W}{2L}(V_{GS}-V_{TH})^2$$

$$I_{DS,\,Lin} = \frac{\mu C_i W}{L}(V_{GS}-V_{TH})V_D$$

Where, V_{DS} is the drain voltage with the source electrode grounded, W and L are the channel width and length, respectively, and C_i is the capacitance per unit area of the dielectric layer.

Current on/off ratio (I_{ON}/I_{OFF}): The current on/off ratio is defined as the drain-source current ratio between the on and off states of transistor.

Threshold voltage (V_{TH}): The threshold voltage is the minimum amount of voltage required to make a conducting channel between source and drain.

Sub-threshold swing (SS): The sub-threshold swing is a measure of how rapidly the devices switches from the off state to the on state in the exponential current increase region and is defined by SS=V_G/(log I_D).[45]

1.5.5 n-channel and p-channel OFETs

OFETs can be classified as n-channel or p-channel depending on majority charge carriers (electrons or holes) (**Figure 1.9**). If the Fermi level of the source/drain electrode is close to the highest occupied molecular orbital (HOMO) level of the organic semiconductor, then positive charges/holes can be extracted by the electrodes via applying a voltage between drain and source and is defined as p-channel OFET. While, in n-channel OFETs, if the Fermi level of the source/drain contact is close to the lowest unoccupied molecular orbital (LUMO) level of the semiconductor, then negative charges/electrons can be released by the electrodes through application of voltage between drain and source.[46] For example, when negative voltage is applied to the gate electrode, hole carriers in the organic semiconductor layer become collected at the interface of the gate dielectric, and hence, hole migration takes place from the source to the drain electrode; this state corresponds to the on-state of transistor. This category of device is called p-channel device. Likewise, application of positive voltage to the gate electrode causes electron transport in the case of n-channel device. The current flow can be controlled by the magnitude of both the gate voltage and the source/drain voltage.

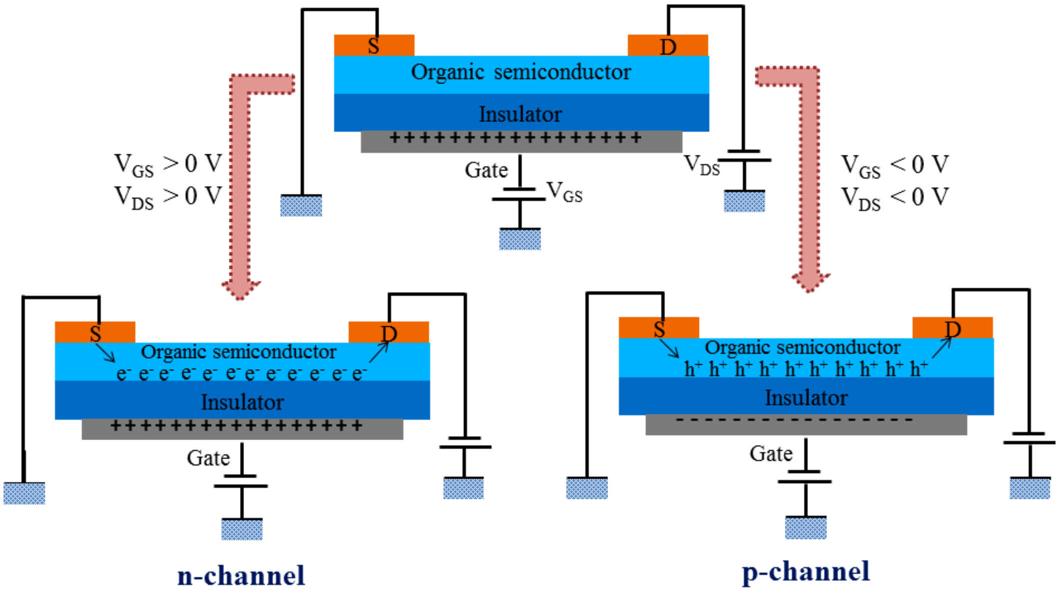

Figure 1.9 Operation in (a) n-channel and (b) p-channel OFET.

However, most of the organic semiconductors explored so far are p-type mainly because of air stability and have relatively high mobility when they are used in OFETs. Unlike p-type semiconductors, most n-type semiconductors are sensitive to air and moisture. Furthermore, n-type semiconductors have relatively low field-effect mobilities. Although most of the work to date has focused on p-type organic materials, however high performance n-type semiconductors are important components of p-n junction diodes, bipolar transistors, and complementary circuits.[47]

1.6 Rylene Diimide as active layer in OFETs (Some selected examples)

In 2008, Shukla *et al.* reported one of the highest electron mobility near 6 cm^2/Vs among all n-type organic semiconducting thin films with vapor deposited compound **1.10a**. The device was fabricated on an octadecyl trichlorosilane (OTS) modified Si/SiO_2 substrate with Au contacts under Ar atmosphere with I_{ON}/I_{OFF} as high as 6×10^8 and V_{TH} of 58 V.[48] Again Mori and co-workers in 2013 reported an OFET device with similar type of material under same device fabrication condition and reported the carrier mobility to be 0.52 cm^2/Vs under vacuum and in air the mobility drops to 0.11 cm^2/Vs with I_{ON}/I_{OFF} value of 10^6 and V_{TH} increases from 44 to 61 V. Both the groups demonstrated the difficulties in attaining small V_{TH} values along with operating voltage in this type of material.[49] Iyer *et al.* in 2014, reported development of a low cost OFET device with **1.10b** showing electron mobility as high as 1.0 cm^2/Vs, where they have utilized low cost device components with PVA dielectric without any buffer layer or PVA cross-linkers.[50] In 2000, Dodabalapur and co-workers reported the OFET device of **1.10c** with mobility up to 0.1 cm^2/Vs and I_{ON}/I_{OFF} ratio above 10^5 measured in the saturation regime, for operation in air after deposition at 70 °C. SiO_2 dielectrics, and gold source and drain contact electrodes were used for fabricating the device.[51] In 2013, Wurthner *et al.* reported single crystal OFET device using **1.10d** on an octadecyl triethoxysilane (OTES) modified Si/SiO_2 substrate with gold contacts. These devices displayed excellent n-channel behavior with mobility of 8.6 cm^2/Vs, V_{TH} of about 9 V and I_{ON}/I_{OFF} of 10^7 in air. The dense packing with strong intermolecular interactions not only along the direction of charge transport but also along the injection layer are the key parameters for its excellent operational stability in air.[52] Zhu *et al.* in 2011, reported a fused core-expanded derivative **1.10e** with sulfur heterocycles and end-capped with electron-withdrawing side groups. The solution processed OFET devices operated as n-channel transistors and displayed the maximum electron mobilities of ≥0.19 cm^2/Vs, $I_{ON}/I_{OFF}>10^5$, and $V_{TH}<15$ V on OTS modified SiO_2 in air.[53] In 2012, Zhang and co-workers investigated

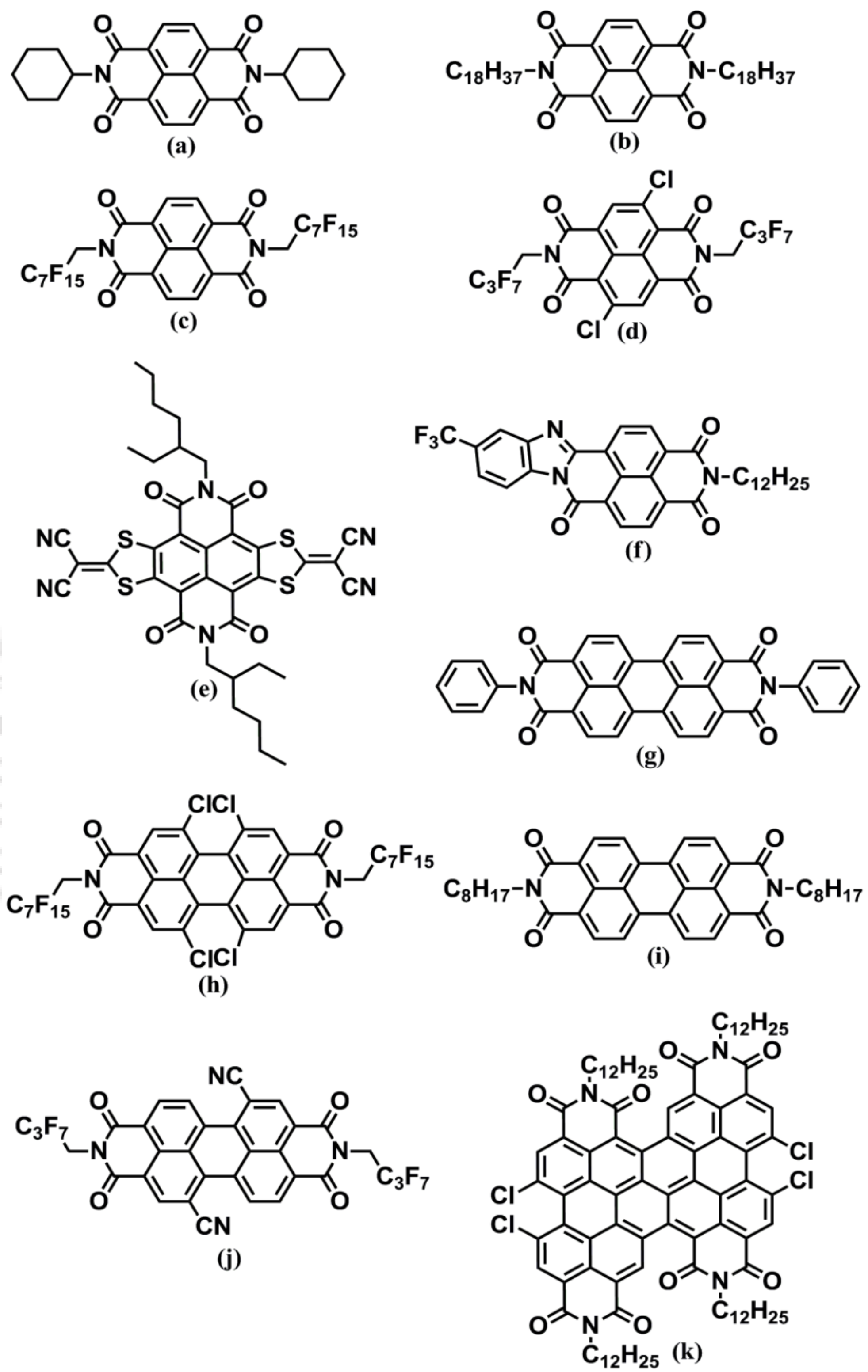

Figure 1.10 Selected examples of rylene diimide derivatives used as active materials for OFETs application.

the n-type OFET device performance of asymmetrically substituted NDI derivative **1.10f**. The vacuum deposited OFET devices fabricated on *β*-phenethyl-trichlorosilane (*β*-PTS) pre-treated SiO_2/Si substrates with Ca and Cu as the drain and source electrodes displayed highest mobility of 0.10 cm^2/Vs and I_{ON}/I_{OFF} ratio of about 10^3. But the best device properties were observed at a substrate temperature of 80 °C.[54] Among PDI based OFET devices, the first n-channel field-effect transistor was reported by Horowitz *et al*. in 1996 fabricated by using derivative **1.10g**, which only revealed a lower electron mobility of 10^{-4} cm^2/Vs.[55] In 2014, Wang *et al.* demonstrated single-crystal microribbons of core-tetrachlorinated PDI derivative **1.10h** produced by physical vapor transport technique, and the transistors made-up on a OTS-modified SiO_2 using Au as source and drain contact electrodes exhibit an electron mobility up to 1.43 cm^2/Vs in air and I_{ON}/I_{OFF} ratio of 10^7, which are correlated with its closest packing arrangement for the distorted molecular skeletons as well as for the alternately overlapped fluorinated alkyl side chains.[56] Jankauskas *et al.* in 2011, reported OFET device fabricated using a vacuum-deposited film of compound **1.10i** as the active layer demonstrated electron mobility as high as 1.7 cm^2/Vs tested under vacuum or reducing atmosphere conditions.[57] Morpurgo *et al.* reported in 2009 that the Single-crystal OFET device with rectangular crystals of compound **1.10j** obtained via physical vapor transport onto heavily doped Si/SiO_2-PMMA substrates with pre-fabricated Ti/Au as source-drain electrodes. The higher electron mobility of ~1 to 6 cm^2/Vs were achieved for single crystal OFET and ~0.1 to 0.6 cm^2/Vs for thin film.[58] In 2012, Wang *et al.* designed an OFET device based on individual micro or nanoribbons of compound **1.10k** grown by solution processed technique which presented an excellent electron mobility of 4.65 cm^2/Vs fabricated on an OTS-treated Si/SiO_2 substrates and Ag as source and drain electrodes[59] **(Figure 1.10)**.

1.7 Electronic sensors

Sensor technologies have appeared as dynamic approaches for numerous applications, including public safety, environmental protection, homeland security, and medical diagnostics.[60-66] Miniaturized devices capable of sensing volatile organic chemicals (VOCs) are extremely desirable because of their simplicity, portability and cost-effective approach compared to already existing techniques. To develop a suitable hand-held, portable sensors that are capable of recognizing as well as quantifying the analyte of interest, in an interfering environment are commercially highly beneficial.[67] Electronic sensors have experienced incredible attention owing to their easiness in the detection or analysis of information of various analytes through electrical signals[68] i.e. they converted a chemospecific sensing event into a voltage or current output. Moreover, the development of a semiconductor device is simple, since the signal does not require intricate detection kits. Electronic sensors are devices incorporated with an active layer having **receptor unit**, which transforms a chemical interaction into an electrically analyzable signal via **transducer unit** (**Figure 1.11**).

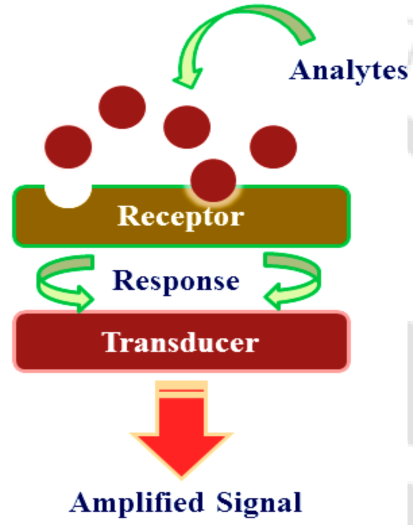

Figure 1.11 Working principle of chemiresistor-type sensor device.

1.7.1 Classification of sensors

Depending on the method of transduction sensor technologies can be differentiated as electrical, optical, thermal or gravimetric. The electrical sensor can be further subdivided by device configuration into chemiresistors, chemicapacitors, OTFTs etc. The optical class covers optical fiber sensors, surface plasmon resonance (SPR) sensors etc. The gravimetric group consists of surface acoustic wave (SAW) sensors, quartz crystal microbalances (QCM) and microcantilever sensors **(Figure 1.12)**.[69]

Among electronic sensor devices, three-terminal OTFTs and two-terminal chemiresistors are the most favorable candidates for the advancement of cost-effective, portable, low power consuming devices for ultrasensitive and selective applications in chemical, biological and physical monitoring.[70] Such ultrasensitive sensors can be useful for detecting traces of various toxic gases and volatile organic compounds (VOCs) even at remote locations.[71,72]

These chemosensors represents the simplest of vapor/gas sensors in that their chemical interaction is directly transduced into electrical output. In such sensing devices modulation in resistance, voltage, capacitance and current indicate the presence of a specific analyte. The sensitivity and selectivity of sensors depends on design of the materials, which will change their electronic properties when in contact with volatile species.[69]

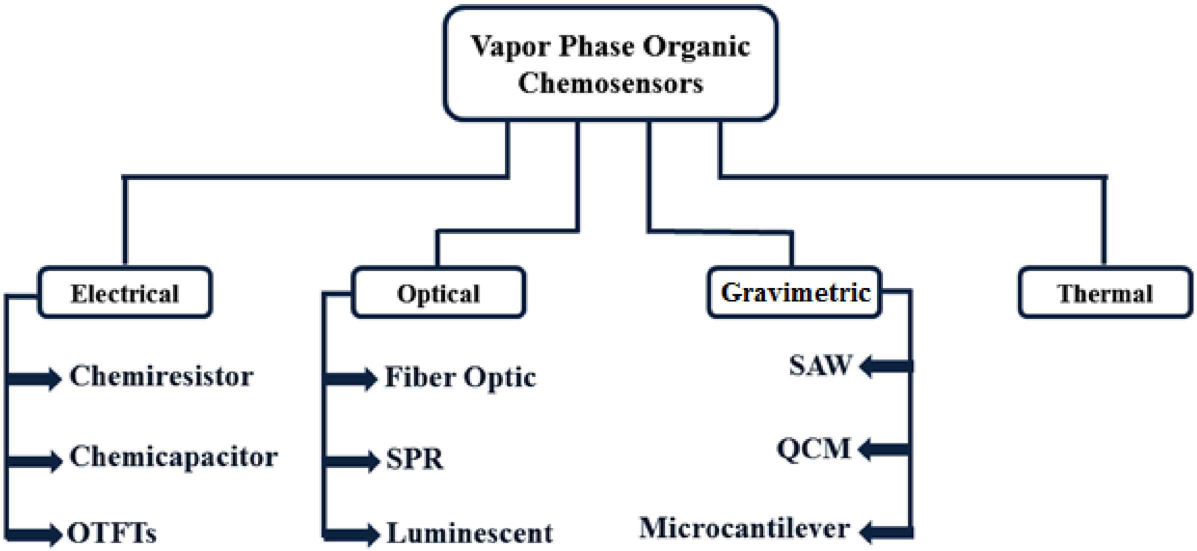

Figure 1.12 Classification of different sensor technology used for chemical vapor detection.

1.7.2 Chemiresistor-type sensor device

Chemiresistor-type sensor device represents the most common and simplest form that incorporates organic semiconductors. A chemiresistor-type sensor is a thin-film device and the detection of analytes in such devices is based on the variation in electrical behavior of organic semiconductors through partial charge transfer or doping effect. While the specificity of the sensor device for a particular analyte can be achieved by incorporating suitable receptor sites on semiconductor active layer.[73,74] Mostly, chemiresistor-type sensor device contains of pair of electrodes that form contacts with the organic semiconductor layer, which is deposited on an insulating surface viz. glass, plastic etc. (**Figure 1.13**) since the devices operate in direct current mode.[69]

As the new developments in sensor technology emerge, vapor phase chemical sensors are gradually finding applications in increasingly diverse areas. Vapor phase sensors have the advantages of utilizing nondestructive, noninvasive ways of detection with the potential for high degree of sensitivity.

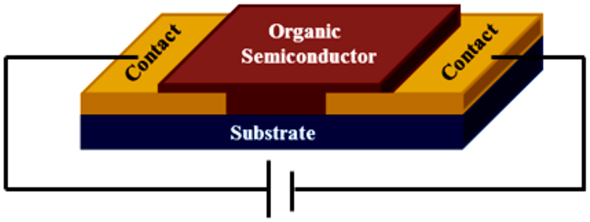

Figure 1.13 Schematic of a simple organic chemiresistor-type sensor device.

1.7.3 Advantages of organic semiconductor based chemiresistor-type sensors

The main advantages of using organic semiconductor based chemiresistor-type sensors are their ease of fabrication, which particularly makes them cost effective. Additionally, they have the advantages of operating under room temperature while metal-oxide semiconductor chemiresistors required temperature of 200 to 500 °C for regular operation, which consumes considerable amount of power. Chemiresistor-type sensors with organic semiconductors operate via multiple sensing mechanisms, and may therefore find complementary uses as compared to existing categories of chemiresistors. Several common sensing mechanisms predominate in chemiresistive devices, including charge transfer, adsorption/desorption at the surface, schottky barrier modulation, dipole-dipole interaction etc.[75] Organic semiconductor based chemiresistor allowing the sensors to regenerate quickly via adsorption/desorption process i.e. they have fast response and recovery time.[76]

1.8 Rylene Diimide as active layer in electronic sensor devices (Some selected examples)

Zang *et al.* in 2007, demonstrated the hydrazine sensing property of compound **1.14a** and **1.14c** via measuring the conductivity changes upon exposure to hydrazine vapor fabricating a simple two terminal sensor device.[77,78] Wei and co-workers in 2011, reported a conductometric gas sensors composed of single-crystalline micro/nanostructures of compound **1.14b**, which selectively performed detection of NH_3 gas.[79] Zang *et al.* in 2016, reported 1-methylpiperidine substituted PDI compound **1.14d** possessing extraordinarily high conductivity which enables application in chemiresistive sensor device. The nanoribbons of

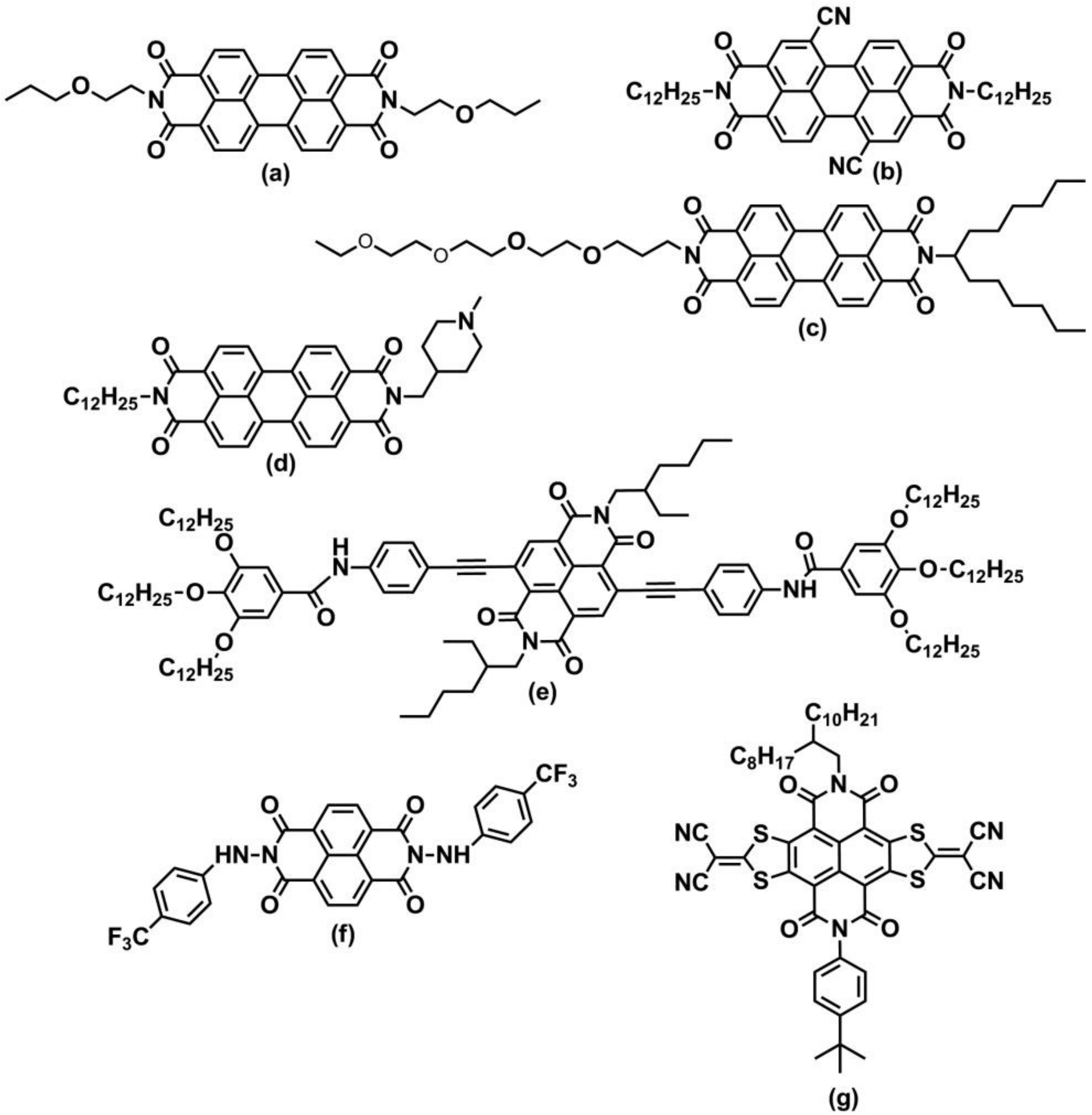

Figure 1.14 Selected examples of rylene diimide derivatives used as active materials for sensor device application.

PDI derivative demonstrated highly sensitive response to H_2O_2 vapor through oxidation, rather than dipole moment interaction as in the case of common liquid vapor, with lowest detected concentration of 0.6 ppm.[80] In 2016, Fang and co-workers designed a fluorescent derivative of NDI compound **1.14e** and established a gel networked fibrillar structure that sensitively detects aniline vapor.[81] In 2010, Mukhopadhyay and co-workers[82] reported sensing of cyanide via fabricating a two terminal sensor device using compound **1.14f**. Similar group in 2013, established differential stoichiometric response to fluoride anions using the same two terminal sensor device.[83] Zhu *et al.* in 2014 demonstrated the specific and reproducible HCl, NO_2, and NH_3 detections utilizing compound **1.14g** via a gas-phase reaction assisted detection approach[84] (**Figure 1.14)**.

1.9 Objective and summary of the thesis work

The main highlight of the thesis work was to design and fabricate Rylene Diimide (RD) based active materials for device applications. Among various rylene diimides, naphthalene diimide and perylene diimide were chosen due to their ease of synthesis and functionalization, formation of good molecular ordering in solid state, high electron accepting ability, excellent optical and redox properties and high thermal stability. By using these two materials with various functionalities at imide position, high performance OFET devices were fabricated and two terminal sensor devices were utilized for vapor mode detection of chemical analytes like ammonia, explosive materials-picric acid etc. The main objective and summary for each work is described below:

- High-performance n-channel OFETs based on NDI-CY2 with low operating voltage can be successfully fabricated using four different combination of dual high-k inorganic/low-k or high-k organic polymer bilayer gate dielectric using cost-effective fabrication techniques. The dual dielectric layer Al_2O_3/PVA reveals the best performance and has been compared to other dielectric combinations. The use of expensive Si-substrates, SiO_2 dielectrics and Au electrodes was avoided in this study. Easy processed, cost-effective device components were utilized that exhibits a highest electron mobility value of 0.08 cm^2/Vs. Significantly improved device parameters such as a low operating and threshold voltage of 5 V and 0.5 V were obtained respectively with the Al_2O_3/PVA dielectric combination, which has not been realized previously with this promising molecule. Finally, by analyzing the morphologies and microstructures of NDI-CY2, the variations in the electrical characteristics of the OFET device obtained for different dual dielectric combinations have been demonstrated which mainly due to the diverse properties of dielectric/NDI-CY2 interfacial layer that govern the accumulation of carriers and charge transport.
- Importance of trilayer dielectrics i.e. high-k inorganic metal-oxide (Al_2O_3)/high-k organic polymer (PVA)/low-k organic polymer (PMMA) to fine-tune the

performance of n-channel OFET based on methyl cyclohexane functionalized NDI i.e. NMeCy2 was established in chapter 3. By employing the trilayer dielectric arrangement, we can effectively reduce the operating voltage as well as V_{TH} without affecting μ_e and I_{ON}/I_{OFF} by promoting ordered growth of NMeCy2 with interconnected charge transport paths. The n-channel OFET device exhibited a saturation regime μ_e value of 0.6 cm^2/Vs. We could successfully lower the V_{TH} value up to 5.23 V and achieved high I_{ON}/I_{OFF} of 10^6, which is one of the best performing devices among n-channel OFETs. The improved performances of the OFET devices are attributed to well-directed close intermolecular π-stacking in thin films over a large scale, the superior film forming ability of NMeCy2 at the trilayer dielectric/semiconductor interface that reduces interfacial defects. The phenomena occurring at the interface between the gate dielectric and the active layer channel have been marked as being closely associated with the overall device operation and performance. Our concept of trilayer dielectric with inorganic high-k metal-oxide and organic polymer high-k/low-k dielectric stacked system demonstrated a significant step towards fabricating cost-effective, easy processed, high performance organic electronic devices.

- Detection of NH_3 vapors has become progressively significant for environmental as well as health monitoring, personal safety, industrial manufacturing, etc. But an advanced method for trace level detection of NH_3 vapors (<2 ppb for environmental monitoring and <50 ppb for breath analysis) is still missing, and the development of such sensing platform is highly desirable for monitoring trace levels of NH_3 vapors. A new and efficient platform for the vapor phase detection of NH_3 using a two terminal sensor device based on PDI-HIS nanostructures has been developed in chapter 4. The sensing parameters viz. sensitivity, selectivity, recyclability, response/recovery time and stability were studied that revealed outstanding performance of the device with a very low detection limit of 0.56 ppm. We have also demonstrated that the molecular self-assemblies of PDI-HIS nanostructures, redox potential and ionic groups at the imide position are key aspects for the significant response of the device towards NH_3 vapors. Thus, the efficiency of as-fabricated sensor device to detect NH_3 vapors at room temperature under ambient condition with high sensitivity, selectivity and low fabrication cost makes the protocol economical and feasible for potential applications in chemical, biomedical areas under competitive environmental conditions.

- The development of reliable methods for the rapid and selective detection of ultratrace amount of nitroexplosive are of vital concern for national security as well as environmental pollution. Owing to its high solubility in water, it can simply contaminate soil as well as groundwater. The detection of traces of nitroexplosive PA vapors is an area of great research interest as the vapor phase detection of PA is still remains a challenging task due to its low vapor pressure in comparison to other nitro derivatives. Development of highly specific and sensitive probe for detection of PA remains a challenging operation for the investigators due to the absence of any suitable receptor for PA and interference from other electron deficient nitroexplosives. The final chapter highlighted the application of cationic NDMI probe for detection of potent nitroexplosive and highly water soluble pollutant PA both in aqueous medium as well as vapor phase. The vapor mode detection was carried out via fabricating a two terminal sensor device using single crystalline NDMI. Finally a simple, portable and cost-effective electronic prototype was developed for visual on-site detection of PA vapors in order to prevent terrorist threats rapidly under very realistic conditions.

1.10 References

(1) Dimmitrakopoulos, C. D.; Malenfant, P. R. L. *Adv. Mater.*, **2002**, *14*, 99.

(2) Muccini, M. *Nat. Mater.*, **2006**, *5*, 605.

(3) Chiang, C. K.; Fincher, C. R.; Park, Y. W.; Heeger, A. J.; Shirakawa, H.; Louis, E. J.; Gau, S. C.; MacDarmid, A. G. *Phys. Rev. Lett.*, **1977**, *39*, 1098.

(4) Yamada, H.; Okujimaa, T.; Ono, N. *Chem. Commun.*, **2008**, 2957.

(5) Takimiya, K.; Kunugi, Y.; Otsubo, T. *Chem. Lett.*, **2007**, *36*, 578.

(6) Anthony, J. E. *Chem. Rev.*, **2006**, *106*, 5028.

(7) Anthony, J. E. *Angew. Chem. Int. Ed.*, **2008**, *47*, 452.

(8) Blouin, N.; Leclerc, M. *Acc. Chem. Res.*, **2008**, *41*, 1110.

(9) Mas-Torrent, M.; Rovira, C. *Chem. Soc. Rev.*, **2008**, *37*, 827.

(10) Pron, A.; Gawrys, P.; Zagorska, M.; Djurado, D.; Demadrille, R. *Chem. Soc. Rev.*, **2010**, *39*, 2577.

(11) Wu, W.; Lui, Y.; Zhu, D. *Chem. Soc. Rev.*, **2010**, *39*, 1489.

(12) Wang, C.; Dong, H.; Hu, W.; Liu, Y.; Zhu, D. *Chem. Rev.*, **2012**, *112*, 2208.

(13) Klauk, H. *Chem. Soc. Rev.*, **2010**, *39*, 2643.

(14) Allard, S.; Forster, M.; Souharce, B.; Thiem, H.; Scherf, U. *Angew. Chem. Int. Ed.*, **2008**, *47*, 4070.

(15) Gross, M.; Muller, D. C.; Nothofer, H.-G.; Scherf, U.; Neher, D.; Brauchle, C.; Meerholz, K. *Nature* **2000**, *405*, 661.

(16) Reineke, S.; Lindner, F.; Schwartz, G.; Seidler, N.; Walzer, K.; Lüssem, B.; Leo, K. *Nature* **2009**, *459*, 234.

(17) Hains, A. W.; Liang, Z.; Woodhouse, M. A.; Gregg, B. A. *Chem. Rev.*, **2010**, *110*, 6689.

(18) Baeg, K.-J.; Binda, M.; Natali, D.; Caironi, M.; Noh, Y.-Y. *Adv. Mater.*, **2013**, *25*, 4267.

(19) Fukuda, K.; Hikichi, K.; Sekine, T.; Takeda, Y.; Minamiki, T.; Kumaki, D.; Tokito, S. *Sci Rep.*, **2013**, *3*, 2048.

(20) Someya, T.; Kato, Y.; Sekitani, T.; Iba, S.; Noguchi, Y.; Murase, Y.; Kawaguchi, H.; Sakurai, T. *Proc. Natl. Acad. Sci. USA* **2005**, *102*, 12321.

(21) Kato, Y.; Sekitani, T.; Noguchi, Y.; Yokota, T.; Takamiya, M.; Sakurai, T.; Someya, T. *IEEE Trans. Electron Devices* **2010**, *57*, 995.

(22) Medina-Saanchez, M.; Martinez-Domingo, C.; Ramon, E.; Merkoçi, A. *Adv. Funct. Mater.*, **2014**, *24*, 6291.

(23) Zaumseil, J.; Sirringhaus, H. *Chem. Rev.*, **2007**, *107*, 1296.

(24) Christopher, R. N.; Frisblie, C. D.; Demetrio, A.; da Filho, S.; Bredas, J-L.; Ewbank, P. C.; Mann, K. R. *Chem. Mater.*, **2004**, *16*, 4436.

(25) Mishra, A.; Bauerle, P. *Angew. Chem. Int. Ed.*, **2012**, *51*, 2020.

(26) Dong, H.; Wang, C.; Hu, W. *Chem. Commun.*, **2010**, *46*, 5211.

(27) Mei, J.; Diao, Y.; Appleton, A. L.; Fang, L.; Bao, Z. *J. Am. Chem. Soc.*, **2013**, *135*, 6724.

(28) Tsumura, A.; Koezuka, H.; Ando, T. *Appl. Phys. Lett.*, **1986**, *49*, 1210.

(29) Zhan, X.; Facchetti, A.; Barlow, S.; Marks, T. J.; Mark A. Ratner, M. A.; Wasielewski, M. R.; Seth R. Marder, S. R. *Adv. Mater.*, **2011**, *23*, 268.

(30) Jurchescu, O. D.; Popinciuc, M.; Wees, B. J. V.; Palstra, T. T. M. *Adv. Mater.*, **2007**, *19*, 688.

(31) Kaji, T.; Takenobu, T.; Morpurgo, A. F.; Iwasa, Y. *Adv. Mater.*, **2009**, *21*, 3689.

(32) Minemawari, H.; Yamada, T.; Matsui, H.; Tsutsumi, J.; Haas, S.; Chiba, R.; Kumai, R.; Hasegawa, T. *Nature* **2011**, *475*, 364.

(33) Li, L.; Tang, Q.; Li, H.; Yang, X.; Hu, W.; Song, Y.; Shuai, Z.; Xu, W.; Liu, Y.; Zhu, D. *Adv. Mater.*, **2007**, *19*, 2613.

(34) Lv, A.; Puniredd, S. R.; Zhang, J.; Li, Z.; Zhu, H.; Jiang, W.; Dong, H.; He, Y.; Jiang, L.; Li, Y.; Pisula, W.; Meng, Q.; Hu, W.; Wang, Z. *Adv. Mater.*, **2012** , *24*, 2626.

(35) Li, H.; Tee, B. C-K.; Cha, J. J.; Cui, Y.; Chung, J. W.; Lee, S. Y.; Bao, Z. *J. Am. Chem. Soc.*, **2012**, *134*, 2760.

(36) Zhao, X.; Xiong, Y.; Ma, J.; Yuan, Z. *J. Phys. Chem. A* **2016**, *120*, 7554.

(37) Chen, L.; Li, C.; Müllen, K. *J. Mater. Chem. C* **2014**, *2*, 1938.

(38) Weil, T.; Vosch, T.; Hofkens, J.; Peneva, K.; Mullen, K. *Angew. Chem. Int. Ed.*, **2010**, *49*, 9068.

(39) Liu, C.; Zhihong Liu, Z.; Lemke, H. T.; Tsao, H. N.; Naber, R. C. G.; Li, Y.; Banger, K.; Mullen, K.; Nielsen, M. M.; Sirringhaus, H. *Chem. Mater.*, **2010**, *22*, 2120.

(40) Tsao, H. N.; Pisula, W.; Liu, Z.; Osikowicz, W.; Salaneck, W. R.; Mullen, K. *Adv. Mater.*, **2008**, *20*, 2715.

(41) Jurchescu, O. D.; Popinciuc, M.; van Wees, B. J.; Palstra, T. T. M. *Adv. Mater.*, **2007**, *19*, 688.

(42) Ebata, H.; Izawa, T.; Miyazaki, E.; Takimiya, K.; Ikeda, M.; Kuwabara, H.; Yui, T. *J. Am. Chem. Soc.*, **2007**, *129*, 15732.

(43) Di, C. A.; Liu, Y. Q.; Yu, G.; Zhu, D. B. *Acc. Chem. Res.*, **2009**, *42*, 1573.

(44) Guo, Y.; Yu, G.; Liu, Y. *Adv. Mater.*, **2010**, *22*, 4427.

(45) Sun, Y.; Y.; Zhu, D. *J. Mater. Chem.*, **2005**, *15*, 53.

(46) Tsao, H. N.; Mullen, K. *Chem. Soc. Rev.*, **2010**, *39*, 1489.

(47) Sun, Y.; Liu, Y.; Zhu, D. *J. Mater. Chem.*, **2005**, *15*, 53.

(48) Shukla, D.; Nelson, S. F.; Freeman, D. C.; Rajeswaran, M.; Ahearn, W. G.; Meyer, D. M.; Carey, J. T. *Chem. Mater.*, **2008**, *20*, 7486.

(49) Kakinuma, T.; Kojima, H.; Ashizawa, M.; Matsumoto, H.; Mori, T. *J. Mater. Chem. C* **2013**, *1*, 5395.

(50) Dey, A.; Kalita, A.; Iyer, P. K. *ACS Appl. Mater. Interfaces* **2014**, *6*, 12295.

(51) Katz, H. E.; Lovinger, A. J.; Johnson, J.; Kloc, C.; Siegrist, T.; Li, W.; Lin, Y.-Y.; Dodabalapur, A. *Nature* **2000**, *404*, 478.

(52) He. T.; Stotle, M.; Wurthner, F. *Adv. Mater.*, **2013**, *25*, 6951.

(53) Hu, Y.; Gao, X.; Di, C.; Yang, X.; Zhang, F.; Liu, Y.; Li, H.; Zhu, D. *Chem. Mater.*, **2011**, *23*, 1204.

(54) Deng, P.; Yan, Y.; Wang, S. D.; Zhang, Q. *Chem. Commun.*, **2012**, *48*, 2591.

(55) Horowitz, G.; Kouki, F.; Spearman, P.; Fichou, D.; Nogues, C.; Pan, X.; Garnier, F. *Adv. Mater.*, **1996**, *8*, 242.

(56) Liu, C.; Xiao, C.; Li, Y.; Hu, W.; Lia, Z.; Wang, Z. *Chem. Commun.*, **2014**, *50*, 12462.

(57) Reghu, R. R.; Bisoyi, H. K.; Grazulevicius, J. V.; Anjukandi, P.; Gaidelis, V.; Jankauskas, V. *J. Mater. Chem.*, **2011**, *21*, 7811.

(58) Molinari, A. S.; Alves, H.; Chen, Z.; Facchetti, A.; Morpurgo, A. F. *J. Am. Chem. Soc.*, **2009**, *131*, 2462.

(59) Lv, A.; Puniredd, S. R.; Zhang, J.; Li, Z.; Zhu, H.; Jiang, W.; Dong, H.; He, Y.; Jiang, L.; Li, Y.; Pisula, W.; Meng, Q.; Hu, W.; Wang, Z. *Adv. Mater.*, **2012**, *24*, 2626.

(60) Meng, Q.; Zhang, F.; Zang, Y.; Huang, D.; Zou, Y.; Liu, J.; Zhao, G.; Wang, Z.; Ji, D.; Di, C.; Hu, W.; Zhu, D. *J. Mater. Chem. C* **2014**, *2*, 1264.

(61) Sun, X.; Wang, Y.; Lei, Y. *Chem. Soc. Rev.*, **2015**, *44*, 8019.

(62) Salinas, Y.; Martinez-Manez, R.; Marcos, M. D.; Sancenon, F.; Costero, A. M.; Parra, M.; Gil, S. *Chem. Soc. Rev.*, **2012**, *41*, 1261.

(63) Riskin, M.; Tel-Vered, R.; Willner, I. *Adv. Mater.*, **2010**, *22*, 1387.

(64) Shanmugaraju, S.; Mukherjee, P. S. *Chem. Commun.*, **2015**, *51*, 16014.

(65) Akhavan, J. The Chemistry of Explosives, 2nd ed.; Royal Society of Chemistry: Cambridge, UK, 2004.

(66) Kalita, A.; Hussain, S.; Malik, A. H.; Barman, U.; Goswami, N.; Iyer, P. K. *ACS Appl. Mater. Interfaces* **2016**, *8*, 25326.

(67) Ibanez, F. J.; Zamborini, F. P. *ACS Nano* **2008**, *2*, 1543.

(68) Meng, Q.; Zhang, F.; Zang, Y.; Huang, D.; Zou, Y.; Liu, J.; Zhao, G.; Wang, Z.; Ji, D.; Di, C.; Hu, W.; Zhu, D. *J. Mater. Chem. C* **2014**, *2*, 1264.

(69) Trogler, W. C. Chemical Sensing with Semiconducting Metal Phthalocyanines. Mingos. D. M. P.; Day, P.; Dahl. J. P., Eds., Springer Berlin/Heidelberg, 2012.

(70) Li, L.; Gao, P.; Baumgarten, M.; Mullen, K.; Lu, N.; Fuchs, H.; Chi, L. *Adv. Mater.*, **2013**, *25*, 3419.

(71) Nayak, A. K.; Ghosh, R.; Santra, S.; Guha, P. K.; Pradhan, D. *Nanoscale* **2015**, *7*, 12460.

(72) Roberts, M. E.; Sokolov, A. N.; Bao, Z. *J. Mater. Chem.*, **2009**, *19*, 3351.

(73) Bailey, R. A.; Persaud, K. C. Sensing Volatile Chemicals Using Conducting Polymer Arrays. In Polymer Sensors and Actuators; Osada, Y.; DeRossi, D. E., Eds., Springer-Verlag: Berlin, 2000.

(74) Sensing Technology: Current Status and Future Trends III. Mason, A.; Mukhopadhyay, S. C.; Jayasundera, K. P., Eds., 2014.

(75) Campbell, M. G.; Liu, S. F.; Swager, T. M.; Dincă, M. *J. Am. Chem. Soc.*, **2015,** *137*, 13780.

(76) Organic Semiconductors in Sensor Applications, edited by Bernards, D. A.; Owens, R. M.; Malliaras, G. G. (Springer Verlag, NY, 2008), Chap. 3, p. 61- 96.

(77) Che, Y.; Datar, A.; Yang, X.; Naddo, T.; Zhao, J.; Zang, L. *J. Am. Chem. Soc.*, **2007**, *129*, 6354.

(78) Che, Y.; Datar, A.; Balakrishnan, K.; Zang, L. *J. Am. Chem. Soc.*, **2007**, *129*, 7234.

(79) Huang, Y.; Fu, L.; Zou, W.; Zhang, F.; Wei, Z. *J. Phys. Chem. C* **2011**, *115*, 10399.

(80) Wu, N.; Wang, C.; Bunes, B. R.; Zhang, Y.; Slattum, P. M.;, Yang, X.; Zang, L. *ACS Appl. Mater. Interfaces* **2016**, *8*, 12360.

(81) Fan, J.; Chang, X.; He, M.; Shang, C.; Wang, G.; Yin, S.; Peng, H.; Fang, Y. *ACS Appl. Mater. Interfaces* **2016**, *8*, 18584.

(82) Ajayakumar, M. R.; Mukhopadhyay, P. *Org. Lett.*, **2010**, *12*, 2646.

(83) Ajayakumar, M. R.; Hundal, G.; Mukhopadhyay, P. *Chem. Commun.*, **2013**, *49*, 7684.

(84) Zang, Y.; Zhang, F.; Huang, D.; Di, C.; Meng, Q.; Gao, X.; Zhu, D. *Adv. Mater.*, **2014**, *26*, 2862.

Chapter 2

Effect of Inorganic/Organic Dual Dielectric Layer on the Morphology and Performance of n-channel OFETs

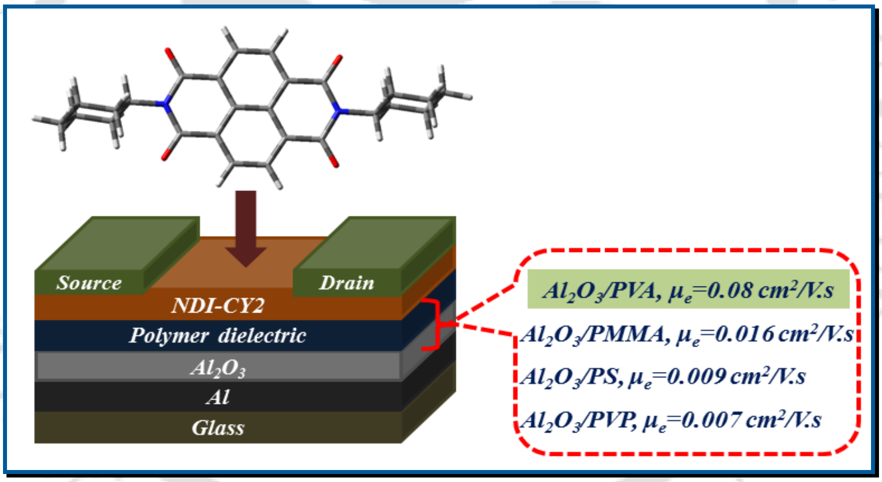

Phys. Chem. Chem. Phys., **2016**, *18*, 12163-12168.

Abstract

The optimization of dual dielectric layers by incorporating organic polymers like poly(vinyl alcohol) (PVA), poly(methyl methacrylate) (PMMA), polystyrene (PS) and poly(4-vinylphenol) (PVP) in combination with inorganic metal-oxide (Al_2O_3) resulted in immensely improved OFET device characteristics with N,N′-bis(cyclohexyl)naphthalene diimide (NDI-CY2) as active material. The influence of the polymeric dielectric layer on the growth morphology of NDI-CY2 and the structural characterization were investigated using atomic force microscopy (AFM) and thin film XRD analysis. The bottom-gate top-contact OFET devices fabricated via cost-effective techniques using glass substrates with Al contact electrodes demonstrated excellent n-channel behavior at substrate temperature 100 °C. Among all the four dual dielectric combinations, Al_2O_3/PVA exhibited highest electron mobility (μ_e) value of 0.08 cm^2/Vs having current on/off ratio (I_{ON}/I_{OFF}) of 10^4. There is a significant improvement in device parameters viz. V_{TH} and operating voltage as low as 0.5 V and 5 V respectively under vacuum condition.

2.1 Introduction

Conjugated organic materials are of great importance because of their potential use as organic semiconductors for various optoelectronic devices, including organic field-effect transistors (OFETs).[1-4] Currently, there is a growing interest in the development of newer active organic materials in order to fabricate complementary circuits.[5] Device characteristics with superior transistor performance are recognized primarily by a few parameters viz. the high carrier mobility, large current on/off ratio and low threshold voltage. To achieve these performances, the development of new organic semiconductors as well as the improvement in device structures are most vital.[6] Small molecule organic semiconductors with optimized molecular ordering facilitate improved charge transport resulting in higher mobilities compared to the polymer based OFET devices. Moreover, the device configuration also influences the measured electronic properties. For instance, the choice of metal electrodes affects the contact resistance. Therefore, it is important to choose the electrode metal according to the nature of the organic semiconductor to have efficient charge injection. The dielectric material also plays a vital role in device operation since it influences the electric field, current leakage through the gate insulator and the quality of the interface between the organic semiconductor and the dielectric. Like inorganic microelectronics, the most widely used dielectric in OFETs has been SiO_2 grown on doped Si gates. However, a lot of research focus has now shifted towards investigation of the influence of different types of inorganic as well as organic dielectrics on the OFET performance. Parameters such as pressure and substrate temperature also control the morphology and quality of the resulting films.[7] Although, a large number of π-conjugated small molecules have been designed and prepared for organic electronics applications. However, the research on n-channel organic materials is slow compared with that on p-channel organic semiconductors.[8] Hence, considerable attention is being devoted for developing and improving the performance of n-channel materials.[9] n-channel small molecule organic semiconductors like naphthalene diimides (NDIs),[10] perylene diimides (PDIs),[11,12] isoindigo[13] and fullerenes[14,15] have been in focus recently. Among these materials, enormous device potential have been shown by NDI based derivatives upon varying the molecular configuration as well as the device architecture.[16] In recent years, many groups reported a significant number of NDI based transistors demonstrating excellent and stable n-channel operation with a mobility value of 3.5 cm^2/Vs

for solution processed thin film transistors[17] and 8.6 cm^2/Vs for single-crystal transistors, respectively.[18] The applicability of these materials in optoelectronic devices such as organic thin-film transistors is primarily determined by their ability to form well-defined molecular crystals. Specifically, whether these compounds allow for the preparation of well-ordered crystalline thin films is one of the key design considerations. The morphology of the organic semiconductor over the dielectric layer too has a crucial impact on the charge transport properties that determines the overall device performance.[19] Moreover, due to the lack of clear ‘‘structure-property’’ relationships, a major challenge arises for researchers to design and develop stable, high performing n-channel organic semiconductors. Furthermore, functionalization at the imide position of NDI by end groups such as cyclohexyl provides a simple and effective way to control the crystalline packing motif and overall thin film morphology that leads to superior field effect mobility.[20,21] In this study, the anodized Al_2O_3 and solution-processed polymer dielectrics, viz. PVA, PMMA, PS, and PVP (**Figure 2.1**), were selected as the second layer in a dual gate dielectric to achieve stable and low operating voltage OFETs with lower thresholds. Al_2O_3 exhibits excellent insulating properties with dielectric constant ~8-10 that can be deposited by low-cost deposition process through the conversion of Al by anodization.[22–25] The use of organic polymer dielectrics has generally resulted in higher mobilities and better device reliability compared to the thermally grown commercial SiO_2.[26] Moreover, the low surface energy of the dual polymer-Al_2O_3 gate dielectric minimizes the interaction between the organic semiconductor (OSC) layer and the gate dielectric layer that induces greater interactions among semiconductor molecules through p-orbital overlapping.[27] In addition, the smoother topography of the upper hydrophobic polymer provides a homogeneous uniform platform for semiconductor growth

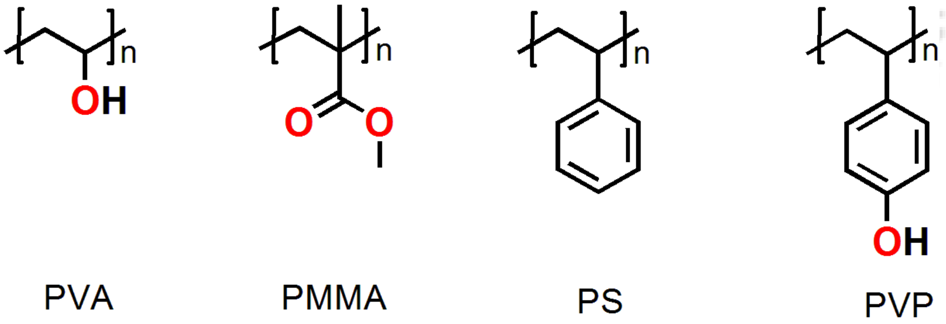

Figure 2.1 Structure of polymer dielectric materials.

and results in less distortion of the crystalline structure compared with highly rough inorganic gate dielectrics. As compared to Si-based OFETs, the fabricated OFETs using dual gate dielectrics allows for lowering of operating voltage as well as threshold voltage. NDI-CY2 was chosen as the active layer due to its outstanding field-effect characteristics as reported earlier.[17] The NDI-CY2 device showed typical n-channel OFET performance with relatively high electron mobility and on/off current ratio under vacuum. The bottom-gate top-contact OFET device based on NDI-CY2 exhibited the highest electron mobility of ~0.08 cm^2/Vs with Al_2O_3/PVA dual dielectric and a current on/off ratio of 10^4 respectively among other dielectric combinations under high vacuum conditions.

2.2 Experimental

2.2.1 Materials and measurements

1,4,5,8-Naphthalenetetracarboxylic dianhydride, cyclohexylamine, quinoline, zinc acetate, PMMA (average MW ~120000), PS (average MW ~350000), and PVP (average MW ~25000) were purchased from Sigma Aldrich and PVA (MW ~115000) from Loba Chemicals. ^1H NMR and ^{13}C NMR spectra were recorded on a Bruker Ascend 600 spectrometer. Using DFT method theoretical calculations were performed on a Gaussian 03 package with B3LYP hybrid functional and 6-31G basis set. Thin film XRD measurements were carried out on a high power (18 kW) X-ray diffractometer (Rigaku TTRAX III) with CuKα radiation. The AFM image was recorded on an Agilent 5500 AFM/SPM microscope in tapping mode to avoid any film damage due to tip-surface interactions. The thicknesses of all the thin films were measured using a Dektak 150 stylus profiler. All the electrical characterizations of OFET devices were performed using a Keithley 4200-SCS parameter analyzer under vacuum conditions.

2.2.2 Device fabrication and measurements

Bottom-gate, top-contact OFETs were fabricated using simple glass slides as substrates. The glass substrates were kept in piranha solution (3:1 H_2SO_4:H_2O_2) for some time and finally washed with deionized water several times. The cleaned glass substrates were subsequently dried under vacuum at 100 °C. A patterned 150 nm thick aluminum gate electrode was deposited using a thermal evaporator onto the glass substrates. The top surface was anodized to get 12 nm of Al_2O_3. Anodization was carried out with a constant current of j = 0.6 mA

cm^{-2} driven through the electrolyte. A 0.001 M citric acid monohydrate ($C_6H_8O_7 \bullet H_2O$) was used to prepare electrolyte solution using ultrapure Milli-Q water. The aluminum-coated glass substrates were immersed into the electrolyte, which work as a working electrode (anode), and a platinum mesh served as the counter electrode (cathode). A Keithley 2400 source meter was used for supplying constant current. Constant current across the growing insulating Al_2O_3 layer was maintained by ramping up the voltage to a limiting anodization voltage (V_A), which was then maintained for several minutes until the current had completely decayed to below 5 μA. The thickness (d) of the resulting films can be controlled very precisely via the anodization voltage V_A, with $d=cV_A$, where c is the "anodization ratio" value for aluminum (1.3 nm/V). The samples were subsequently rinsed in high-purity Milli-Q water heated at 60 °C to remove the citric acid molecules and carefully dried in a hot plate at a temperature of 100 °C. After anodization, 30 mg each of PVA, PS, PVP and PMMA were dissolved in 1 mL of solvent (deionized water, THF, toluene and anisole) respectively to prepare a 3% polymer dielectric solution. A 100 nm thick layer of each dielectric was obtained by spin-coating each solution at 3000 rpm for 60s to reduce the surface roughness, and dried for 1h at 120 °C under an argon atmosphere. Following this and after optimizing the deposition temperature of NDI-CY2, a 60 nm thin film of NDI-CY2 active material was deposited at 100 °C substrate temperature using a thermal deposition method under a base pressure of 10^{-6} mbar. The Al source and drain contacts (80 nm) were deposited on the organic layer through a shadow mask with a channel length (L) and width (W) of 40 mm and 800 mm, respectively. All the electrical properties of the fabricated OFETs were measured under vacuum using a Keithley 4200-SCS semiconductor parameter analyzer. The field-effect mobility (μ) in the saturation regime was extracted using the equation $I_{DS}=(\mu WC_i/2L)(V_G-V_{TH})^2$ under the conditions of $V_{DS}>(V_G- V_{TH})$, where W is the channel width, L is the channel length, C_i is the capacitance per unit area of the gate dielectric layer, and V_G, V_{TH} and V_{DS} are the gate, threshold and source-drain voltages, respectively.

2.2.3 Synthesis of N, N′-bis(cyclohexyl)naphthalene diimide (NDI-CY2)

A mixture of 1, 4, 5, 8-Naphthalenetertacarboxylic dianhydride (0.5 g, 1.8 mmol), cyclohexylamine (1.10g, 11.16 mmol) and zinc acetate (25 mg) in 15 mL quinolone was heated at 150 °C for 6h. The reaction mixture was cooled to room temperature and diluted with several volumes of methanol. The resulting slurry was filtered; the collected solid was washed with methanol and dried in air. The crude product was further purified by column chromatography using hexane-chloroform as eluent. Yield: 85%. ^{1}H NMR (600 MHz, $CDCl_3$, δ ppm): 8.70 (s), 5.01 (m), 2.51 (m), 1.57 (s), 0.87 (t). ^{13}C NMR (150 MHz, $CDCl_3$, δ ppm): 163.54, 131.03, 127.11, 54.64, 29.90, 26.68, 25.54.

2.3 Results and discussion

2.3.1 Synthesis and characterization of NDI-CY2

NDI-CY2 was synthesized following the reported procedure by a simple condensation method as shown in **Scheme 2.1**.[28] The synthesized NDI-CY2 were characterized by ^{1}H and ^{13}C NMR (**Figure A2.1 and A2.2**).

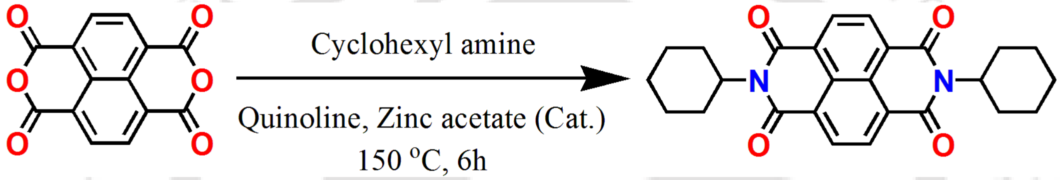

Scheme 2.1. Synthetic scheme of NDI-CY2.

2.3.2 Morphology and structural characterization

The as-fabricated thin film morphology of various dual dielectric layers and the deposited organic semiconductor NDI-CY2 on the dielectric layers, after optimizing the substrate temperature at T_{sub}=100 °C were investigated by AFM analysis (**Figure 2.2 and 2.3**). In general, dielectric surface roughness or irregularities are vital factors that affect the device performance as well as its parameters. Interfacial roughness hinders the charge conduction by disturbing the morphology or acting as physical traps in the organic semiconductor layer. The representative surface morphology of anodized Al_2O_3 (**Figure A2.3**) exhibits a very rough surface (R_q=27 nm) compared to various dual dielectric layers, viz. Al_2O_3/PVA (R_q=0.32 nm), Al_2O_3/PMMA (R_q=0.30 nm), Al_2O_3/PS (R_q=0.49 nm) and Al_2O_3/PVP (R_q=2.33 nm) (**Figure 2.2**), which indicates that the single anodized Al_2O_3 layer is not suitable for an ordered growth of the semiconductor. After the deposition of each polymer dielectric by spin coating, the roughness decreases down to lower values. Such a highly smooth surface is an essential platform for the growth of quality films, which results in efficient charge transport between the dielectric layer and the semiconductor channel. From the AFM images of dielectric films, we observed a fairly good correlation between the morphology and the device performance. The Al_2O_3/PVA and Al_2O_3/PMMA dual dielectrics provide a superior device performance compared to Al_2O_3/PS and Al_2O_3/PVP, which is due to the better surface morphology provided for OSC growth. The surface topography image of the NDI-CY2 film (**Figure 2.3**) deposited on different dual dielectric layers at 100 °C substrate temperature displayed similar surface morphologies with closely packed grain regions. The AFM topographic image of NDI-CY2 on Al_2O_3/PVA exhibited flat homogeneous compact regions having a few elongated stripe like structures with an RMS surface roughness of 11 nm (**Figure 2.3a**). The topography of a densely packed NDI-CY2 without any stripe like structure on the dual gate dielectric Al_2O_3/PMMA (**Figure 2.3b**) shows a RMS roughness of ~9.5 nm. **Figure 2.3c and 2.3d** (Al_2O_3/PS and Al_2O_3/PVP) reveals that the surface growth is very similar in all the cases with RMS surface roughness values of 5.5 and 7.6 nm,

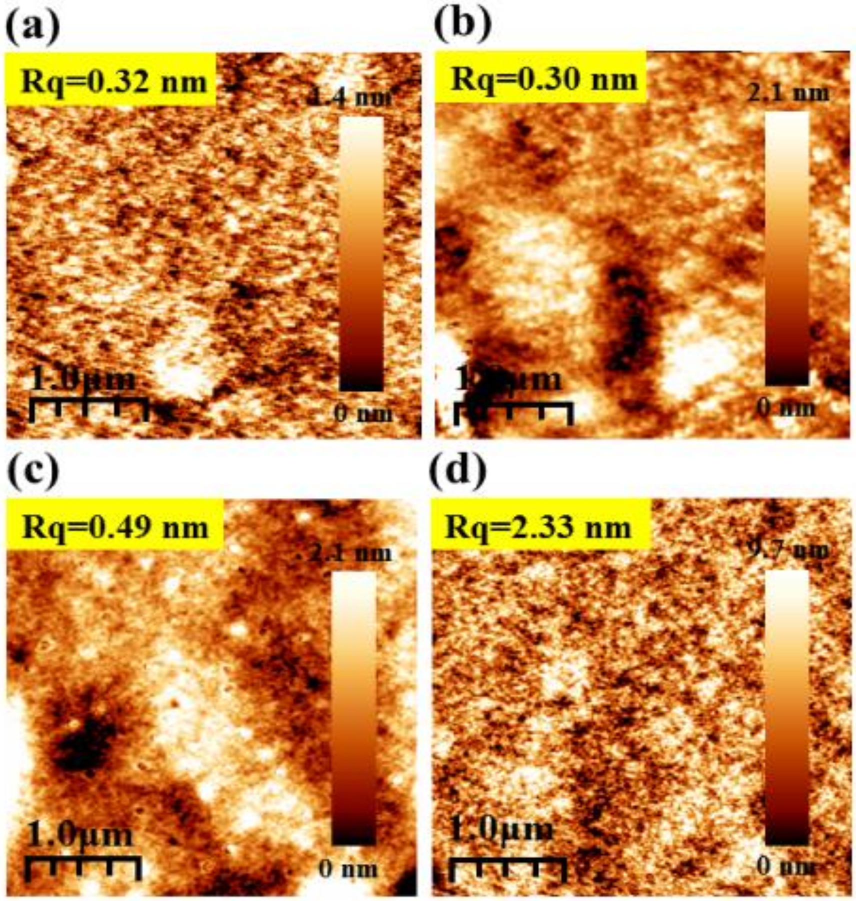

Figure 2.2 5×5 μm^2 AFM images of various dual dielectric layers (a) Al_2O_3/PVA, (b) Al_2O_3/PMMA, (c) Al_2O_3/PS and (d) Al_2O_3/PVP.

respectively. Though the RMS roughness is higher in all the four cases, only the first few layers of NDI-CY2 that are in direct contact with the dielectric contribute to proper charge conduction through the interface. The thin film microstructures of NDI-CY2 on each dual dielectric at T_{sub} = 100 °C were studied using thin film XRD technique (**Figure 2.4**).

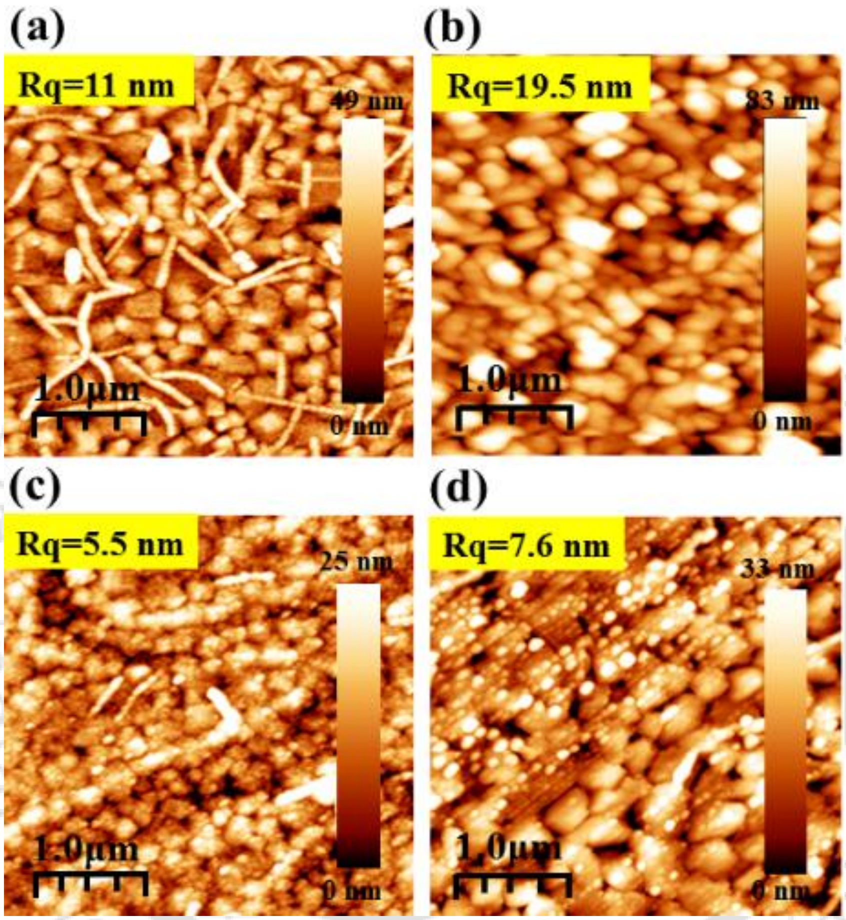

Figure 2.3 5×5 μm^2 AFM images of NDI-CY2 film deposited at T_{sub}=100 °C on (a) Al_2O_3/PVA, (b) Al_2O_3/PMMA, (c) Al_2O_3/PS and (d) Al_2O_3/PVP.

Besides the dependence of transport properties on surface morphology, thin film crystallinity is also a key factor for influencing the carrier mobility through the OSC. As shown in **Figure 2.4**, the substrate temperature has a significant influence on the morphology and crystallinity of the microstructures, which presumably affects the corresponding charge transport properties. A highly intense diffraction peaks were observed in all the four cases which indicated a higher degree of crystallinity of NDI-CY2 on dielectric layers. The reflection peak at 2θ=4.91 was observed for all the dielectric coated thin films, corresponding to a d-spacing of 17.8 Å, which is comparable to the molecular length obtained from DFT calculations (17.9 Å, **Figure A2.4**). Moreover, the peak intensities of the Bragg reflection of the NDI-CY2 thin film on PVA and PMMA were more noticeable than those on PS and PVP. This confirms that the crystalline qualities of the NDI-CY2 thin film on PVA and PMMA were superior to those on PS and PVP, thereby resulting in better charge carrier mobilities.

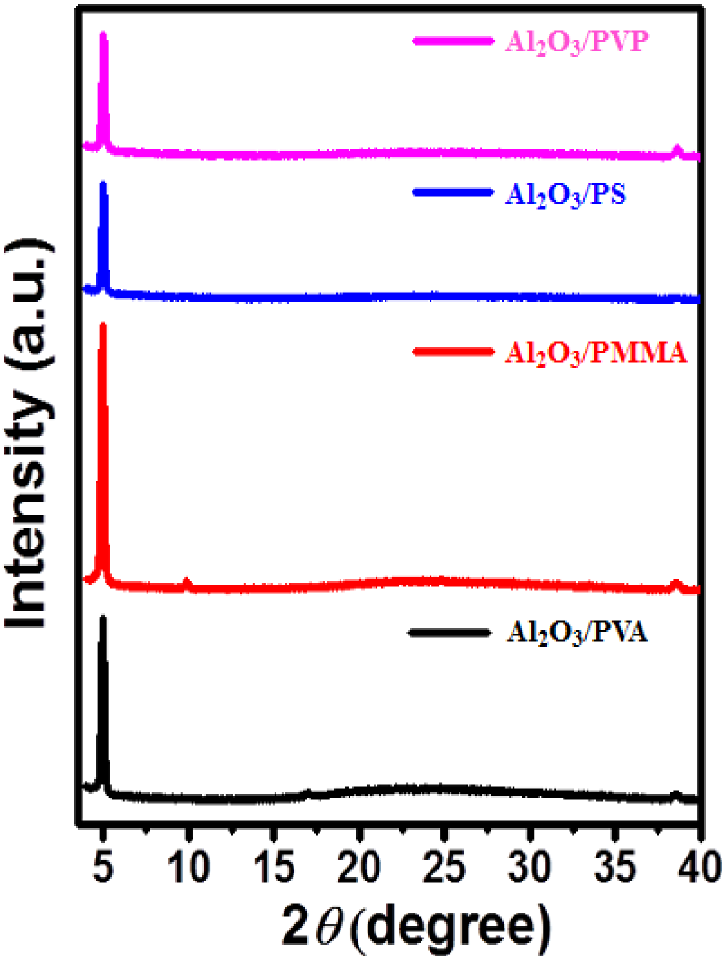

Figure 2.4 Thin film XRD of NDI-CY2 film deposited on various dielectric combination at T_{sub}=100 °C.

2.3.3 OFET fabrication and characterization

A bottom-gate, top-contact OFET device based on NDI-CY2 molecule was fabricated using various combinations of dual dielectric systems viz. Al_2O_3/PVA, Al_2O_3/PMMA, Al_2O_3/PS and Al_2O_3/PVA, where Al_2O_3 layer was deposited via well-known anodization method[29] and spin coating technique was used for coating polymer layers. **Figure 2.5 and 2.6** depicts the typical schematic of the device geometry with the NDI-CY2 molecule and the representative output and transfer characteristics of the OFET devices respectively using different dual dielectrics at 100 °C substrate temperature.

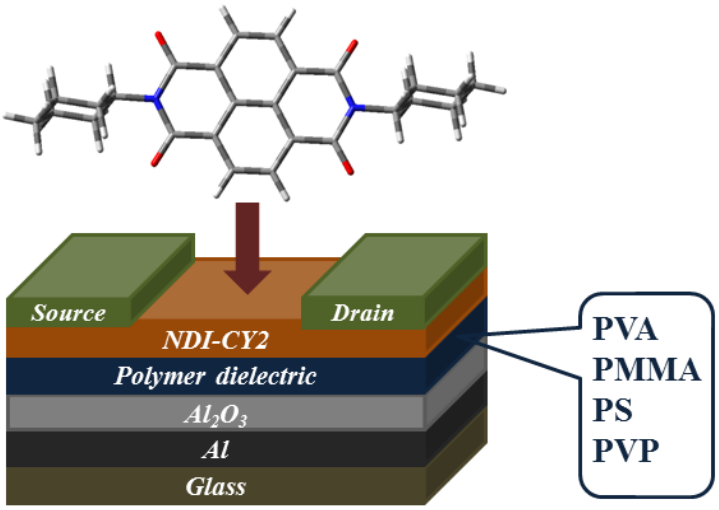

Figure 2.5 OFET device with bottom-gate top-contact geometry using NDI-CY2 as active layer with various combination of dual dielectric.

The transport properties of NDI-CY2 were optimized under various conditions, viz. by using single inorganic Al_2O_3 as well as single polymeric gate dielectric layer, varying substrate temperatures etc. Single Al_2O_3 layer based OFETs did not show any satisfactory device properties and exhibited very high leakage current due to high surface roughness (**Figure A2.3**), which confirms that it is inappropriate for growing smoother semiconducting interfacial layers. However, OFETs with a single polymer dielectric layer provide high threshold voltage as well as operating voltage though they offer smooth surfaces for ordered growth of semiconductor layer over it. Finally we optimized the OFET device with dual dielectric combinations (inorganic/organic) along with 100 °C substrate temperature as the most optimum conditions.

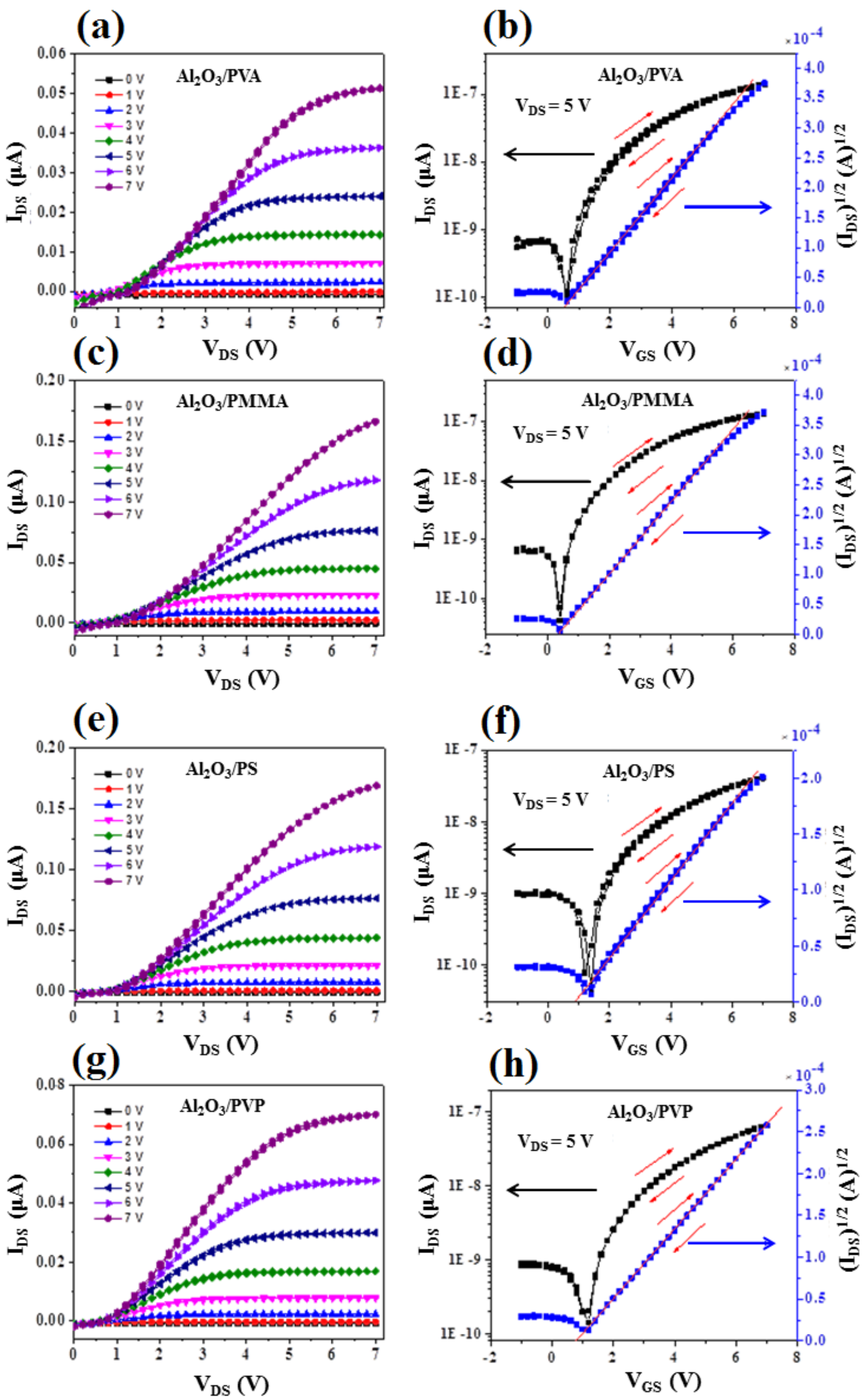

Figure 2.6 Output curves of NDI-CY2 OFETs for dielectric combinations (a) Al_2O_3/PVA, (c) Al_2O_3/PMMA, (e) Al_2O_3/PS, (g) Al_2O_3/PVP and transfer curves for (b) Al_2O_3/PVA, (d) Al_2O_3/PMMA, (f) Al_2O_3/PS, (h) Al_2O_3/PVP.

The summary of the device data fabricated for various dual dielectric combinations are given in **Table 1**.

Table 1. Summary of device data.

Dual-dielectrics	V_{TH} (V)	C_i (nF/cm^2)	W (µm)	L (µm)	μ_e (cm^2/Vs)	I_{ON}/I_{OFF}
Al_2O_3/PVA	0.50	3.25	800	40	0.080	10^4
Al_2O_3/PMMA	0.47	31.0	800	40	0.016	10^4
Al_2O_3/PS	0.86	10.68	800	40	0.009	10^3
Al_2O_3/PVP	0.76	14.2	800	40	0.007	10^3

Herein, we successfully reported the electrical characteristics and operational stability of low-operating voltage NDI-CY2 based OFETs fabricated on a low-cost glass slide as the substrate and dual dielectric layers. There are very specific requirements for gate dielectrics to be used in field-effect transistors. Apart from high capacitance, high dielectric breakdown strength, high levels of purity, high on to off ratios, low hysteresis, material processability and device stability are the most essential.[30,31] In order to fabricate OFET devices in the current study, anodized Al_2O_3 was utilized as one of the dielectric layers since it offers a higher capacitance than thermally grown SiO_2 and exhibits optimum mechanical and insulating properties.[32] Because of its low cost deposition process, Al_2O_3 is one of the highly favorable dielectric materials for OFET device fabrication. However, the thin film forming ability of this inorganic dielectric is inferior, which results in a huge current leakage problem during device operation. On the other hand, polymeric materials are promising alternatives to improve the film quality and build flexible OFETs.[33] To fulfill this requirement, various classical polymers including PVA, PMMA, PS and PVP have been extensively utilized as the gate insulator in OFETs.[34-37] Generally it is difficult to meet the requirements for a high-performance OFET from a single polymeric material. Therefore, several organic-inorganic hybrid combinations have been proposed to overcome this problem.[38,39] A polymer dielectric layer on an inorganic metal oxide layer can greatly decrease the RMS roughness in addition to providing a high quality interface for OSC growth by minimizing the surface energy of dual dielectrics and provides enhanced overall device performances. Moreover, there have been numerous reports on the OSC based electronic devices which prove that these semiconducting devices have several inherent advantages like energy-efficiency and eco-friendly nature that silicon-based electronics lack. Recently, an NDIOD2 based OTFT device fabricated on a glass slide along with a biodegradable and biocompatible PVA dielectric has shown an excellent electron mobility of ~1 cm^2/Vs.[40]

In 2008, Shukla *et al.* reported an NDI-CY2 based OFET device with a mobility value as high as 6 cm^2/Vs with a threshold voltage of 58 V under an argon atmosphere when fabricated on an OTS treated SiO_2 substrate with a gold source-drain contact and measured.[20] Recently, Kakinuma *et al.* reported an OFET device using the same molecule; however, the mobility value obtained was 0.52 cm^2/Vs with a threshold voltage of 44 V, in vacuum.[41] In both the above cases, the dielectric materials used were SiO_2, source and drain contacts were gold and the devices had very high threshold and operating voltages. In the present study, we have successfully reported the fabrication of a cost-effective OFET device on a glass substrate based on the NDI-CY2 molecule, along with improved device performance by drastically reducing the operating as well as the threshold voltages, which is expected to have diverse applications in memory devices, RFID tags, biomedical devices and sensors.

2.4 Conclusion

In summary, we have successfully demonstrated high-performance n-channel OFETs based on NDI-CY2 using four different dual dielectric combinations. The dual dielectric layer Al_2O_3/PVA reveals the best performance among all and has been compared to other dielectric combinations. Use of expensive Si-substrates, SiO_2 dielectrics and Au contact electrodes were avoided in this investigation. Cost-effective, simple and easy processed device components were utilized that displayed a highest mobility value of 0.08 cm^2/Vs with I_{ON}/I_{OFF} ratio of 10^4. Moreover, vastly enhanced device parameters like low operating voltage and lower threshold voltage of around 5 V and 0.5 V were obtained respectively with Al_2O_3/PVA dielectric combination, which has not been recognized earlier with this promising material. The morphology and structural characterization of NDI-CY2 correlates the electrical properties of the OFET devices with various dual dielectric combinations. The variations in charge transport properties are mainly affected by the diverse dielectric/NDI-CY2 interfacial layer that governs the transport and accumulation of charge carriers.

2.5 References

(1) Yoon, M. H.; DiBenedetto, S. A.; Facchetti, A.; Mark, T. J. *J. Am. Chem. Soc.*, **2006**, *127*, 1348.

(2) Takimiya, K.; Kunugi, Y.; Konda, Y.; Ebata, H.; Toyoshima, Y.; Otsubo, T. *J. Am. Chem. Soc.*, **2006**, *128,* 3044.

(3) Dimitrakopoulos, C. D.; Malenfant, R. L. *Adv. Mater.*, **2002**, *14*, 99.

(4) Mamada, M.; Kumaki, D.; Nishida, J.; Tokito, S.; Yamashita, Y. *ACS Appl. Mater. Interfaces* **2010**, *2*, 1303.

(5) Crone, B.; Dodabalapur, B.; Lin, A.; Filas, Y.-Y.; Bao, R. W.; LaDuca, Z.; Sarpeshkar, R.; Katz, H. E.; Li, W. *Nature* **2000**, *403*, 521.

(6) Yamashita, Y. *Sci. Technol. Adv. Mater.*, **2009**, *10*, 024313.

(7) Mas-Torrent, M.; Rovira, C. *Chem. Soc. Rev.*, **2008**, *37*, 827.

(8) Chen, W.; Zhang, J.; Long, G.; Liuc, Y.; Zhang, Q. *J. Mater. Chem. C* **2015**, *3*, 8219.

(9) Mori, T. *J. Phys.: Condens. Matter* **2008**, *20*, 184010.

(10) Wang, Z.; Zhao, J.; Dong, H.; Qiu, G.; Zhang, Q.; Hu, W. *Phys. Chem. Chem. Phys.*, **2015**, *17*, 26519.

(11) Jones, B. A.; Ahrens, M. J.; Yoon, M. H.; Facchetti, A.; Marks, T. J.; Wasielewski, M. R. *Angew. Chem., Int. Ed.*, **2004**, *43*, 6363.

(12) Lv, A.; Puniredd, S. R.; Zhang, J.; Li, Z.; Zhu, H.; Jiang, W.; Dong, H.; He, Y.; Jiang, L.; Li, Y.; Pisula, W.; Meng, Q.; Hu, W.; Wang, Z. *Adv. Mater.*, **2012**, *24*, 2626.

(13) Yue, W.; He, T.; Stolte, M.; Gsanger, M.; Würthner, F. *Chem. Commun.*, **2014**, *50*, 545.

(14) Haddon, R. C. *J. Am. Chem. Soc.*, **1996**, *118*, 3041.

(15) Kitamura, M.; Aomori, S.; Na, J. H.; Arakawa, Y. *Appl. Phys. Lett.*, **2008**, *93*, 033313.

(16) Rodel, R.; Letzkus, F.; Zaki, T.; Burghartz, J. N.; Kraft, U.; Zschieschang, U.; Kem, K.; Klauk, H. *Appl. Phys. Lett.*, **2013**, *102*, 233303.

(17) Zhang, F.; Hu, Y.; Schuettfort, T.; Di, C.; Gao, X.; McNeill, C. R.; Thomsen, L.; Mannsfeld, S. C. B.; Yuan, W.; Sirringhaus, H.; Zhu, D. *J. Am. Chem. Soc.*, **2013**, *135*, 2338.

(18) He, T.; Stolte, M.; Würthner, F. *Adv. Mater.*, **2013**, *25*, 6951.

(19) He, T.; Stolte, M.; Burschka, C.; Hansen, N. H.; Musiol, T.; Kälblein, D.; Pflaum, J.; Tao, X.; Brill, J.; Würthner, F. *Nat. Commun.,* **2015**, *6*, 5954.

(20) Shukla, D.; Nelson, S. F.; Freeman, D. C.; Rajeswaran, M.; Ahearn, W. G.; Meyer, D. M.; Carey, J. T. *Chem. Mater.*, **2008**, *20*, 7486.

(21) Adiga, P. S.; Shukla, D. *J. Phys. Chem. C* **2010**, *114*, 2751.

(22) Majewski, L. A.; Schroeder, R.; Grell, M. *J. Phys. D: Appl. Phys.*, **2004**, *37*, 21.

(23) Hickmott, T. W. *J. Appl. Phys.*, **2001**, *89*, 5502.

(24) Hebard, A. F.; Ajuria, S. A.; Eick, R. H. *Appl. Phys. Lett.*, **1987**, *51*, 1349.

(25) Lin, H. C.; Ye, P. D.; Wilk, G. D. *Appl. Phys. Lett.*, **2005**, *87*, 182904.

(26) Veres, J.; Ogier, S.; Lloyd, G. *Chem. Mater.*, **2004**, *16*, 4543.

(27) Shin, K.; Yang, C.; Yang, S. Y.; Jeon, H.; Parka, C. E. *Appl. Phys. Lett.*, **2006**, *88*, 072109.

(28) Kalita, A.; Subbarao, N. V. V.; Iyer, P. K. *J. Phys. Chem. C* **2015**, *119*, 12772.

(29) Subbarao, N. V. V.; Gedda, M.; Vasimalla, S.; Iyer, P. K.; Goswami, D. *Phys. Status Solidi A* **2014**, *211*, 2403.

(30) Zhao, J.; Uosaki, K. *Appl. Phys. Lett.*, **2003**, *83*, 2034.

(31) Balk, P. *Adv. Mater.*, **1995**, *7*, 703.

(32) Ha, W. H.; Choo, M. H.; Im, S. J. *Non-Cryst. Solids* **2002**, *303*, 78.

(33) Liu, C.; Zhu, Q.; Jin, W.; Gu, W.; Wang, J. *Synth. Met.*, **2011**, *161*, 1635.

(34) Peng, X.; Horowitz, G.; Fichou, D.; Garnier, F. *Appl. Phys. Lett.*, **1990**, *57*, 2013.

(35) Yoon, M. H.; Kim, C.; Facchetti, A.; Marks, T. J. *J. Am. Chem. Soc.*, **2006**, *128*, 12851.

(36) Hwang, D. K.; Kim, C. S.; Choi, J. M.; Lee, K.; Park, J. H.; Kim, E.; Baik, H. K.; Kim, J. H.; Im, S. *Adv. Funct. Mater.*, **2006**, *18*, 2299.

(37) Wang, Y.; Acton, O.; Ting, G.; Weidner, T.; Shamberge, P. J.; Ma, H.; Ohuchi, F. S.; Castner, D. G.; Jen, A. K.-Y. *Org. Electron.*, **2010**, *11*, 1066.

(38) Jung, C.; Maliakal, A.; Sidorenko, A.; Siegrist, T. *Appl. Phys. Lett.*, **2007**, *90*, 062111.

(39) Lu, Y.; Lee, W. H.; Lee, H. S.; Jang, Y.; Cho, K. *Appl. Phys. Lett.*, **2009**, *94*, 113303.

(40) Dey, A.; Kalita, A.; Iyer, P. K. *ACS Appl. Mater. Interfaces* **2014**, *6*, 12295.

(41) Kakinuma, T.; Kojima, H.; Ashizawa, M.; Matsumoto, H.; Mori, T. *J. Mater. Chem.*, **2013**, *1*, 5395.

2.6 Appendix

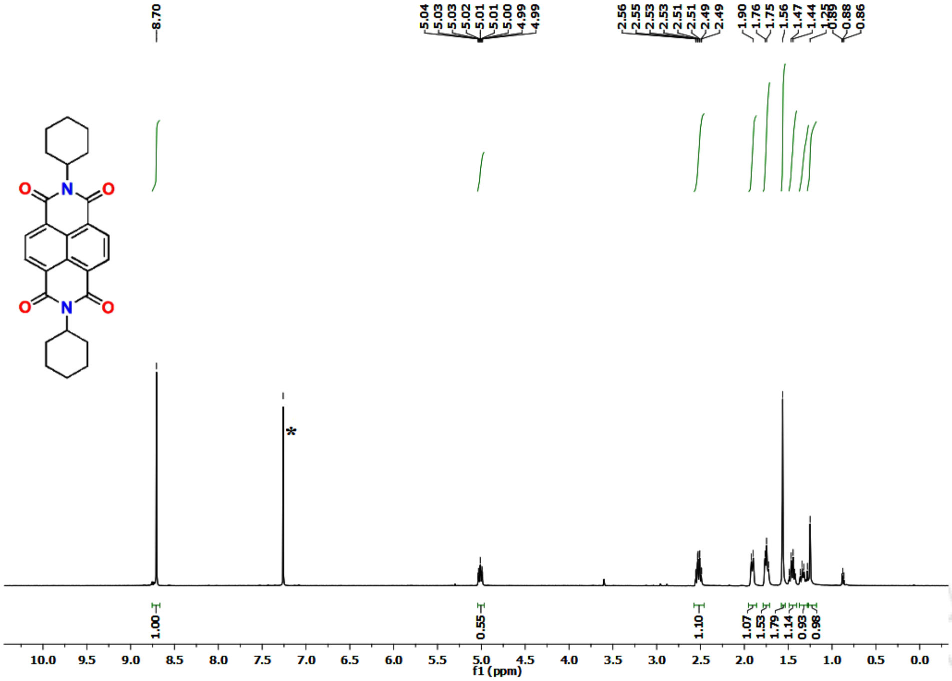

Figure A2.1 ^{1}H NMR (600 MHz, $CDCl_3$) spectra of NDI-CY2.

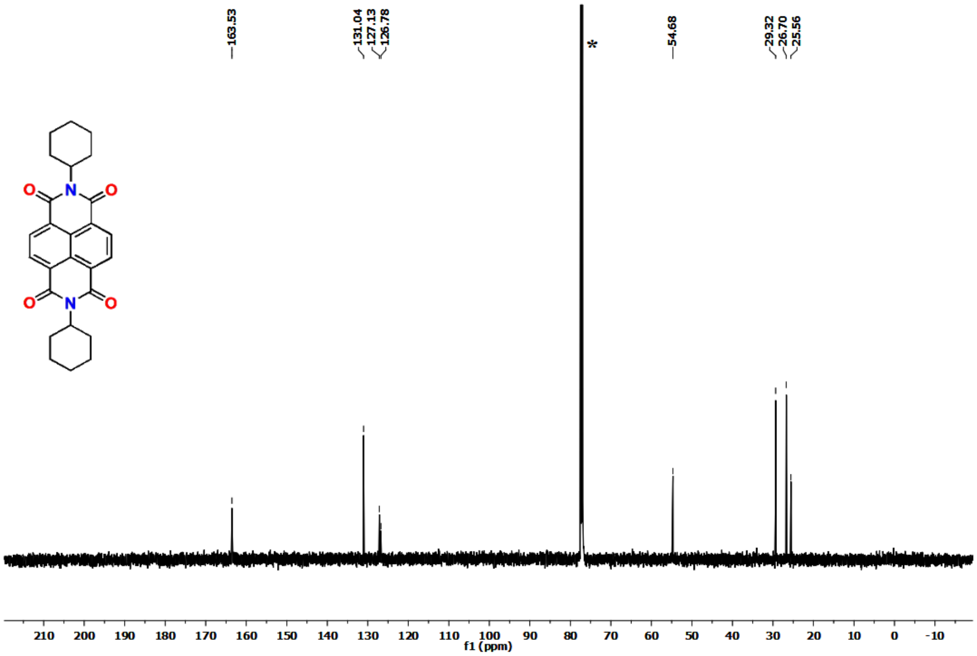

Figure A2.2 ^{13}C NMR (150 MHz, $CDCl_3$) spectra of NDI-CY2.

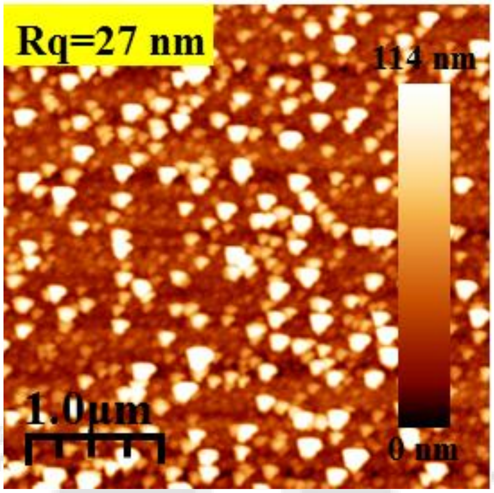

Figure A2.3 AFM image of anodized Al_2O_3 layer.

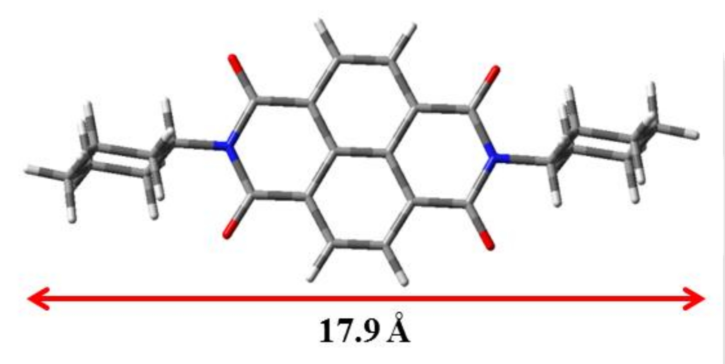

Figure A2.4 Molecular length of NDI-CY2 (17.9 Å) estimated from DFT calculation.

Chapter 3

Large-Scale Molecular Packing and Morphology Dependent High Performance Organic Field-Effect Transistor by Symmetrical Naphthalene Diimide Appended with Methyl Cyclohexane

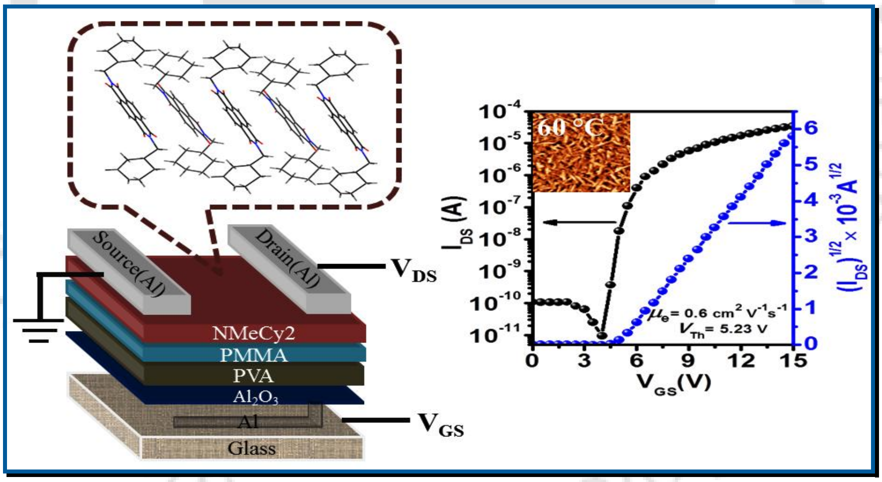

J. Phys. Chem. C **2015**, *119*, 12772-12779.

Abstract

The influence of structural ordering and their correlation with enhanced device performances is achieved using methyl cyclohexane appended naphthalene diimide (NMeCy2) thin films. The vacuum-deposited thin-film microstructure and morphology of NMeCy2 have been investigated using thin-film X-ray diffraction (XRD), atomic force microscopy (AFM), field emission scanning electron microscopy (FESEM) and were comparable with the bulk-phase crystalline structure and packing of NMeCy2. The organic field-effect transistor (OFET) was fabricated on a glass substrate consists of a bilayer polymer dielectric poly(methyl methacrylate) (PMMA) over poly(vinyl alcohol) (PVA) and an inorganic high-k dielectric Al_2O_3 as the third layer. NMeCy2 thermally deposited at an optimized substrate temperature (T_{sub}) of 60 °C displayed excellent molecular packing over a large area that ensued the improved field-effect performance with electron mobility (μ_e) value as high as 0.6 cm^2/Vs and current on/off ratio (I_{ON}/I_{OFF}) of 10^6 via modifications in dielectric configuration. Furthermore, the device afforded an unprecedented threshold voltage (V_{TH}) of 5.23 V with this material. We have been successful in developing a facile, reliable, and cheap method to tune the dielectric features which can culminate in improved field-effect transport properties.

3.1 Introduction

Electronic devices based on small organic molecules and polymers have received considerable attention in recent years due to their low cost and milder operating conditions. Particularly, small molecule based organic semiconductors (OSCs) are versatile, inexpensive, reliable, easily functionalized, and are used as active materials in organic light emitting devices (OLEDs),[1] organic photovoltaics (OPVs),[2] and organic field effect transistors (OFETs).[3] The key problems of these molecules are the low mobility and low environmental stability. High mobility in OFETs is a prerequisite for fast response in high speed device applications. On the other hand, OFETs impose serious limitations to their practical applications due to high operating and threshold voltage. Serious efforts have been devoted by researchers around the globe to improve these factors by designing molecules with superior properties, device engineering, controlling the roughness and morphology of the dielectric, and OSC layers. The growth of OSCs and the alignment of crystalline layers on the dielectric surfaces are the key requirements for achieving high mobility.[4] Generally, the hydrophobic surface is more favorable for the growth of OSCs than hydrophilic surfaces. Highly compact well organized molecular packing among adjacent molecules with significant π-orbital overlap and the absence of grain boundaries facilitate efficient charge transport enabling high mobility.[5] Low operating voltage is one of the main criteria for the integrated digital circuits and biosensor applications. The reduction in the threshold voltage and operating voltage can be achieved by using high-k dielectrics or by decreasing the thickness of the dielectric by using a combination of high-k/low-k dielectric layers (d) ($C_i = \varepsilon_0 k/d$).[6,7] There are very few reports on low V_{TH} for n-channel OFETs with SiO_2 or polymer as dielectric. The V_{TH} is one of the most important device parameters in field-effect transistors, which is directly related to the charge trapping at the interface of organic-dielectric materials. In particular, control of V_{TH} is very crucial for constructing integrated transistor circuits because a shift of V_{TH} to a lower value results in a decrease in power consumption together with a high circuit operation speed.[8]

Among the small molecule n-type materials, naphthalene diimides are well studied for their applications in organic electronic devices. Shukla *et al.* reported a cyclohexylsubstituted NTCDI derivative that displayed μ_e of 6.2 cm^2/Vs with I_{ON}/I_{OFF} and V_{TH} of 6×10^8 and ~58 V, respectively, on an OTS-modified SiO_2 substrate.[9] This is the highest μ_e reported so far among n-type OFETs due to the compact crystalline molecular packing in the thin-film phase.[10] However, from the recent report by Mori's group, the best values of μ_e, V_{TH}, and I_{ON}/I_{OFF} for the same material were found to be 0.52 cm^2/Vs, 44 V, and 10^6, respectively. It is relatively difficult to achieve lower V_{TH} with operating voltage below 100-120 V in this type of material as observed in this report.[11] It is well known that high mobility can be obtained only in certain crystallographic planes and directions. Hence, it is important to correlate the transport behavior with the crystal structure and packing of the molecule and examine whether the thin-film deposition plane corresponds to the preferred plane for charge transport.[12] Apart from this it is well-known that, in a typical OFET, the first few layers of molecules at the dielectric semiconductor interface are also responsible for charge transport.[13]

Herein, we report the synthesis of NMeCy2 and fabrication of n-channel OFETs using a stack of trilayer gate dielectric system (Al_2O_3/PVA/PMMA) to achieve high mobility and low operating voltage. Among high-k dielectrics, inorganic metal oxides are generally preferred. The reason for selecting an inorganic high-k Al_2O_3 dielectric layer is to provide high capacitance density and low leakage current. Among various polymer dielectric materials, PVA is highly versatile for OFETs due to its notable properties, viz. low leakage current, high dielectric constant, low temperature processing, good solubility in water, biocompatibility, low cost, and excellent film-forming abilities.[14,15] It is widely recognized that PVA-like high-k materials are preferred as the gate dielectric due to their driving of high capacitance in OFET operation. However, under humid conditions, PVA-based OFETs exhibit pronounced hysteresis in transfer characteristics[16-18] due to the charge traps at the semiconductor-dielectric interface which is because of the hydrophilic nature of PVA.[19] Hysteresis-free OFETs can be made using PVA dielectrics without any cross-linkers or photosensitizers by applying a thin interface layer of hydrophobic/less polar PMMA that inhibits charge trapping activities[20] and enhances large-scale, well-organized closely packed crystalline grains. Finally we optimized the fabrication of OFETs using a suitable stack trilayer combination of dielectrics, and the factors such as μ_e, V_{TH}, operating voltage, and I_{ON}/I_{OFF} ratio could be improved under reliable, low cost processing conditions. Thus, a trilayer dielectric system is employed to construct OFETs with n-type material that showed high performances under vacuum.[21]

3.2 Experimental

3.2.1 Materials and measurements

1,4,5,8-Naphthalene dianhydride, cyclohexyl methaneamine, quinoline, zinc acetate, and PMMA (MW=996000 g/mol) were purchased from Sigma-Aldrich and were used without further purification. PVA (MW = 89000-98000 g/mol) was purchased from Alfa-Aesar. ^{1}H NMR and ^{13}C NMR were recorded on were recorded on a Bruker Ascend 600 spectrometer. UV-VIS absorption spectra (both solution and thin film) were recorded on a Perkin Elmer Lambda 35 spectrometer. Emission spectra (both solution and thin film) were measured on a FluoroMax-4 spectrofluorometer. Electrochemical measurements were carried out on a CH instruments model 700D series consisting of a three-electrode system, viz., $Ag/AgNO_3$ as the reference electrode, platinum wire as the counter electrode, and glassy carbon as the working electrodes. Tetra-n-butyl ammonium hexafluorophosphate (TBAP) in acetonitrile solution (0.1 M) and ferrocene were used as a supporting electrolyte and internal reference respectively at a scan rate of 50 mV/s under an inert atmosphere. The thickness of the deposited films was optimized using a profilometer (Dektat-150). Using the Gaussian 03 software theoretical calculations were performed by the DFT method with B3LYP hybrid functional and a 6-31G basis set. Thermogravimetric analysis (TGA) and differential scanning calorimetry (DSC) were performed on METTLER TOLEDO (model TG/SDTA 851 e and model DSC 1, Stare system) under N_2 flow at a heating rate of 10 °C/min. Thin-film XRD analysis was done by a RIGAKU TTRAX III diffractometer. A single-crystal structure was obtained using a Bruker Nonius SMART APEX CCD diffractometer equipped with a graphite monochromator and an Apex CCD camera. The diffraction data were collected at room temperature with MoKα radiation ($\lambda = 0.71073$ Å). Structures were solved and refined by direct methods using SHELXS-97 and full-matrix least-squares on F^2. AFM images were recorded on an Agilent 5500 AFM/SPM microscope. Field emission scanning electron microscope (FESEM) images were recorded on a Sigma Carl ZEISS scanning electron microscope. The thickness of all the thin films were measured using Dektat-150 profilometer. All the electrical characterizations of OFET devices were carried out by Keithley 4200-SCS semiconductor parameter analyzer.

3.2.2 Synthesis of N, N'-bis(cyclohexylmethyl)naphthalene diimide (NMeCy2)

NMeCy2 molecule was synthesized following the procedure reported in literature by the direct condensation of 1,4,5,8-Naphthalene dianhydride with cyclohexyl methane amine with excellent yields in the range of 80-90%. A mixture of 1,4,5,8-Naphthalenetetracarboxylic acid anhydride (0.5 g, 1.8 mmol), cyclohexyl methaneamine (3g, 11.16 mmol), and zinc acetate (25 mg) in 15 mL quinoline was heated at 150 °C for 6h. The mixture was cooled to room temperature and diluted with several volumes of methanol. The resulting slurry was filtered; the collected solid was washed with methanol and dried in air. The crude product was then purified by column chromatography using hexane-chloroform as eluent. The crystals were grown by dissolving the product in DCM solution and kept it for slow evaporation to get light brown needle like crystals. Yield: 85%. ^{1}H NMR (600 MHz, $CDCl_3$, δ ppm): 8.74 (s, 4H), 4.08 (d, 4H), 1.89 (m, 2H), 1.66 (m, 8H), 1.19 (m, 12H). ^{13}C NMR (150 MHz, $CDCl_3$, δ ppm): 163.40, 131.23, 126.93, 126.78, 46.80, 36.92, 31.14, 29.89, 26.49, 26.03.

3.2.3 Device fabrication and measurements

OFETs were fabricated using bottom-gate, top-contact configuration. Herein, we utilized the low cost microscopic glass slides (roughness 1.8 nm) as the substrates for the fabrication of the devices on Al_2O_3/PVA/PMMA trilayer dielectric system. The glass substrates were kept in piranha solution (3:1 H_2SO_4:H_2O_2) for some time and finally washed with deionized water several times. The cleaned glass substrates were subsequently dried under vacuum at 100 °C. A patterned 150 nm thick aluminum gate electrode was deposited using a thermal evaporator onto the glass substrates. The top surface was anodized to get 10 nm of Al_2O_3 to reduce the leakage current and increase the capacitance by decreasing the thickness of the subsequent polymer layers. Anodization was carried out with a constant current of $j = 0.6$ mA cm^{-2} driven through the electrolyte. A 0.001 M citric acid monohydrate ($C_6H_8O_7{\cdot}H_2O$) was used to prepare electrolyte solution using ultrapure Milli-Q water. The aluminum-coated glass substrates were immersed into the electrolyte, which work as a working electrode (anode), and a platinum mesh served as the counter electrode (cathode). A Keithley 2400 source meter was used for supplying constant current. Constant current across the growing insulating Al_2O_3 layer was maintained by ramping up the voltage to a limiting anodization voltage (V_A), which was then maintained for several minutes until the current had completely decayed to below 5 μA. The thickness (d) of the resulting films can be controlled very precisely via the anodization voltage V_A, with $d=cV_A$, where c is the “anodization ratio” value for aluminum (1.3 nm/V). The samples were subsequently rinsed in high-purity Milli-Q water heated at 60 °C to remove the citric acid molecules and carefully dried in a hot plate at a temperature of 100 °C. The bilayer polymeric dielectrics of PVA and PMMA were prepared by spin-coating method. Initially, 3% PVA in water was spin coated at the rate of 3500 rpm for 60s on an anodized alumina (Al_2O_3) surface, and the samples were dried in a vacuum oven for 60 min at 80 °C. A 1% PMMA solution in anisole was then spin coated above the dried PVA layer at the same rate for the same time and dried in a vacuum oven for 60 min at 80 °C. The total thickness of the dielectric layer was optimized to ~110 nm i.e. (Al_2O_3(10 nm)/PVA(70 nm)/PMMA(30 nm)). The capacitance measurements on metal-insulator-metal (MIM) systems were carried out at 1 kHz-10 MHz at 30 mV modulation voltage with a Keithley 4200 SCS. A 60 nm thick film of NMeCy2 was deposited using thermal evaporation at a deposition rate of 0.4 Å/s under a base pressure of 5×10^{-6} mbar. Aluminum source and drain electrodes were deposited via thermal evaporation by using a shadow mask. The typical channel length (L) of the devices was 30 μm, and the channel width (W) was about 750 μm with width/length (W/L) as 25. The capacitance and electrical characteristics of OFET devices were carried out at room temperature in the dark under high vacuum using a Keithley 4200-SCS semiconductor parameter analyzer and a probe station (Lake Shore, $<1\times10^{-4}$ mbar) immediately after the devices were fabricated. The key device parameters such as μ_e, I_{ON}/I_{OFF}, and V_{TH} were extracted from transfer characteristics, using the formula in the saturation regime

$$I_{DS} = (\mu_e W C_i/2L)(V_{GS}-V_{TH})^2 \qquad (1)$$

where C_i denotes the capacitance of the gate dielectric per unit area.

3.3 Results and discussion

3.3.1 Synthesis and characterization of NMeCy2

NMeCy2 was synthesized in high yields (85%) by a direct condensation method (**Scheme 3.1**). The synthesized monomer was characterized by ^{1}H NMR and ^{13}C NMR spectroscopy (**Figure A3.1 and A3.2**).

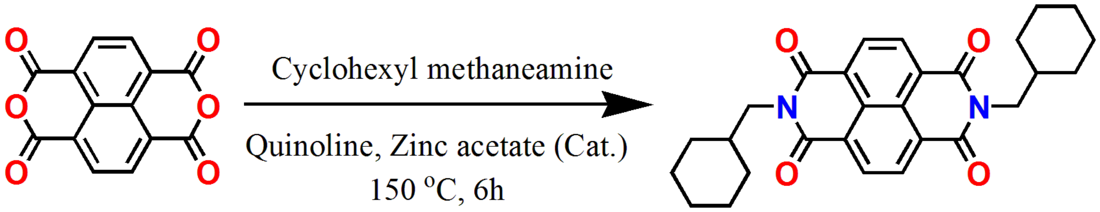

Scheme 3.1 Synthetic scheme of NMeCy2.

3.3.2 Photophysical properties

The absorption and emission properties of NMeCy2 were studied in both solution (DCM, 10^{-5} M) and thin-film (thickness 120 nm) phase (**Figure 3.1a and 3.1b**). The absorption spectra of NMeCy2 in solution showed three characteristic peaks at 381, 360, and 341 nm corresponding to the 0-0, 0-1, and 0-2 vibronic transitions, respectively. However, the absorption peaks in thin film was broadened and red-shifted by 10 nm, attributed to the formation of J-aggregates.[22] The optical band gap calculated using the absorption onset method was found to be 3.18 and 3.01 eV, respectively, for solution and thin-film phases. The emission spectra of NMeCy2 in solution exhibited three peaks at 385, 407, and 431 nm and a broad unstructured low intensity band appearing at 550 nm. The thin film exhibited a monomeric emission peak at 412 nm and a highly intense red-shifted emission peak at 560 nm confirming aggregation.

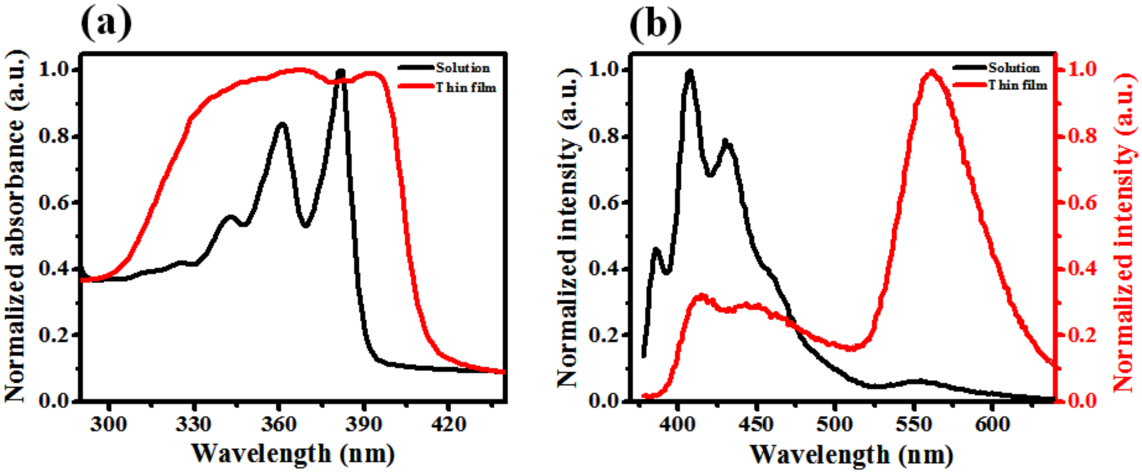

Figure 3.1 Normalized (a) absorption and (b) emission spectra of NMeCy2 in the solution and thin-film phase.

3.3.3 Electrochemical properties

The electrochemical properties of NMeCy2 were investigated by cyclic voltammetry (CV) measurements to find the HOMO and LUMO positions of the molecule. A representative cyclic voltammogram for NMeCy2 is shown in **Figure 3.2**. The obtained electrochemical data are presented in **Table 1**. No oxidation waves could be observed up to 2 V. NMeCy2 exhibited two (quasi) reversible one-electron reduction waves corresponding to the formation of a radical anion and dianion.

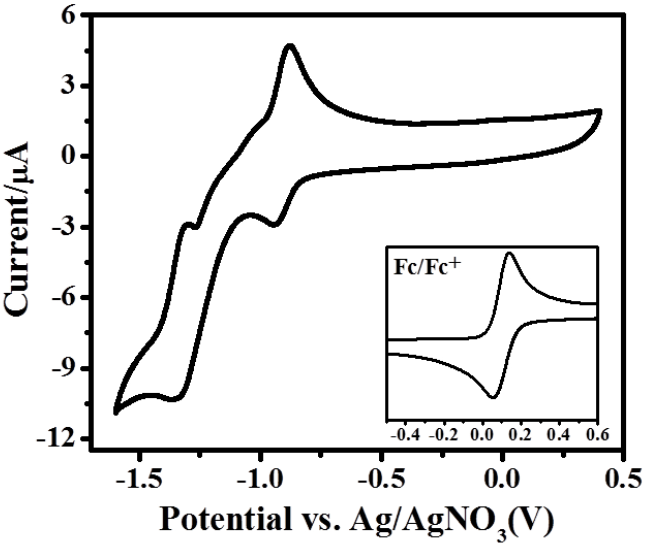

Figure 3.2 A typical cyclic voltammogram of NMeCy2 in CH_3CN. Inset: cyclic voltammogram of ferrocene used as reference.

The LUMO energy level was calculated using the following equation[23]

$$E_{LUMO}\ (eV) = -\ (E_{red\text{-}onset} + 4.8)$$

$$= -\ (E_{pc\text{-}onset} - E_{Fc} + 4.8)$$

The HOMO energy level was estimated based on the optical band gap obtained from solid state absorptiononset measurements.[24]

$$E_{LUMO} = -\ (E_{pc\text{-}onset} - E_{Fc} + 4.8)$$

$$= -\ (-1.32 - 0.09 + 4.8) = -\ 3.39\ eV$$

$$E_{HOMO} = E_{LUMO} - E_g^{optical}$$

$$= -\ 3.39 - 3.01$$

$$= -\ 6.40\ eV$$

($E_g^{optical}$ = 1240/λ eV = 1240/412 eV = 3.01 eV)

$E_g = E_{LUMO} - E_{HOMO}$ = 3.00 eV

3.3.4 Theoretical calculations

DFT calculations were carried out using gas-phase geometry optimization that reveal HOMO/LUMO energy levels as −7.13 eV/−3.59 eV and an energy gap of 3.54 eV which are in good agreement with the experimental values as shown in **Table 1**.

Table 1. E_{HOMO}, E_{LUMO}, and Band Gap (E_g) of NMeCy2 calculated from CV and DFT Calculation.

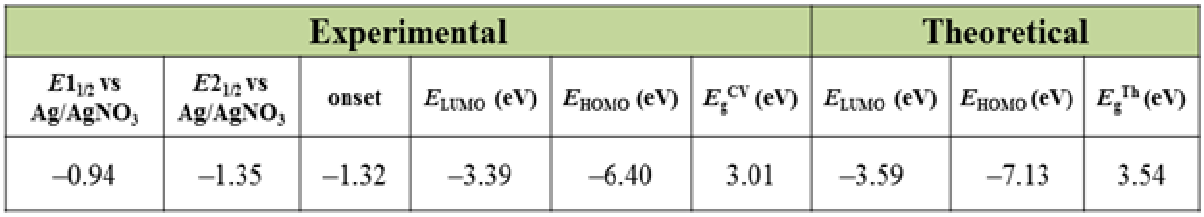

Experimental						Theoretical		
$E1_{1/2}$ vs Ag/AgNO$_3$	$E2_{1/2}$ vs Ag/AgNO$_3$	onset	E_{LUMO} (eV)	E_{HOMO} (eV)	E_g^{CV} (eV)	E_{LUMO} (eV)	E_{HOMO} (eV)	E_g^{Th} (eV)
−0.94	−1.35	−1.32	−3.39	−6.40	3.01	−3.59	−7.13	3.54

The HOMO and LUMO orbitals are shown in **Table 2.** It was also observed that methyl cyclohexane groups do not contribute to the frontier orbitals and are important only to attain the desired thin-film structural arrangement. The majority of the molecular orbital density was located mainly on C atoms along the C-C bonds.

Table 2. HOMO/LUMO orbital plots for NMeCy2 optimized geometries from DFT calculation.

HOMO	LUMO
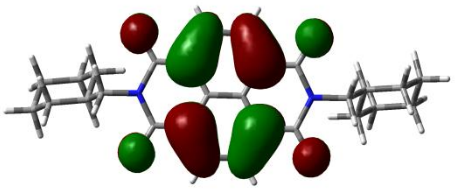	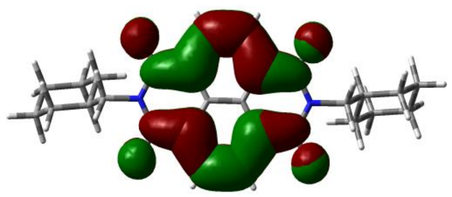

3.3.5 Thermal studies

The thermal stabilities of NMeCy2 were determined using TGA and DSC techniques (**Figure A3.3**). NMeCy2 exhibited excellent thermal stability with onset decomposition temperatures of around 305 °C under an inert gas environment. During DSC studies, a sharp transition at 334 °C was observed upon first heating that corresponds to melting of NMeCy2, while on second cooling the transition occurred at 288 °C. An evaporation temperature of NMeCy2 was optimized as 260 °C via TGA/DSC data using a ceramic crucible in high vacuum thermal evaporator. Thus, the thermal stability of the NMeCy2 is adequate for applications in optoelectronic devices.

3.3.6 Single crystal XRD and pattern of packing in the solid state

The structural information on NMeCy2 was obtained by single-crystal X-ray analysis (**Figure 3.3a and 3.3b**). Crystallographic studies confirm the system as triclinic with P-1 space group (a = 8.038(2) Å, b = 8.7402(19) Å, c = 17.845(4) Å, α = 100.535(9)°, β = 97.165(9)°, γ = 93.721(8)°, Z = 1), unlike monoclinic as reported for the cyclohexyl substituted NTCDI molecule[9] (**Table A3.1)**. The crystal packing structure of the molecule displayed a flip-flap stacking (**Figure 3.3c**) to minimize the steric hindrance between methyl cyclohexane side chains. It is evident that π-π stacking between neighboring moieties was not

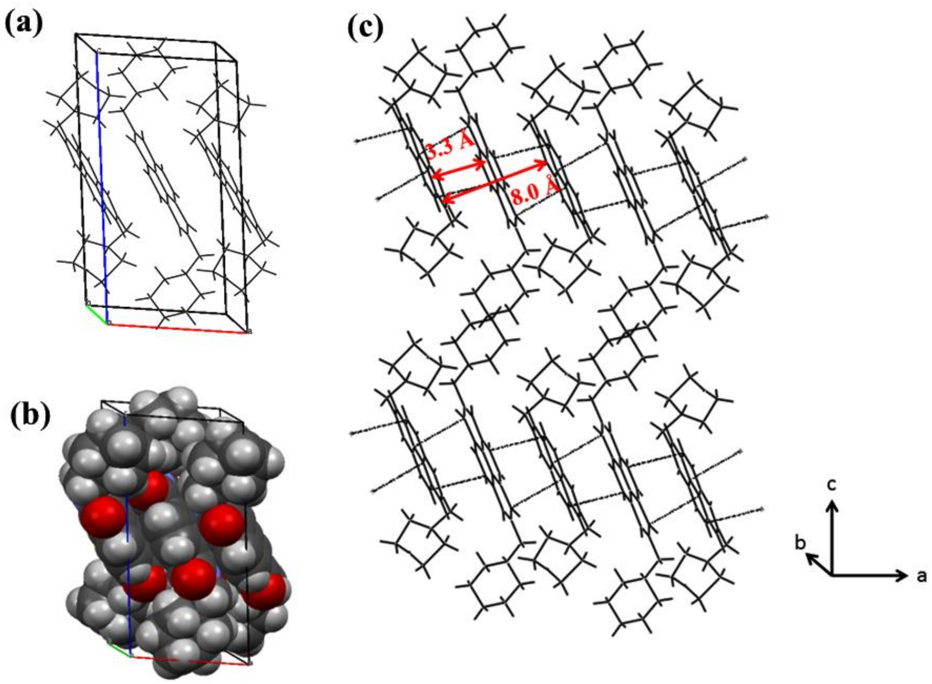

Figure 3.3 (a) Crystal structure of the unit cell, (b) space filling model, and (c) packing arrangement showing the shortest distance between two neighboring and two identical units in the crystal.

completely cofacial but was slightly tilted with the shortest distance of around 3.3 Å. However, the distance between two similarly aligned molecules was observed to be ~8 Å. The observed intermolecular distance is comparable to the π-π stacking distance commonly observed in cofacially packed linear acenes, i.e., 3.4-3.5 Å, which is required for strong electronic coupling and good charge mobility.[25] The energy minimization calculations on a stacked dimer at a fixed stacking distance of 3.3 Å give strong evidence for flip-flap intermolecular stacking that minimizes the steric hindrance between the methyl cyclohexane side chains. The total energy of the dimer decreases sharply upon rotating the molecules from zero degree and reaches the most stable stacking conformation at a rotation angle of 42.5 °C (**Figure A3.4 and A3.5**). This dense packing facilitates the efficient charge transport in the crystals.

3.3.7 OFET device characteristics

To explore the semiconducting properties of NMeCy2 at different T_{sub}, OFET devices were fabricated with bottom-gate, top-contact configuration using trilayer gate dielectric materials. NMeCy2 used as the active layer was deposited by vacuum sublimation using a thermal evaporator. The schematic diagram of the device structure is illustrated in **Figure 3.4**, and the devices were tested under vacuum (~10^{-4} mbar) immediately after fabrication. The OFET devices were fabricated by growing the organic semiconductor film at different T_{sub} = RT, 60, 90, and 120 °C to monitor the effect and influence of T_{sub} on charge transport properties. Except the device set at T_{sub} = 60 °C, others displayed very poor μ_e value with relatively

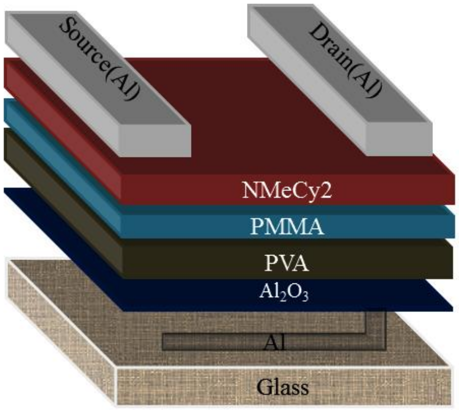

Figure 3.4 Schematic illustration of the OFET device fabricated on a trilayer dielectric system.

lower I_{ON}/I_{OFF} (**Table A3.2**) confirming that T_{sub} is a key parameter in self-assembled growth of OSC layers at the dielectric-semiconductor interfaces which improves the charge carrier mobility and other OFET parameters. To arrive at some intricate correlation between device properties and its constituent layers, it is necessary to characterize each individual layer present in the device structure.

3.3.8 Thin film morphology and structural characterization of dielectric layers and the dielectric-NMeCy2 interface at different T_{sub}

The thin-film morphology and structural characterization of both dielectric materials and the dielectric-NMeCy2 interface is investigated by AFM, FESEM, and thin-film XRD analysis.

3.3.8a AFM analysis

Generally, surface roughness of the gate dielectric is an important parameter that affects the device performance. Rough interfaces hinder the charge transport in the semiconductor by disturbing the morphology of the organic semiconductor layer or by acting as physical traps. The typical surface morphology of the Al gate electrode, anodized Al_2O_3, spin-coated PVA on anodized Al_2O_3, and a thin layer of PMMA on Al_2O_3/PVA dielectric (**Figure 3.5**) and organic semiconductor (NMeCy2) deposited on trilayer dielectric at different T_{sub} were studied by AFM (**Figure 3.6**). The Al gate electrode after thermal deposition shows a RMS surface roughness (R_q) of 6.27 nm which after anodization gives a very rough anodized Al_2O_3 film of R_q=27.8 nm. After deposition of polymer dielectric PVA, the roughness decreases up to 1.97 nm. A highly smooth and compact surface is a prerequisite for the growth of quality film, which would eventually result in efficient charge coupling between dielectric material and the channel. Finally, a flat homogeneous surface of R_q=0.21 nm was obtained by covering the hydrophilic PVA dielectric layer by a very thin hydrophobic PMMA layer. The hydrophobic surface has a better interaction with organic semiconductors and passivates the scattering sites to improve the device performance. The large-scale ordered growth alignment of organic molecules over the dielectric layer helps form efficient, interconnected charge transport routes. **Figure 3.6** shows the AFM topography images of an organic semiconductor (NMeCy2) deposited on a trilayer dielectric system at different T_{sub}. From the AFM images of dielectric-NMeCy2 films at different T_{sub}, we could deduce a fairly good microstructure/morphology-mobility correlation. Generally, with an increase in T_{sub},

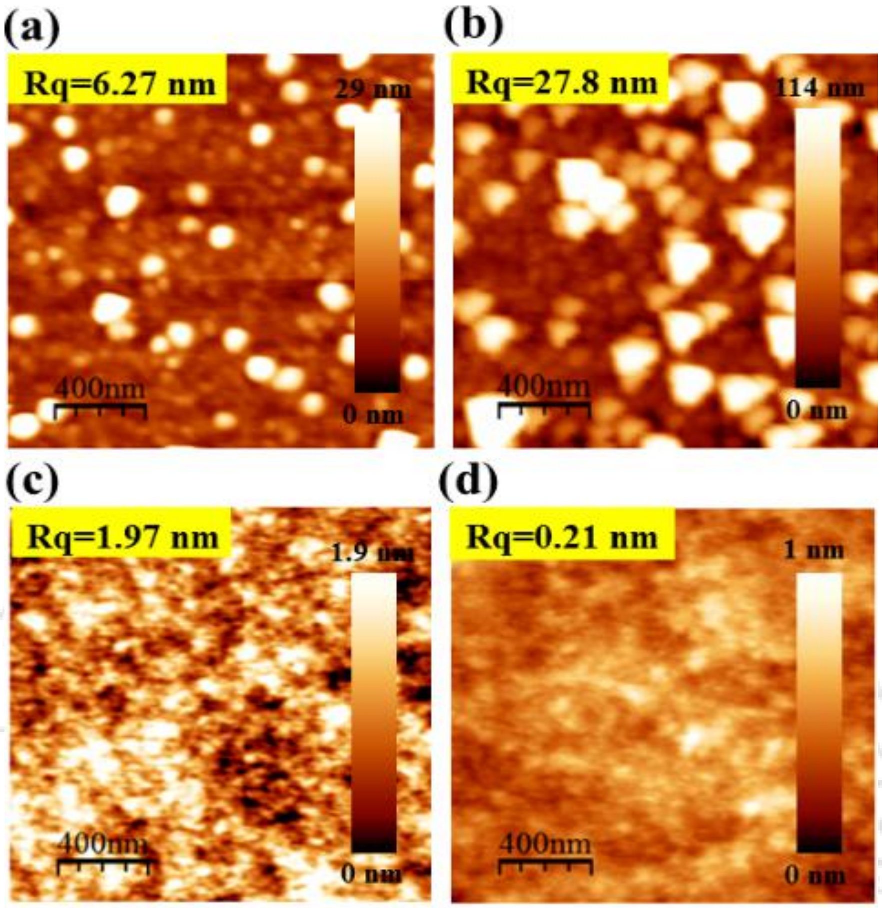

Figure 3.5 2 × 2 μm^2 AFM images of the (a) Al gate electrode, (b) anodized Al_2O_3 layer, (c) spin-coated PVA on anodized Al_2O_3, and (d) spin-coated PMMA layer on anodized Al_2O_3/PVA layer.

the molecules gain certain thermal energy and move faster on the substrate, and the alignment would change with the diffusion rate. This led to different morphology with various T_{sub}. At RT, though the topography image showed small crystallites with compact film morphology, due to the lack of thermal activation, the charge transport is not pronounced which directly affects the carrier mobility. The AFM images of crystalline domains undergo change when T_{sub} was increased above 60 °C. At T_{sub}=60 °C the dielectric-NMeCy2 surface shows crystals of around 1 µm in size in addition to the closely compacted grains with R_q=3.5 nm. After increasing the T_{sub} above 60 °C, i.e., 90 and 120 °C, the continuous grains disintegrate into single elongated ones with apparently a larger number of grain gaps separating each other compared to T_{sub}=60 °C which can act as charge trapping sites. The distinct morphological evolution at 90 and 120 °C may be due to the loss in viscoelasticity of the polymer dielectric films heating above its glass transition temperature.

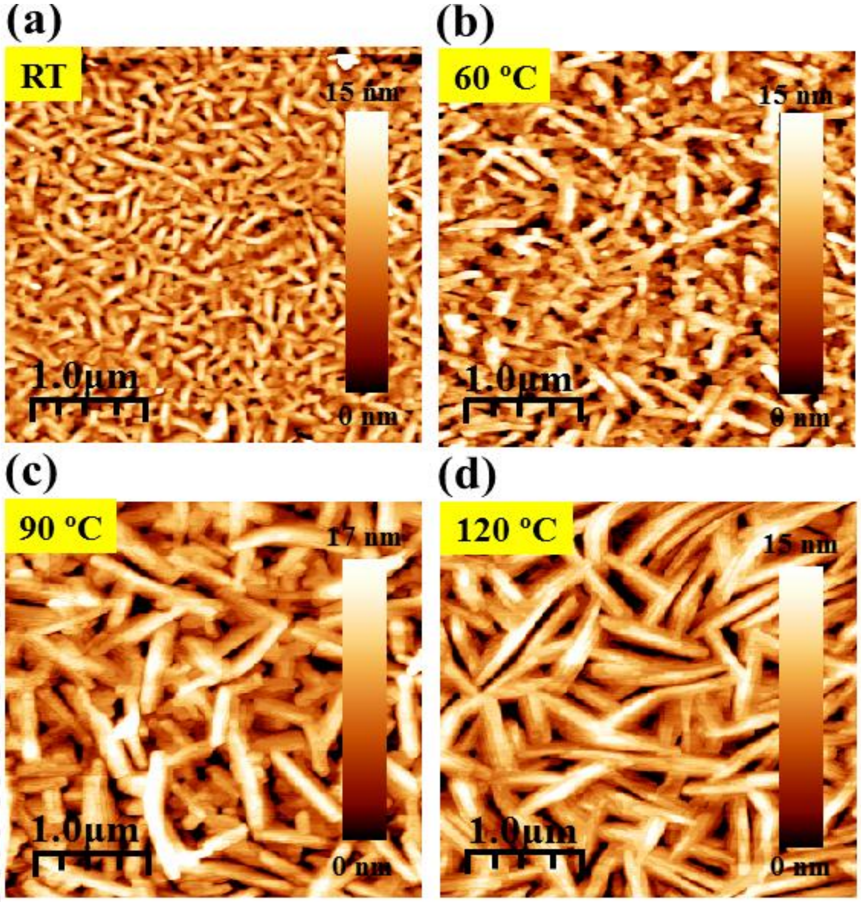

Figure 3.6 5 × 5 μm^2 AFM images of NMeCy2 at T_{sub} (a) RT, (b) 60 °C, (c) 90 °C, and (d) 120 °C.

As the interface degrades the continuity of NMeCy2, the film was severely affected which resulted in alteration of crystalline packing of the molecules at the dielectric-semiconductor interface. The existence of dielectric-NMeCy2 interfacial changes in morphology at higher T_{sub} resulted in mobility degradation. The devices fabricated at T_{sub}=60 °C exhibited superior field-effect behavior which is assigned to the better interconnection and tighter packing between grains that reduces the charge trapping states at the boundaries to enhance the current in the channel. On the contrary, at elevated temperature the large dendritic grains with immense voids existing in the first few NMeCy2 layers contribute to the hindrance in smooth charge transport through the OSC channel and finally reduce the carrier mobility drastically compared to the device at T_{sub}=60 °C.

3.3.8b FESEM analysis

Figure 3.7 shows FESEM images of the anodized Al_2O_3 layer, spin-coated PMMA layer on anodized Al_2O_3/PVA layer, and thermally deposited NMeCy2 film on stack Al_2O_3/PVA/PMMA at T_{sub}=60 °C. The anodized Al_2O_3 layer displayed a rough surface with small seed-like structures. After spin coating PVA and a thin layer of PMMA on anodized Al_2O_3, a uniform smooth film without any pores and voids was observed. A uniform and highly smooth dielectric surface is desirable for the growth of NMeCy2 semiconductor film. The FESEM image (**Figure 3.7c)** of NMeCy2 film on anodized Al_2O_3/PVA/PMMA at T_{sub}=60 °C exhibits an interconnected network of grains which results in better device properties.

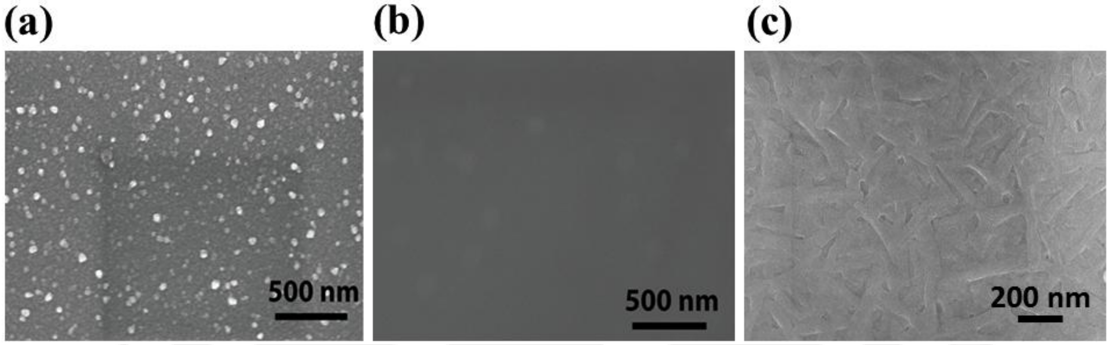

Figure 3.7 FESEM images of the (a) anodized Al_2O_3 layer, (b) spincoated PMMA layer on anodized Al_2O_3/PVA layer, and (c) deposited NMeCy2 layer on Al_2O_3/PVA/PMMA at T_{sub}=60 °C.

3.3.8c Thin film XRD study

The XRD patterns of thermally deposited NMeCy2 film at T_{sub}=60 °C were compared with the simulated pattern obtained from single-crystal XRD data to investigate the molecular packing of NMeCy2 (**Figure 3.8a and 3.8b**). The simulated XRD pattern exhibits peaks with multiple reflections, while thin films deposited on glass substrate showed only three sharp peaks in the 5° to 50° range of 2θ. The amorphous hump at ~2θ=25° is due to the diffraction from the glass substrate. In both the conditions primary peaks appeared at ~2θ=5.1°, corresponding to a d-spacing of 17.3 Å which is close to the length of the c-axis of the

NMeCy2 unit cell and is therefore attributed to (001) reflections as obtained from crystal data. The lower d001 value (17.3 Å) and this difference indicates a tilted orientation of the molecule on the substrate.[27] The tilt angle with respect to the substrate normal is given by $\cos^{-1}$ (17.3/17.8)=13.6°.[28] The second and third order diffraction peaks appear at 2θ=10.2° (d-spacing = 8.7 Å) and 2θ=20.4° ($d_{spacing}$=4.3 Å). The d-spacing of 8.7 Å measured from thin film XRD confirms flip-flap stacking as observed in the case of single-crystal packing, for which the shortest distance between two identical molecules in the crystal unit is typically 8.0 Å. In addition, the appearance of a diffraction peak at 2θ=20.4° is assigned to the π-π stacking and implies the existence of effective intermolecular π-orbital overlap. The match between the peak pattern obtained from the simulation of single-crystal data and the deposited thin film suggests that the growth of thin film is similar to that in bulk crystal. All

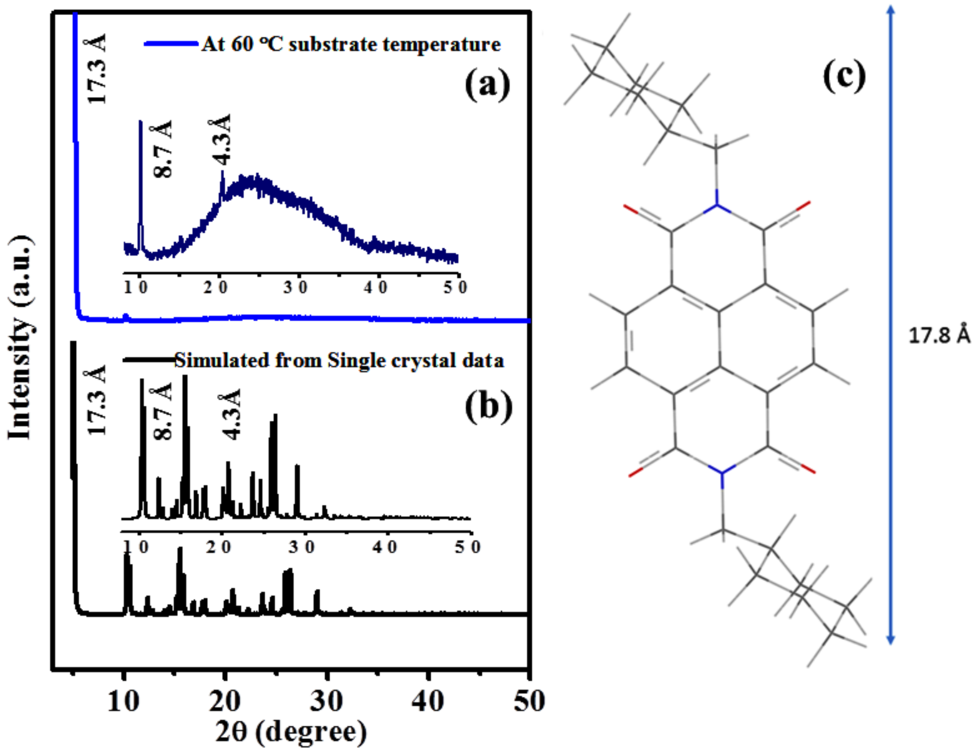

Figure 3.8 (a) Thermally deposited thin-film XRD pattern of NMeCy2 on a glass substrate at T_{sub}=60 °C. (b) Simulated XRD (from single crystal) pattern of NMeCy2. (Inset: expanded area of XRD from 2θ=8° to 50°.) (c) Molecular length (17.8 Å) of NMeCy2 as calculated from DFT.

the observations on morphological and structural characterization of thin films support the better device performance of NMeCy2 at T_{sub}=60 °C.

3.3.9 Transistor properties

The OFET device fabricated at T_{sub}=60 °C on trilayer (Al_2O_3/PVA/PMMA) dielectric displayed very good linear and saturation behavior under output characteristic curves as shown in **Figure 3.9a**. The data presented here are the average of the ∼10 devices in all the cases. All the devices reached the saturation region within the operating voltage 15 V. From the transfer characteristic curve (**Figure 3.9b**), the plot of log I_{DS} and square root of I_{DS} as a function of V_{GS} gives V_{TH}, μ_e, and I_{ON}/I_{OFF} to be 5.23 V, 0.6 cm^2/Vs, and 10^6, respectively. This is one of the rare low operating voltage devices with low threshold voltage and high mobility compared to the devices fabricated with similar type of molecules. The average subthreshold swing value was observed to be 0.23 V/decade, which yields an interface trap density (N_{Trap}) of 8.94×10^{11} cm^{-2} e V^{-1}, derived from the equation

$$N_{Trap} = \left[\frac{S.\log(e)}{kT/q} - 1 \right] . \frac{C_i}{q}$$

where S denotes subthreshold swing; k is Boltzmann's constant; T represents the absolute temperature; and C_i is 50 nF/cm^2. The trap density at the interface with the trilayer dielectric is calculated to be near 10^{12} cm^{-2} e V^{-1} which is lower than the best values reported for OFETs.[29] This relatively lower N_{Trap} value for this device supports the formation of a good dielectric-NMeCy2 interface and is a very important factor to achieve high mobility. The summary of device characterization data is presented in **Table 3**.

Table 3. Summary of device characterization data fabricated on the trilayer dielectric system.

Substrate	**Dielectric**	**T_{Sub} (°C)**	**S (V/decade)**	**N_{trap} (cm^{-2} eV^{-1})**	**I_{ON}/I_{OFF}**	**μ_e (cm^2/Vs)**	**V_{TH} (V)**
Glass	Al_2O_3/PVA/ PMMA	60	0.27	1.15×10^{12}	10^6	0.6	5.23

T_{Sub}: Substrate temperature, S: Sub-threshold swing, N_{trap}: Interface trap density, I_{ON}/I_{OFF}: On/off current ratio, μ_e: Electron mobility in saturation regime, V_{TH}: Threshold voltage.

3.4 Conclusion

In conclusion, we have demonstrated the significance of trilayer dielectrics to tune the performance of n-channel OFET based on methyl cyclohexane functionalized NMeCy2. By employing trilayer dielectric system, we can effectively reduce the operating voltage as well as threshold voltage without affecting μ_e and I_{ON}/I_{OFF} values by promoting ordered growth of NMeCy2 with interconnected charge transport paths. The n-channel NMeCy2 based OFET device exhibited a saturation regime μ_e value of 0.6 cm^2/Vs. We could successfully lower the V_{TH} value up to 5.23 V and achieved high I_{ON}/I_{OFF} of 10^6, which is one of the best performing devices among n-channel OFETs. The enhanced performances of the OFET device are attributed to the well-directed close intermolecular π-stacking in thin films over a large scale, the superior film forming ability of NMeCy2 at the trilayer dielectric/semiconductor interface, and reduced interfacial defects. The phenomena happening at the interface between the gate dielectric layer and the active channel have been marked as being closely connected to the overall device operation and performance. Our concept of trilayer dielectric with inorganic high-k metal-oxide and organic polymer based high-k/low-k dielectric stacked arrangement demonstrates a significant step toward fabricating cost-effective, easy processed, high performance organic electronic devices.

3.5 References

(1) Tang, C. W. *Appl. Phys. Lett.*, **1986**, *48*, 183.

(2) Tang, C. W.; VanSlyke, S. A. *Appl. Phys. Lett.*, **1987**, *51*, 913.

(3) Tsumura, A.; Koezuka, K.; Ando, T. *Appl. Phys. Lett.*, **1986**, *49*, 1210.

(4) Geyer, F. L.; Pun, A.; Hanifi, D.; Bunz, U. H. F.; Liu, Y. *J. Mater. Chem. C* **2013**, *1*, 6661.

(5) Li, L.; Tang, Q.; Li, H.; Yang, X.; Hu, W.; Song, Y.; Shuai, Z.; Xu, W.; Liu, Y.; Zhu, D. *Adv. Mater.*, **2007**, *19*, 2613.

(6) Veres, J.; Ogier, S.; Lloyd, G. *Chem. Mater.*, **2004**, *16*, 4543.

(7) Su, Y.; Wang, C.; Xie, W.; Xie, F.; Chen, J.; Zhao, N.; Xu, J. *ACS Appl. Mater. Interfaces* **2011**, *3*, 4662.

(8) Dao, T. T.; Matsushima, T.; Friedlein, R.; Murata, H. *Org. Electron.*, **2013**, *14*, 2007.

(9) Shukla, D.; Nelson, S. F.; Freeman, D. C.; Rajeswaran, M.; Ahearn, W. G.; Meyer, D. M.; Carey, J. T. *Chem. Mater.*, **2008**, *20*, 7486.

(10) Locklin, J.; Li, D.; Mannsfeld, S. C. B.; Borkent, E. J.; Meng, H.; Advincula, R.; Bao, Z. *Chem. Mater.*, **2005**, *17*, 3366.

(11) Kakinuma, T.; Kojima, H.; Ashizawa, M.; Matsumoto, H.; Mori, T. *J. Mater. Chem. C* **2013**, *1*, 5395.

(12) Adiga, S. P.; Shukla, D. *J. Phys. Chem. C* **2010**, *114*, 2751.

(13) Zhang, H.; Guo, X.; Hui, J.; Hu, S.; Xu, W.; Zhu, D. *Nano Lett.*, **2011**, *11*, 4939.

(14) Huang, W.; Shi, W.; Han, S.; Yu, J. *AIP Adv.*, **2013**, *3*, 052122.

(15) Etten, E. A. V.; Ximenes, E. S.; Tarasconi, L. T.; Garcia, I. T. S.; Forte, M. M. C.; Boudinov, H. *Thin Solid Films* **2014**, *568*, 111.

(16) Majewski, L. A.; Schroeder, R.; Grell, M. *Adv. Mater.*, **2005**, *17*, 192.

(17) Park, J.; Park, S. Y.; Shim, S. O.; Kang, H.; Lee, H. H. *Appl. Phys. Lett.*, **2004**, *85*, 3283.

(18) Tsai, T. D.; Chang, J. W.; Wen, T. C.; Guo, T. F. *Adv. Funct. Mater.*, **2013**, *23*, 4206.

(19) Chesterfield, R. J.; McKeen, J. C.; Newman, C. R.; Frisbie, C. D.; Ewbank, P. C.; Mann, K. R.; Miller, L. L. *J. Appl. Phys.*, **2004**, *95*, 6396.

(20) Ukah, N. B.; Granstrom, J.; Gari, R. R. S.; King, G. M.; Guha, S. *Appl. Phys. Lett.*, **2011**, *99*, 243302.

(21) Subbarao, N. V. V; Gedda, M.; Iyer, P. K.; Goswami, D. K. *ACS Appl. Mater. Interfaces* **2015**, *7*, 1915.

(22) Spano, F. C. *Annu. Rev. Phys. Chem.*, **2006**, *57*, 217.

(23) Vasimalla, S.; Senanayak, S.; Sharma, M.; Narayan, K. S.; Iyer, P. K. *Chem. Mater.*, **2014**, *26*, 4030.

(24) Kolhe, N. B.; Devi, R. N.; Senanayak, S. P.; Jancy, B.; Narayan, K. S.; Asha, S. K. *J. Mater. Chem.*, **2012**, *22*, 15235.

(25) Shukla, D.; Welter, T. R.; Robello, D. R.; Giesen, D. J.; Lenhard, J. R.; Ahearn, W. G.; Meyer, D. M.; Rajeswaran, M. *J. Phys. Chem. C* **2009**, *113*, 14482.

(26) Maunoury, J. C.; Howse, J. R.; Turner, M. L. *Adv. Mater.*, **2007**, *19*, 805.

(27) Gawrys, P.; Djurado, D.; Rimarcik, J.; Kornet, A.; Boudinet, D.; Jean-Marie, V.; Lukes, V.; Wielgus, I.; Zagorska, M.; Pron, A. *J. Phys. Chem. B* **2010**, *114*, 1803.

(28) Facchetti, A.; Mushrush, M.; Yoon, M. H.; Hutchison, G. R.; Ratner, M. A.; Marks, T. J. *J. Am. Chem. Soc.*, **2004**, *126*, 13859.

(29) McDowell, M.; Hilla, I. G. *Appl. Phys. Lett.*, **2006**, *88*, 073505.

3.6 Appendix

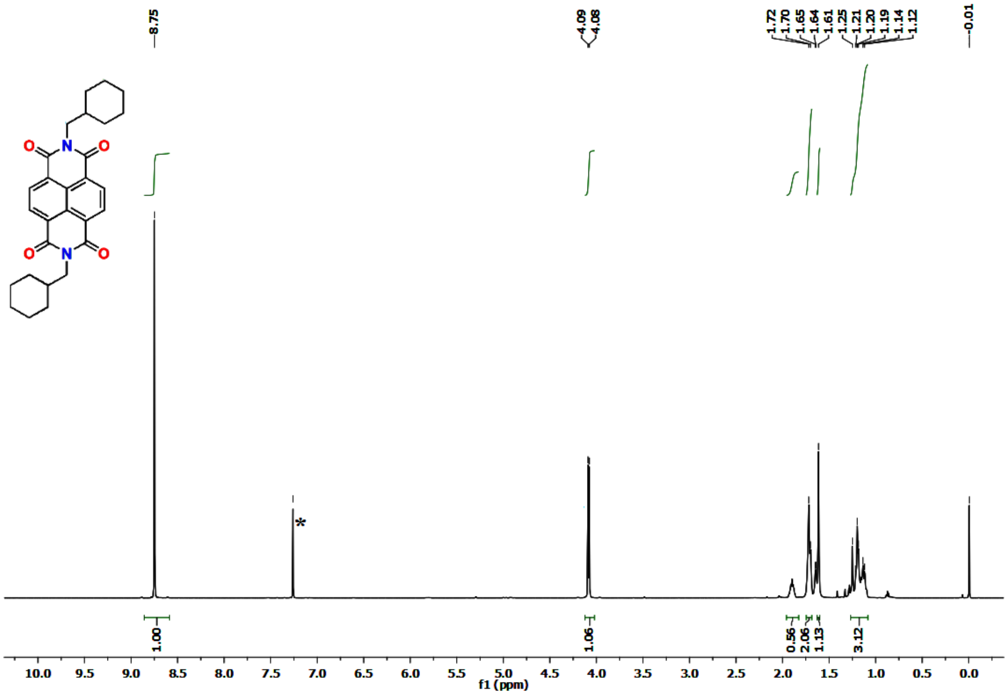

Figure A3.1 ^{1}H NMR (600 MHz, $CDCl_3$) spectra of NMeCy2.

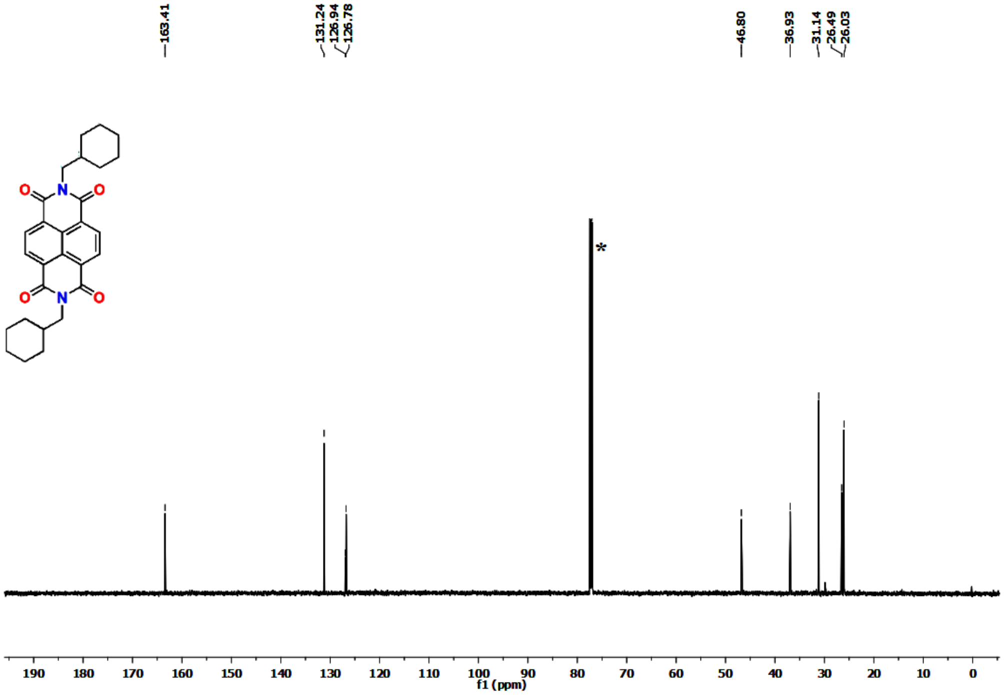

Figure A3.2 ^{13}C NMR (150 MHz, $CDCl_3$) spectra of NMeCy2**.**

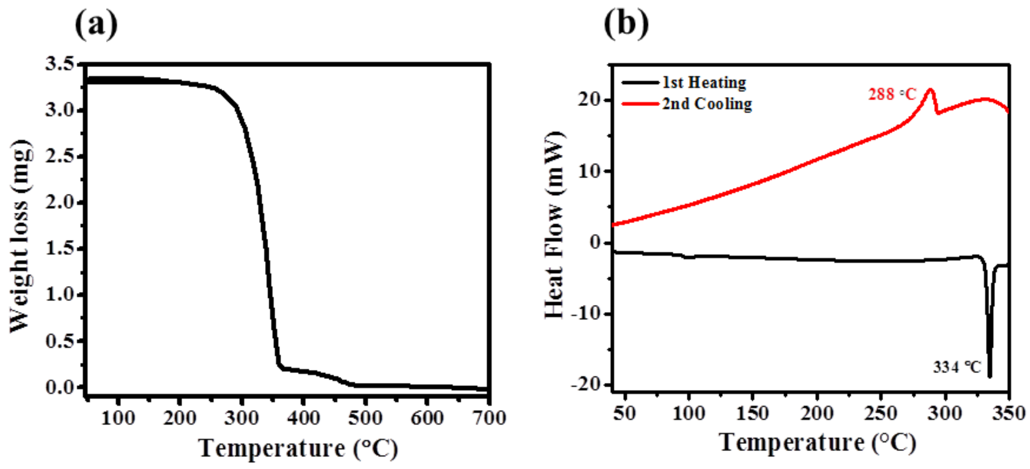

Figure A3.3 (a) TGA and (b) DSC plots of NMeCy2 at a heating rate of 10 °C/min under N_2.

Table A3.1. The crystallographic data from single crystal XRD.

The crystallographic data for the structure of NMeCy2 have been deposited with the Cambridge Crystallographic Data Centre as supplementary publication no. CCDC-1045824. These data can be obtained free of charge from www.ccdc.ac.uk/data.request/cif.

empirical formula	C56 H58 N4 O8
formula weight	915.06
crystal system	Triclinic
space group	P-1
T(K)	296
Wavelength/ Å	0.71073
Radiation type	MoK\α
a/Å	8.038(2)
b/Å	8.7402(19)
c/Å	17.845(4)

α/deg	100.535(9)
β/deg	97.165(9)
γ/deg	93.721(8)
V / Å^3	1218.0(5)
D_{calcd} (g cm^{-3})	1.248
μ (mm^{-1})	0.084
Z	1
reflns collected	5696
Observed reflns	2151
R_1[I> 2σ(I)]	0.1015
wR2(all)	0.2497
goodness-of-fit	1.166

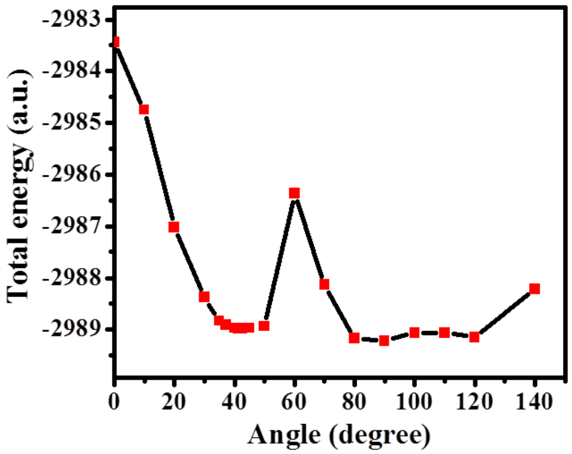

Figure A3.4 DFT calculation on stacked dimers at B3LYP/6-31G level showing total energy vs rotation angle of stacked dimer.

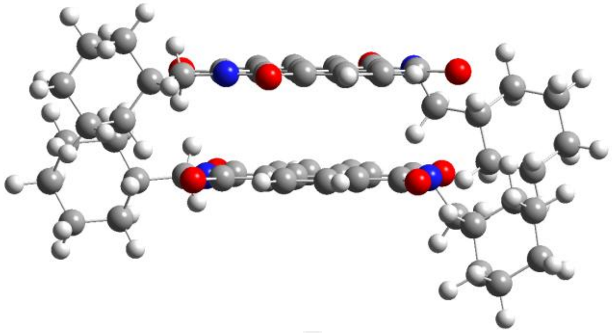

Figure A3.5 The angle that minimizes the steric repulsion between two molecules is found to be 42.5°.

Table A3.2. Device data at various substrate temperatures (T_{sub}) are summarized below.

T_{sub} (°C)	I_{ON}/I_{OFF}	μ_e (cm^2/Vs)
RT	10^3	7×10^{-4}
60	10^6	0.6
90	10^2	6.7×10^{-5}
120	10^1	2×10^{-4}

Chapter 4

Vapor Phase Sensing of Ammonia at Sub-ppm Level Using Perylene Diimide Thin Film Device

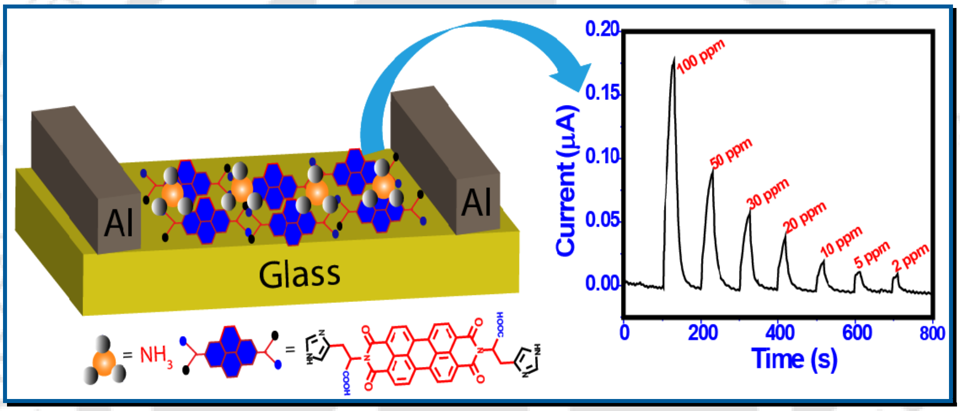

J. Mater. Chem. C **2015**, *3*, 10767-10774.

Abstract

The fabrication of a two terminal sensor device based on histidine substituted perylene diimide (PDI-HIS) thin film for the sensitive detection and quantification of ammonia (NH_3) vapors by monitoring the changes in its current intensity is described at room temperature under ambient conditions. The thin film morphological variations of the drop casted PDI-HIS films before and after exposure to NH_3 vapors are characterized by FESEM and TEM confirming the diffusion/adsorption of the NH_3 vapors. The solution cast PDI-HIS thin film gas sensor device exhibited rapid, highly sensitive and selective vapor phase response towards NH_3 with a detection limit as low as 0.56 ppm which is much lower than the maximum permissible limit set for NH_3 (25 ppm) for prolonged exposure. Furthermore, control sensing experiments were performed using alkyl substituted PDI (PDI-n-octyl) demonstrated that the presence of histidine groups at the imide position of PDI-HIS drastically affects the solid-state aggregation mode as well as redox potential that ultimately enhances the sensing response of the device. The key performance parameters of the device such as sensitivity, response/recovery time, selectivity, recyclability, stability and detection limit demonstrated the protocol as simple, reliable, cost-effective and most efficient in performing NH_3 detection under very realistic conditions.

4.1 Introduction

Electrical sensors have received remarkable attention owing to their ease in the analysis of information during detection of various analytes through electrical signals.[1] Moreover, the development of a semiconductor sensor device is simple, since the signal does not necessitate intricate detection kits. Among electrical sensors, three-terminal transistors and two-terminal resistors are the most promising candidates for the advancement of low-cost, portable, low power consuming and selective sensing devices for applications in chemical, biological and physical monitoring.[2] Such ultrasensitive sensors can be utilized in detecting traces of various toxic gases and volatile organic compounds (VOCs) even at remote locations.[3] Ammonia (NH_3) detection has received immense attention among various volatile species owing to its severe effect on the environment as well as human health.[1] NH_3 is highly toxic and corrosive that can be easily spread into the environment due to its widespread applications in fertilizers, refrigeration systems, manufacturing of dyes, drugs, synthetic fibers, plastics, etc.[4] Moreover, ammonium nitrate (NH_4NO_3) found in many explosives gradually decomposes to release trace amounts of NH_3 which are essential to be monitored in order to prevent the lethal accidents.[5] Ammonia, in its flammability range of 15% to 28% by volume can easily explode or catch fire.[6] Although, it finds applications in various sectors, its exposure in high concentrations is a major threat to the human health. The lower limit of human NH_3 perception by smell is around 50 ppm.[7] However, even below this limit, it is irritating to the respiratory system, skin as well as eyes.[8,9] The long term (8 h) permissible concentration of NH_3 for workers is 25 ppm.[10] Therefore, it is highly desirable to design and fabricate a long-term-reliable, highly-sensitive, miniaturized, room-temperature-efficient and low power consuming NH_3 gas sensor, which can detect and monitor NH_3 concentration surrounding the environment in real time.

In the past decade, there have been numerous reports on NH_3 detection based on nanostructured metal oxides,[11-16] plasmophores,[17] conducting polymers,[18-22] carbon nanotubes[23-25] and nanostructured graphenes.[26-29] However, a very few small molecule based sensors[30-35] with improved properties such as lower operating temperature, high stability, fast response/recovery time, high selectivity and low detection limit have been reported.[36] Among small molecules, perylene diimide derivatives (PDIs) are an important class of materials for the fabrication of devices due to their numerous features such as high absorption coefficient, good chemical and thermal stability, better electronic properties and excellent photostability. Owing to their unique features, these materials have found versatile applications in organic field-effect transistors (OTFTs), organic solar cells and sensor devices.[37-39] Recently, various types of PDIs composed of self-assembled aggregates, nanorods, nanobelts, nanofibres etc. have been developed for detecting volatile species such as amines, explosives, etc.[40,41] Molecular modification has a vital role in improving the performance of such PDI-based organic semiconductor devices. In this context, modifications of PDIs have been achieved by either substituting electron withdrawing groups at the core position[42] (so called bay position) or introducing solubilizing groups at the imide position.[43] Amino acids have achieved much attention as active groups to tune the structure of PDIs at the imide position, since they can deliver a range of supramolecular structures with variable degrees of arrangement due to the site-specific hydrogen bonding.[44] Though, most of the efficient sensor devices reported for NH_3 detection are based on the functionalization of perylenes at the core position[45,46] the imide position has been modulated mainly for providing solubility to the system. Hence, meagre attention has been paid in designing perylene derivatives with suitable receptors at the imide position that can be utilized as tools to fabricate devices with a specific aim of sensing gases such as NH_3 with high sensitivity and selectivity.

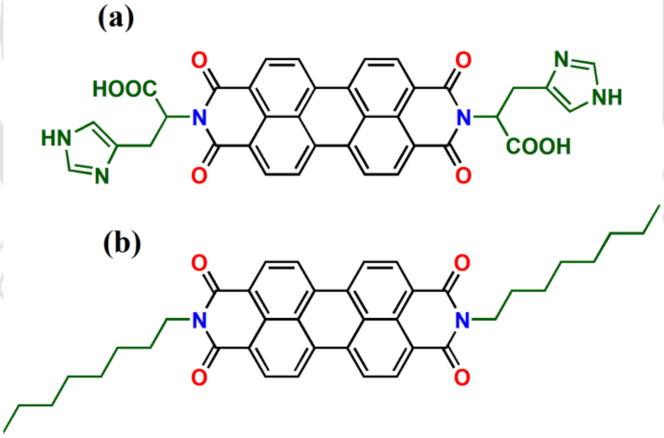

Scheme 4.1 Structure of the PDI derivatives (a) PDI-HIS and (b) PDI-n-octyl used for the sensing studies.

Herein, we report the fabrication of a low cost two terminal sensor device using a PDI-HIS (**Scheme 4.1a**) thin film as an active layer and systematically investigated its sensing response towards NH_3 vapors by measuring the variation of current intensity. The sensor displayed notable features viz. (i) solution processibility, (ii) fast signal response/recovery time (28 s/40 s), (iii) lower limit of detection at sub-ppm levels (0.56 ppm), (iv) high selectivity over other volatile species, and (v) operational ability at room temperature under ambient conditions. A control sensing experiment was also performed using simple alkyl substituted PDI i.e. PDI-n-octyl (**Scheme 4.1b**) to confirm the effect of amino acid attached onto the imide position of PDI on sensing behavior. Finally, we have demonstrated that the variation of substituent groups at the imide position of perylene dyes remarkably affects the solid-state aggregation modes as well as redox potential that cause the significant impact on the gas responses.

4.2 Experimental

4.2.1 Materials and measurements

Perylene-3,4,9,10-tetracarboxylic dianhydride, octylamine, and zinc acetate were purchased from Sigma-Aldrich and were used as received without any further purification. Histidine and imidazole were purchased from Himedia Leading BioSciences Company and Alfa Aesar, respectively. Spectroscopic grade solvents were used for all the experiments. The ^{1}H NMR and ^{13}C NMR spectra were recorded on a Bruker Ascend 600 spectrometer. Mass spectra were obtained using a Q-TOF ESI-MS instrument (model HAB 273). Field emission scanning electron microscope (FESEM) images were recorded on a Sigma Carl ZEISS scanning electron microscope. Transmission electron microscopic (TEM) studies were done using a Tecnai G2 F20 S-twin JEOL 2100 transmission electronmicroscope. UV-VIS absorption spectra (both solution and thin film) were recorded on a Perkin Elmer Lambda 35 spectrometer. FT-IR was recorded on a Perkin Elmer spectrometer with samples prepared using KBr pellets. Electrochemical measurements were carried out on a CH instruments model 700D series consisting of a three-electrode system, viz., Ag/AgNO$_3$ as the reference electrode, platinum wire as the counter electrode, and glassy carbon as the working electrodes. Tetra-n-butyl ammonium hexafluorophosphate (TBAP) in acetonitrile solution (0.1 M) and ferrocene were used as a supporting electrolyte and internal reference respectively at a scan rate of 50 mV/s under an inert atmosphere. The thickness of the deposited films was optimized using a Dektat-150 profilometer.

4.2.2 Synthesis of PDI-HIS

PDI-HIS and PDI-n-octyl were synthesized using a modified reported procedure.[47,48]

A mixture of perylene-3,4,9,10-tetracarboxylic dianhydride (300 mg, 0.76 mmol), histidine (260 mg, 1.67 mmol), zinc acetate (catalytic amount) and 5.0 g of imidazole was heated at 140 °C for 8h under continuous stirring. The reaction mixture was then allowed to cool and poured into water. To the mixture, 2.0 M HCl was added under continuous stirring to obtain a precipitate. This was then centrifuged and washed several times with water followed by drying under vacuum to get the red colored solid product. Yield=460 mg, 90%. ^{1}H NMR (DMSO, 600 MHz, δ ppm): 9.06 (s, 2H), 8.96 (s, 2H), 8.53 (b, 4H), 8.34 (b, 4H), 5.86 (t, 2H). ^{13}C NMR (DMSO, 150 MHz, δ ppm): 169.89, 162.50, 134.32, 134.19, 133.96, 131.59, 130.03, 124.15, 119.41, 117.15, 52.82, 28.49. ESI-MS: m/z $[M+H]^+$ calculated for $C_{36}H_{22}N_6O_8$ 666.1499, found 667.1551.

4.2.3 Synthesis of PDI-n-octyl

A mixture of perylene-3,4,9,10-tetracarboxylic dianhydride (300 mg, 0.76 mmol), octyl amine (216 mg, 1.67 mmol), zinc acetate (catalytic amount) and 5.0 g of imidazole was heated at 140 °C for 8h under continuous stirring. The reaction mixture was then allowed to cool and poured into methanol. The red solid was further purified by column chromatography using hexane-chloroform as an eluent. Yield=291 mg, 62%. ^{1}H NMR ($CDCl_3$, 600 MHz, δ ppm): 8.67 (d, 4H), 8.60 (d, 4H), 4.18 (t, 4H), 1.74 (m, 4H), 1.55-1.24 (m, 20H), 0.85 (t, 6H).

4.2.4 Device fabrication and characterization

For the fabrication of a two terminal sensor device, low cost microscopic glass slides (1 cm x 2 cm) were used as substrates. The glass substrates were cleaned in piranha solution ($3:1/H_2SO_4:H_2O_2$) for 1h and washed several times with deionized water followed by sonication. The cleaned substrates were then dried under vacuum at 100 °C. A channel of 30 μm length (L) and 2000 μm width (W) was obtained by depositing 150 nm thick aluminum (Al) electrodes on to cleaned glass substrates by thermal evaporation under high vacuum $<10^{-6}$ mbar. From the stock solution of 1mM PDI-HIS in DMSO, a volume of 5 mL was drop-casted over the channel between the electrodes. The solvent was fully dried by heating on a hot plate for 30 min at 80 °C to form a thin film (thickness 60 nm) across the fabricated Al electrodes. All the electrical characterizations of the devices were carried out under ambient conditions using a Keithley 4200-SCS semiconductor parameter analyzer at room temperature.

4.2.5 Vapor phase detection

For the vapor sensing experiment, the fabricated device was kept in a chamber of approximately 0.06 L in volume. A certain volume of the analyte was injected into the test chamber by using a micropipette. The concentration of vapor was calculated using the following eqn. (1);[49]

$$C_{ppm} = \frac{V_{\mu L}\, D_{g/mL}}{M_{g/mol} V_{mL}} \times 2.24 \times 10^{7} \qquad (1)$$

where, C_{ppm} is the required vapor concentration, $V_{\mu L}$ is the volume of the liquid analyte, $D_{g/mL}$ is the density of the liquid, V_{mL} is the volume of the test chamber and $M_{g/moL}$ is the molecular weight of the liquid analyte. All the subscripts are the corresponding units. Sensing studies using various commercially available common analytes were carried out by injecting the sample in a vial placed inside the chamber adjacent to the device at room temperature and under ambient conditions.

4.3 Results and discussion

4.3.1 Synthesis and characterization of PDI-HIS and PDI-n-Octyl

PDI-HIS and PDI-n-Octyl were synthesized in high yields by using modified reported procedure (**Scheme 4.2a and 4.2b**). The synthesized monomers were characterized by NMR spectroscopy and mass spectrometry (**Figure A4.1-A4.4**).

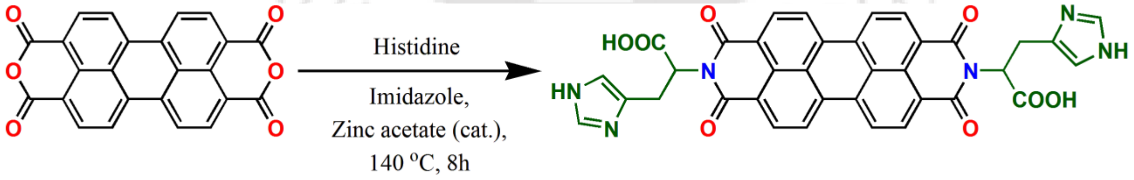

Scheme 4.2a Synthetic scheme of PDI-HIS.

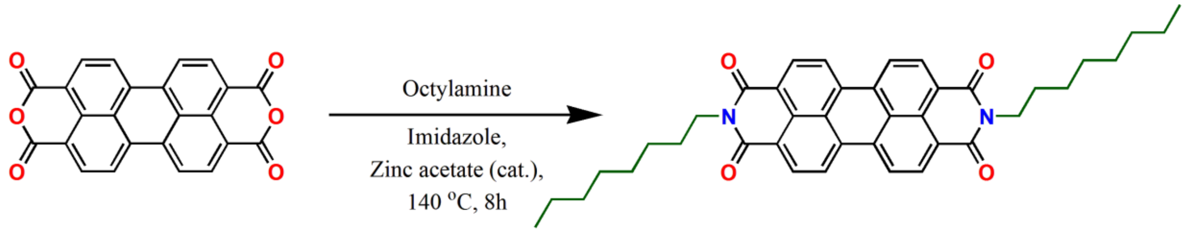

Scheme 4.2b Synthetic scheme of PDI-n-Octyl.

4.3.2 Sensing studies

Sensing experiments were carried out using both PDI-HIS and PDI-n-octyl fabricated two terminal sensor devices with simple architecture as shown in **Figure 4.1a**. The devices were kept in a chamber and connected to a Keithley 4200 SCS semiconductor parameter analyzer to perform electrical characterization. For I-V measurements, the devices were tested in a vacuum first and then under ambient conditions by sweeping the voltage from –10 V to +10 V to check their stability in the real environment. The I-V curve obtained for a PDI-HIS thin film demonstrated a good conducting behavior (**Figure 4.1b**) compared to that of PDI-n-octyl (**Figure A4.5**).

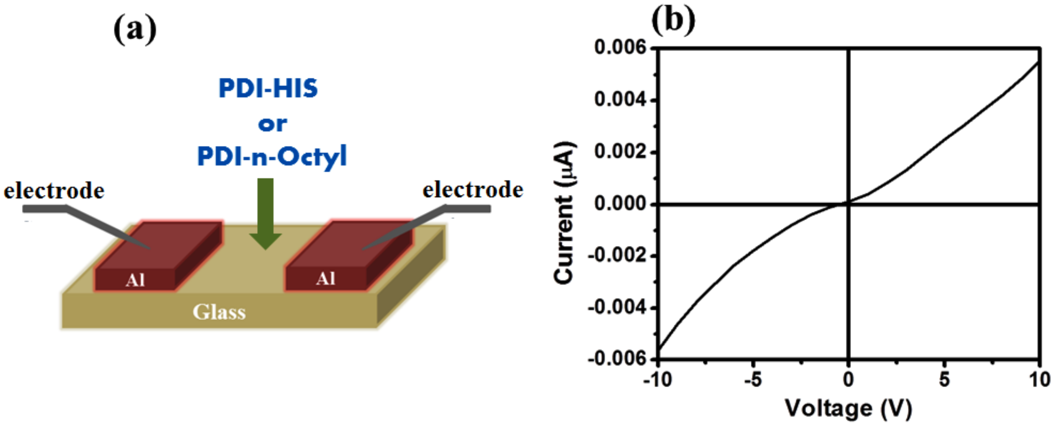

Figure 4.1 (a) Schematic diagram of the device structure and (b) I-V characteristics of the PDI-HIS thin film.

To investigate the sensing response of a PDI-HIS thin film device towards NH_3, the concentrations of NH_3 were systematically varied from 100 ppm to 2 ppm and changes in the current intensity were observed. As shown in **Figure 4.2a**, a significant increase in current was observed after exposing 100 ppm NH_3 vapors to the chamber that was seen enhancing continuously with very short response time. Upon turning off the NH_3 source, current intensity recovered quickly to its initial level. Thus, it can be concluded that the device exhibits excellent response and recovery time for the NH_3 detection. To perform the quantification by this device, the chamber was exposed to 50, 30, 20, 10, 5 and 2 ppm NH_3 vapors to obtain similar responses with lower current intensity that varied according to the concentrations. The corresponding sensitivity (S) was calculated using the formula $S=\Delta I/I_0$, where ΔI is the change in current intensity upon NH_3 vapor exposure and I_0 is the initial current in absence of NH_3 vapors. The sensitivity of the device was then plotted as a function of different NH_3 concentrations. The curve showed a linear response with increase in the concentration of NH_3 as shown in **Figure 4.2b**.

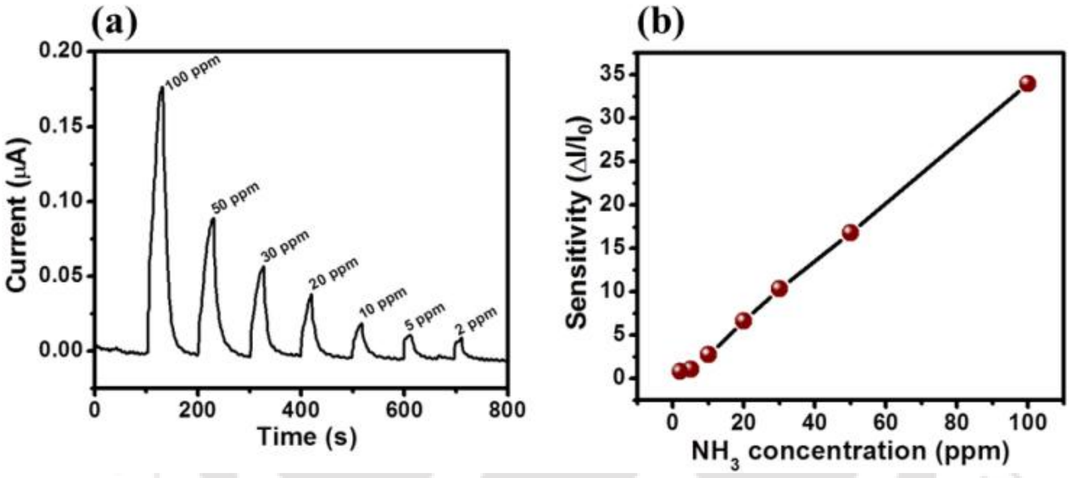

Figure 4.2 (a) Response of the PDI-HIS sensor device towards various concentrations of NH_3 vapors ranging from 100 ppm to 2 ppm and (b) sensitivity of the device as a function of NH_3 concentration.

The response and recovery times are considered as important parameters for any gas-sensing devices. The response time is the time needed for a sensing device to reach 90% of total current change after the supply of analyte vapors, whereas the recovery time is the 90% of current change to return to its original position after the analyte vapor source is turned off. The response time of the device to 100 ppm of NH_3 was calculated to be very low as 28 s, whereas the recovery time was found to be 40 s (**Figure 4.3a**). To the best of our knowledge, such low cost high stability devices have not been reported yet with such a remarkable response/recovery time for NH_3 detection and high sensitivity making the current protocol highly reliable and useful for the rapid detection of NH_3 vapors. To further verify the viability of this system for practical applications, the recyclability of the device was checked by exposing certain concentration of NH_3 vapors repeatedly after certain interval of time into the test chamber. Almost similar increment in current intensity (**Figure 4.3b**) was observed after each exposure confirming the feasibility of the sensor device for realistic use.

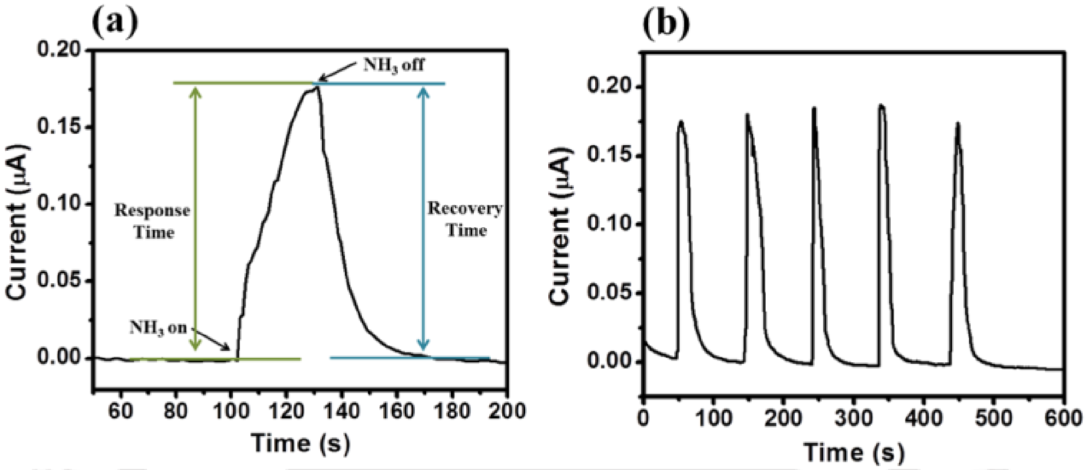

Figure 4.3 (a) Response and recovery time of NH_3 sensor device and (b) recyclability test with 100 ppm of NH_3 vapor.

The stability of the sensor device is another crucial and most vital criterion for practical applications. After leaving the device under ambient conditions for ~4 weeks, the sensor device was again tested with different NH_3 concentrations (**Figure 4.4a**). It was observed that the change in current intensity in the devices showed excellent reversibility and stability under continuous operation and storage conditions with negligible to no loss in activity even after prolonged testing or storing under ambient conditions. The limit of detection (LOD) is another vital parameter to be determined for a sensor device. To calculate the LOD, a calibration curve was constructed by plotting the maximum current intensity against the concentration of NH_3 (**Figure 4.4b**). The curve demonstrates a good linear relationship with the correlation coefficient (R^2) value of 0.9994. The limit of detection (LOD) was calculated using the formula $LOD=3\sigma/S$, where, 'σ' is the relative standard deviation of the current response of the device in the absence of NH_3 and 'S' is the slope of the calibration curve. The LOD was found to be 0.56 ppm which is compatible with the minimum permissible limit set for NH_3 in the working environment i.e. 25 ppm for long exposure upto 8h.

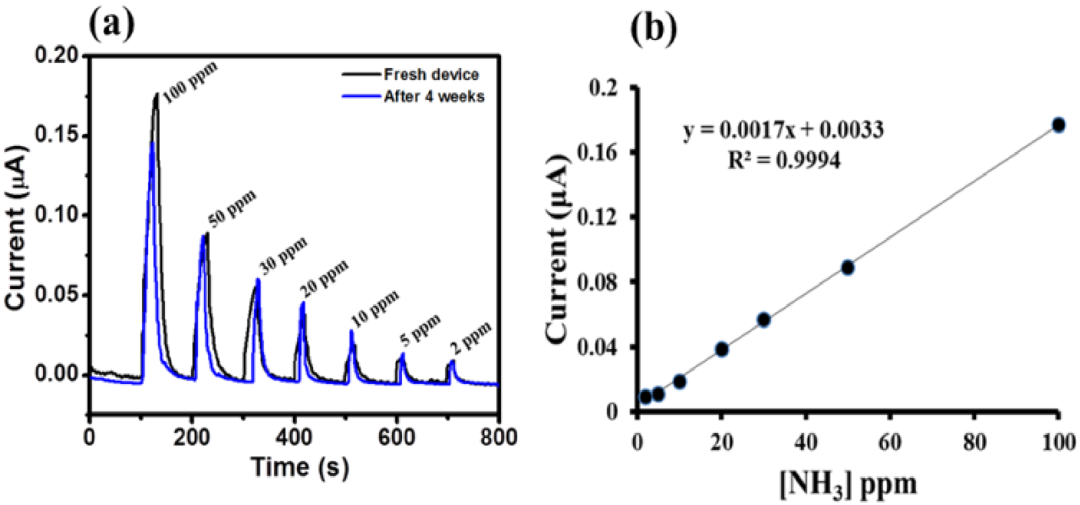

Figure 4.4 (a) Sensing response of the PDI-HIS sensor device with different concentration of NH_3 before and after 4 weeks of storage under ambient conditions and (b) calibration curve for calculating the detection limit.

4.3.2 Effect of humidity and film thickness on sensing

All the sensing experiments were carried out in the laboratory atmosphere (relative humidity RH $\geq$ 60%) that provides an environment closer to the ultimate condition of the sensor devices. To further study the effect of humidity on the NH_3 response, sensing experiments were carried out by exposing 50 ppm NH_3 on three different devices at humidity levels RH 0%, 60% and 90%, respectively (**Figure A4.6).** In a vacuum (RH 0%), the sensor device gave highest response for NH_3 and decreases by ~18% on increasing the RH upto 60%. However, on further increasing the humidity levels from 60% to 90%, the response of the device towards NH_3 decreases by only ~8%. Low sensitivity of the device at higher humidity is consistent with the weak adsorption/diffusion of NH_3 vapors on the surface of the film. It is believed that under higher humidity conditions, there is a probability of a strong competition between water and NH_3 molecules to get adsorbed/diffused at the receptor sites (histidine units) of the PDI-HIS film. Thus, it can be concluded that the sensor device is functional over a wide range of humidity levels and can be used for sensing NH_3 under real environmental conditions.

To monitor the effect of film thickness on sensitivity, three devices with variable thicknesses (30, 60 and 100 nm) were optimized and investigated for their sensing response towards 100 ppm NH_3 **(Figure 4.5 and A4.7**). It was found that the sensitivity of the devices rises by ~3.3 times on increasing the thickness from 30 nm to 60 nm with slight increment (1s/4s) in the response/recovery time. However, on further increasing the thickness from 60 nm to 100 nm, the sensitivity increases by only ~1.3 times with much larger increment (26s/16s) in response/recovery time. The high response time in a thicker film may be attributed to the diffusion of a large number of NH_3 molecules into the film which thereby takes a much longer time to get recovered. These studies helped in concluding that the thickness of a film affects the sensor response and a device with film thickness of ~60 nm is generally appropriate for NH_3 detection considering the response/recovery time and better sensitivity observed here.

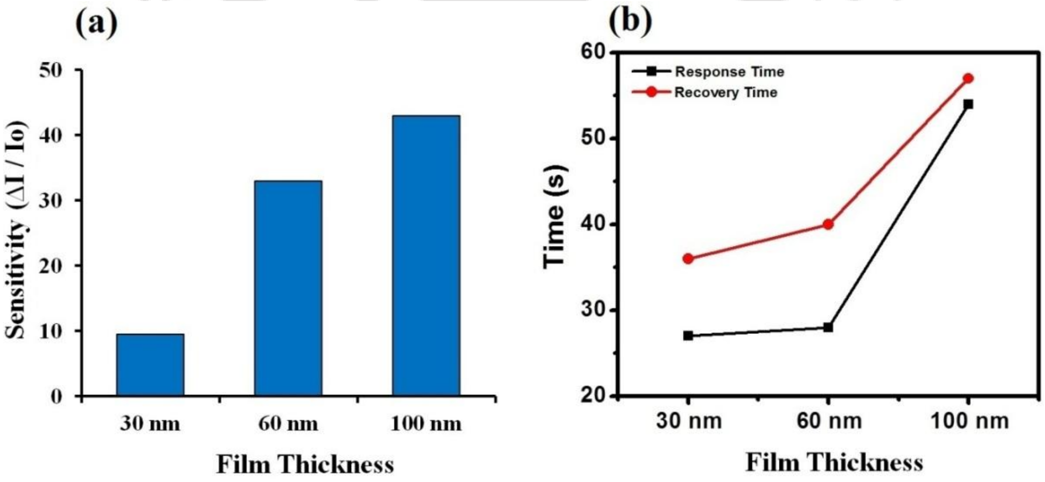

Figure 4.5 Effect of film thickness on (a) sensitivity of the device and (b) response/recovery time after exposing 100 ppm NH_3.

4.3.3 Selectivity studies

To validate the selectivity of the device, similar sensing experiments were also performed with eight common volatile organic solvents (chloroform, acetone, methanol, isopropanol, ethanol, ethyl acetate, THF and hexane) by exposing five times higher concentration than NH_3 (**Figure 4.6a**). Interestingly, the device responses to even 1000 ppm of common organic analytes were negligible in comparison to 200 ppm of NH_3. To date, such outstanding selectivity and reusability of NH_3 sensors with remarkably low detection limits has marked this sensor device as a rare example available in literature. To further explore the selectivity of this system, the device was also exposed to various other common organic amines such as cyclohexyl amine, triethyl amine, diisopropyl amine, pyridine and diethyl amine, since all these vapors have biological or environmental consequences. From **Figure 4.6b**, it can be concluded safely that the response of a sensor device towards various other amines was insignificant compared to NH_3 even at much higher concentrations.

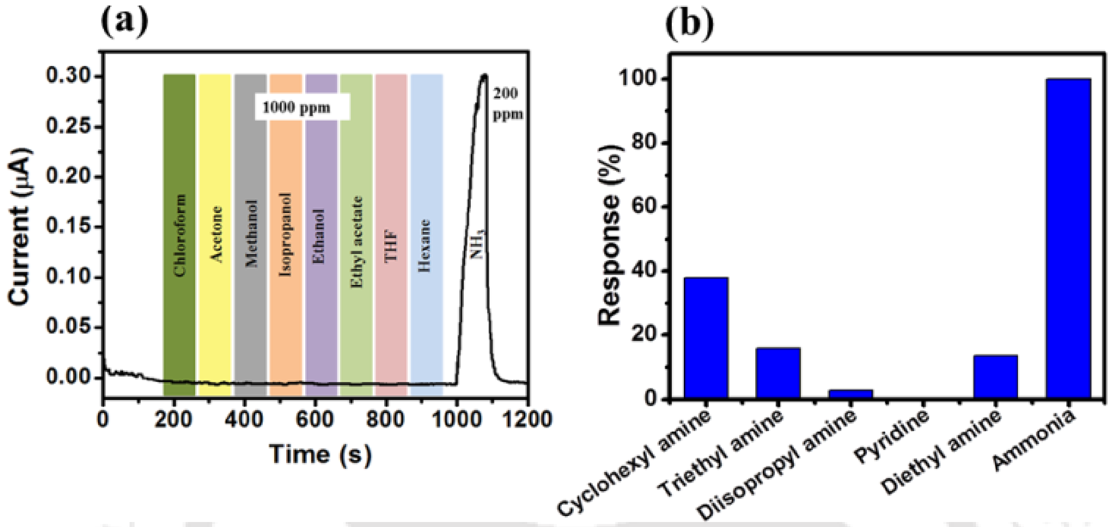

Figure 4.6 Sensing response of the PDI-HIS sensor device with vapors of various common (a) organic solvents and (b) amines. Concentrations of NH_3 and other analytes were 200 and 1000 ppm, respectively.

4.3.4 Sensing mechanism

Generally, the mechanism of organic semiconductor based conductometric gas sensors involves the adsorption of analytes onto the surface via dissociation and/or diffusion followed by the formation of a possible charge transfer complex that eventually leads to the variation of majority charge carriers than in the current.[45,50] Depending upon the chemical nature of both the species, the binding can be weak or strong via some chemical interactions such as hydrogen bonding, dipole-dipole interactions etc. The molecular self-assembly due to π-π interactions in such semiconductors also provides efficient pathways for charge migration or transport. Change in redox potential is another major factor associated with the mobility of charge carriers.[1,30,32,42,51,52]

To understand the sensing mechanism, the surface morphology of the PDI-HIS fabricated film was initially studied before and after exposure to NH_3 vapors via FESEM and TEM, respectively. The PDI-HIS film showed an amorphous self-assembled nanostructured network throughout the surface (**Figure 4.7a and 4.7c**) which indicates the huge surface area available for the adsorption and/or diffusion of gas molecules (**Figure 4.7b and 4.7d**) that subsequently leads to the remarkable change in the current and response time. On introducing NH_3 vapors onto the PDI-HIS fabricated film, the current intensity displayed significant increment by several orders of magnitude with an excellent response time. This can be explained by donor-acceptor like complexation[53] between n-type organic semiconductor materials i.e. PDI-HIS (electron acceptor) and NH_3 (electron donor) molecules. Since, each PDI-HIS molecule consists of two –COOH units at the imide positions that have the tendency to bind with NH_3 through an acid-base interaction, numerous ion pairs are expected to form in the film that can drastically increase the ionic conductivity and consequently the current. In addition, the presence of histidine groups will further boost up the sensitivity of the device due to the favorable hydrogen bonding interactions with NH_3. The aggregation of PDI-HIS molecules due to π-π interactions is another possible factor responsible for such a high sensitivity, since it can provide efficient charge transport into the material.

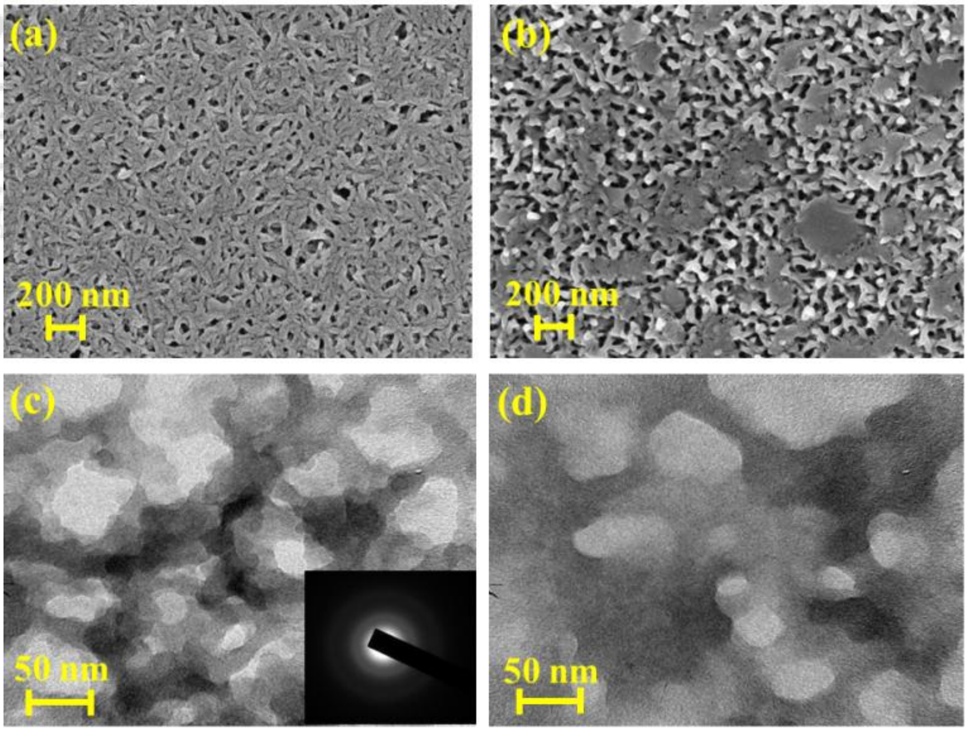

Figure 4.7 FESEM and TEM images of PDI-HIS thin film (a), (c) before and (b), (d) after exposure of NH_3 vapors. (Inset: SAED pattern of PDI-HIS)

Furthermore, to validate the proposed sensing mechanism, we have monitored the changes in the IR spectrum of PDI-HIS before and after exposing it to NH_3 vapors (**Figure A4.8**). The band observed at 3418 cm^{-1}corresponds to the stretching vibrations of carboxylic –OH and/or histidine –NH, which showed a significant shift (3347 cm^{-1}) immediately after exposing it to NH_3 vapors confirming the adsorption/diffusion of NH_3 vapors onto the surface of the film via hydrogen bonding interactions/acid-base interactions that subsequently leads to the increment in ionic conductivity and current.

In order to elucidate the effect of the amino acid anchoring groups on PDI-HIS, sensing studies were also performed using a fabricated device of a model compound PDI-n-octyl that does not consists of any active groups (e.g. COOH) at the imide position except long alkyl chains. Interestingly, no significant enhancement in the current (0.20 times) was observed after introducing NH_3 vapors to the PDI-n-octyl fabricated film even at much higher concentrations (**Figure A4.9**). These results confirm that the solubilizing/anchoring group attached onto the imide position of PDI-HIS played a vital role in the signaling process. The active –COOH groups on either side of PDI-HIS are responsible for the ultra-sensitivity, since they may possibly increase the number of H^+ ions which in turn enhance the mobility of protons in the molecule and ultimately the current.

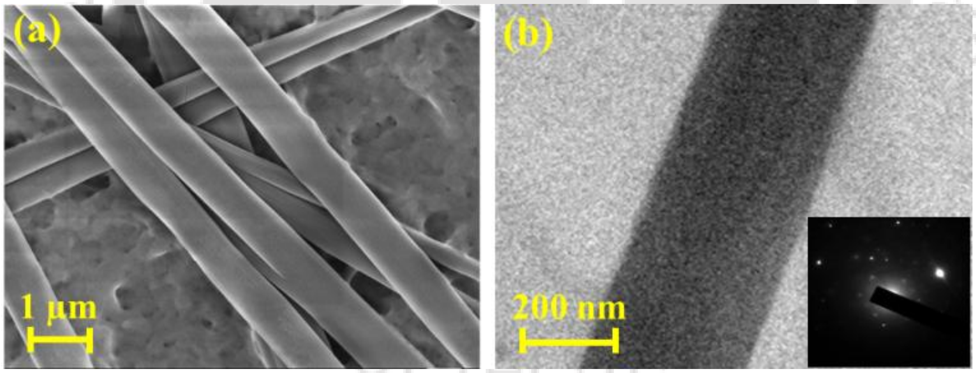

Figure 4.8 (a) FESEM and (b) TEM image of PDI-n-octyl. Inset: SAED pattern of PDI-n-octyl.

The morphology of the PDI-n-octyl film was studied via FESEM and TEM analysis (**Figure 4.8**) which confirms that PDI-n-octyl molecules exhibit single-crystalline belt like microstructures unlike amorphous aggregates as observed in the PDI-HIS film. The single-crystalline micro/nanostructures provide highly efficient channels for charge carrier transport due to the large surface area for diffusion of gas molecules.[30]

However, the PDI-HIS molecule showed a marvellous response towards NH_3 compared to the PDI-n-octyl molecule even though it is amorphous in nature. This indicates that there is a possibility of some additional factors that are also involved in the sensing mechanism. Thus, to gain further insight into the mechanism and differential response of the NH_3 vapors towards PDI-HIS and PDI-n-octyl fabricated devices, electronic parameters of both the semiconductors were studied via cyclic voltammetry (CV) measurements (**Figure 4.9**).

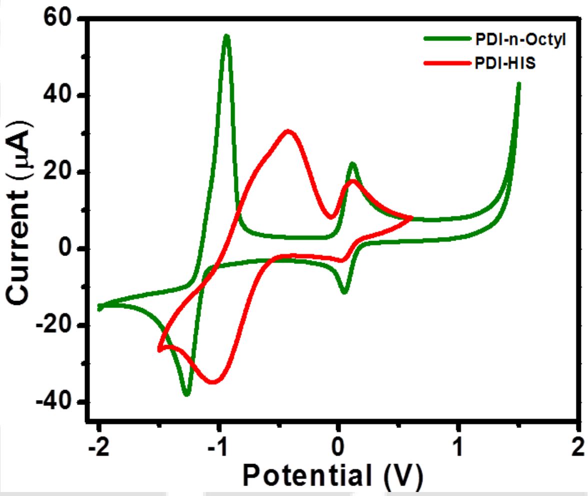

Figure 4.9 Cyclic voltammograms of PDI-HIS and PDI-n-octyl films on a glassy carbon electrode in CH_3CN.

The values of reduction potential, HOMO/LUMO energies and the estimated band gap are summarized in **Table 1**. The LUMO energy level obtained for PDI-HIS (–4.07 eV) was

Table 1. Frontier molecular orbital energies as estimated from cyclic voltammetry and optical absorption.

Organic semiconductors	E_{red}^{onset}	LUMO (eV)	HOMO (eV)	λ_{abs}^{onset} (nm)	E_g (eV)
PDI-HIS	−0.65	−4.07	−6.32	549	2.25
PDI-n-Octyl	−1.12	−3.60	−5.89	542	2.29

significantly lower compared to PDI-n-octyl (–3.60 eV) that makes it more capable for the occurrence of charge transfer[30] between the PDI-HIS and NH_3 molecules that ultimately leads to the dramatic increment in current (~33 times). Thus, it can be concluded that the presence of active receptors (histidine units) in PDI-HIS is one of the key factors for increasing the sensitivity of the device via lowering the LUMO energies that enabled the efficient charge exchange between PDI-HIS and NH_3 molecules, making the sensor device highly sensitive towards NH_3.

4.3.5 Comparative study

To demonstrate the advantage of present sensing platform over the previously reported works, various parameters of the PDI-HIS sensor device towards NH_3 vapors are compared with recent literature (**Table 2**).

Table 2. A comparative study of PDI-HIS sensor with different reported materials.

Sensing material used	Response/ Recovery Time	LOD	Ref.
Perylene diimide thin film	***28s/40s***	***0.56 ppm***	***Present work***
WO_3-SnO_2 nanostructures	N/A	520 ppb	3
Dialkyl tetrathiapentacene derivative	36s/10s	10 ppm	2
Naphthalene diimide derivative	5s/2s	10 ppm	29
Pentacene thin film	N/A	0.5 ppm	30
Monolayer pentacene thin film	N/A	10 ppm	28
Fe_3O_4/MWCNT PhCOOH hybrid	200s/>200s	250 ppm	14
Polymer PGMA-AN and PGMA-S	N/A	13.9 ppm & 16 ppm	48
ZnO nanostructures	20s/25s	25 ppm	15
Graphene network	N/A	20 ppm	24

SnO_2 nanoparticle	75s/67s	50 ppm	16

It is noteworthy that the sensing performance of the PDI-HIS thin film is not only superior to other materials such as polymers, metal oxides, graphenes, CNT etc. but also the best and the most economical platform among various other small molecule based sensors towards NH_3.

4.4 Conclusion

In conclusion, a new and efficient platform for the vapor phase detection of NH_3 using a two terminal sensor device based on PDI-HIS nanostructures fabricated on a simple glass substrate by the drop-casting method has been developed. The sensing parameters viz. sensitivity, selectivity, recyclability, response/ recovery time and stability were studied that revealed the excellent performance of the device with a very low detection limit of 0.56 ppm for NH_3. We have also demonstrated that the molecular assemblies of PDI-HIS nanostructures, redox potential and ionic groups at the imide position are key aspects for the remarkable response of the device towards NH_3. Thus, the ability of the as-fabricated sensor device to detect NH_3 vapors at room temperature and under ambient conditions with high sensitivity, selectivity and low fabrication cost makes the protocol economical and feasible for potential applications under chemical, biomedical and competitive environmental conditions.

4.5 References

(1) Meng, Q.; Zhang, F.; Zang, Y.; Huang, D.; Zou, Y.; Liu, J.; Zhao, G.; Wang, Z.; Ji, D.; Di, C.; Hu, W.; Zhu, D. *J. Mater. Chem. C* **2014**, *2*, 1264.

(2) Li, L.; Gao, P.; Baumgarten, M.; Müllen, K.; Lu, N.; Fuchs, H.; Chi, L. *Adv. Mater.*, **2013**, *25*, 3419.

(3) Nayak, A. K.; Ghosh, R.; Santra, S.; Guha, P. K.; Pradhan, D. *Nanoscale* **2015**, *7*, 12460.

(4) Appl, M. Ammonia: Principles and Industrial Practice, Wiley-VCH, New York, USA, **1999**.

(5) Pandey, S.; Goswami, G. K.; Nanda, K. K. *Sci Rep.*, **2013**, *3*, 2082.

(6) Cannilla, C.; Bonura, G.; Frusteri, F.; Spadaro, D.; Trocinoc, S.; Neri, G. *J. Mater. Chem. C* **2014**, *2*, 5778.

(7) Budarvari, S. The Merck Index, An Encyclopedia of Chemicals, Drugs and Biologicals, O'Neil, J. M. Ed.; Royal Society of Chemistry: Cambridge, 12th ed., **1996**.

(8) Wang, J.; Yang, P.; Wei, X. *ACS Appl. Mater. Interfaces* **2015**, *7*, 3816.

(9) Timmer, B.; Olthuis, W. Berg, A. *Sens. Actuators B* **2005**, *107*, 666.

(10) Grady, T.; Butler, T.; MacCraith, B. D.; Diamond, D.; McKervey, M. A. *Analyst* **1997**, *122*, 803.

(11) Kumar, N.; Srivastava, A. K.; Nath, R.; Gupta, B. K.; Varma, G. D. *Dalton Trans.*, **2014**, *43*, 5713.

(12) Kannan, P. K.; Saraswathi, R. *J. Mater. Chem. A* **2014**, *2*, 394.

(13) Wang, J.; Yang, F.; Wei, X.; Zhang, Y.; Wei, L.; Zhang, J.; Tang, Q.; Guo, B.; Xua, L. *Phys. Chem. Chem. Phys.*, **2014**, *16*, 16711.

(14) Pistone, A.; Piperno, A.; Iannazzo, D.; Donato, N.; Latino, M.; Spadaro, D.; Neri, G. *Sens. Actuators, B* **2013**, *186*, 333.

(15) Mani, G. K.; Rayappan, J. B. B. *Sens. Actuators, B* **2013**, *183*, 459.

(16) Liu, X.; Chen, N.; Han, B.; Xiao, X.; Chen, G.; Djerdjc, I.; Wang, Y. *Nanoscale* **2015**, *7*, 14872.

(17) Strömberg, N.; Hakonen, A. *Anal. Chim. Acta* **2011**, *704*, 139.

(18) Chartuprayoon, N.; Hangarter, C. M.; Rheem, Y.; Jung, H.; Myung, N. V. *J. Phys. Chem. C* **2010**, *114*, 11103.

(19) Danesh, E.; Lopez, F. M.; Camara, M.; Bontempi, A.; Quintero, A. V.; Teyssieux, D.; Thiery, L.; Briand, D.; Rooij, N. F.; Persaud, K. C. *Anal. Chem.*, **2014**, *86*, 8951.

(20) Stamenov, P.; Madathil, R.; Coey, J. M. D. *Sens. Actuators, B* **2012**, *161*, 989.

(21) Chen, S.; Sun, G. *ACS Appl. Mater. Interfaces* **2013**, *5*, 6473.

(22) Kang, S.; Chun, J.; Park, N.; Lee, S. M.; Kim, H. J.; Son, S. U. *Chem. Commun.*, **2015**, *51*, 11814.

(23) Kong, J.; Franklin, N. R.; Zhou, C.; Chapline, M. G.; Peng, S.; Cho, K.; Dai, H. *Science* **2000**, *287*, 622.

(24) Cui, S.; Pu, H.; Lu, G.; Wen, Z.; Mattson, E. C.; Hirschmugl, C.; Josifovska, M. G.; Weinert, M.; Chen, J. *ACS Appl. Mater. Interfaces* **2012**, *4*, 4898.

(25) Feng, X.; Irle, S.; Witek, H.; Morokuma, K.; Vidic, R.; Borguet, E. *J. Am. Chem. Soc.*, **2005**, *127*, 10533.

(26) Ghosh, R.; Singh, A.; Santra, S.; Ray, S. K.; Chandra, A.; Guha, P. K. *Sens. Actuators, B*, **2014**, *205*, 67.

(27) Seredych, M.; Teresa, J.; Bandosz, T. J. *Langmuir* **2010**, *26*, 5491.

(28) Ghosh, R.; Midya, A.; Santra, S.; Ray, S. K.; Guha, P. K. *ACS Appl. Mater. Interfaces* **2013**, *5*, 7599.

(29) Yavari, F.; Chen, Z.; Thomas, A. V.; Ren, W.; Cheng, H. M.; Koratkar, N. *Sci. Rep.*, **2011**, *1*, 166.

(30) Huang, Y.; Fu, L.; Zou, W.; Zhang, F.; Wei, Z. *J. Phys. Chem. C* **2011**, *115*, 10399.

(31) Yu, X.; Zhou, N.; Han, S.; Lin, H.; Buchholz, D. B.; Yu, J.; Chang, R. P. H.; Marks, T. J.; Facchetti, A. *J. Mater. Chem. C* **2013**, *1*, 6532.

(32) Huang, W., Besar, K.; LeCover, R.; Rule, A. M.; Breysse, P. N.; Katz, H. E. *J. Am. Chem. Soc.*, **2012**, *134*, 14650.

(33) Mirza, M.; Wang, J.; Li, D.; Arabi, S. A.; Jiang, C. *ACS Appl. Mater. Interfaces* **2014**, *6*, 5679.

(34) Zhang, F.; Di, C.; Berdunov, N.; Hu, Y.; Gao, X.; Meng, Q.; Sirringhaus, H.; Zhu, D. *Adv. Mater.*, **2013**, *25*, 1401.

(35) Zan, H. W.; Dai, M. Z.; Hsu, T. Y.; Lin, H. C.; Meng, H. F.; Yang, Y. S. *IEEE Sens. J.*, **2012**, *12*, 594.

(36) Zhang, J.; Wang, S.; Xu, M.; Wang, Y.; Xia, H.; Zhang, S.; Guo, X. Wu, S. *J. Phys. Chem. C* **2009**, *113*, 1662.

(37) Jones, B. A.; Facchetti, A.; Wasielewski, M. R.; Marks, T. J. *Adv. Funct. Mater.*, **2008,** *18*, 1329.

(38) Kozma, E.; Catellani, M. *Dyes Pigm.*, **2013**, *98*, 160.

(39) Hu, J. C.; Kuang, W. F.; Deng, K.; Zou, W. J.; Huang, Y. W.; Wei, Z. X.; Faul, C. F. J. *Adv. Funct. Mater.*, **2012**, *22*, 4149.

(40) Zang, L.; Che, Y.; Moore, J. S. *Acc. Chem. Res.*, **2008**, *41*, 1596.

(41) Huang, Y.; Yan, Y.; Smarsly, B. M.; Wei, Z.; Faul, C. F. J. *J. Mater. Chem.*, **2009**, *19*, 2356.

(42) Huang, Y.; Fu, L.; Zou, W.; Zhang, F. *New J. Chem.*, **2012**, *36*, 1080.

(43) Balakrishnan, K.; Datar, A.; Naddo, T.; Huang, J.; Oitker, R.; Yen, M.; Zhao, J.; Zang, L. *J. Am. Chem. Soc.*, **2006**, *128*, 7390.

(44) Sun, Y.; Li, Z.; Wang, Z. *J. Mater. Chem.*, **2012**, *22*, 4312.

(45) Huang, Y.; Zhang, W.; Wang, J.; Wei, Z. *ACS Appl. Mater. Interfaces*, **2014**, *6*, 9307.

(46) Huang, Y.; Zhang, W.; Wang, J.; Fu, L.; Shi, J. *Mater. Chem. Phys.*, **2015**, *151*, 93.

(47) Muthuraj, B.; Chowdhury, S. R.; Mukherjee, S.; Patra, C. R.; Iyer, P. K. *RSC Adv.*, **2015**, *5*, 28211.

(48) Singh, T. B.; Erten, B.; Gunes, S.; Zafer, C.; Turkmen, G.; Kuban, B.; Teoman, Y.; Sariciftci, N. S.; Icli, S. *Org. Electron.*, **2006**, *7*, 480.

(49) Kaneti, Y. V.; Zhang, Z.; Yue, J.; Zakaria, Q. M. D.; Chen, C.; Jiang, X.; Yu, A.; *Phys. Chem. Chem. Phys.*, **2014**, *16*, 11471.

(50) Dai, M. Z. Lin, Y. L.; Lin, H. C.; Zan, H. W.; Chang, K. T.; Meng, H. F.; Liao, J. W.; Tsai, M. J.; Cheng, H. *Anal. Chem.*, **2013**, *85*, 3110.

(51) Li, C.; Zhai, H.; Liu, X.; Zhang, W.; Huang, Y. *J. Mater. Chem. C* **2015**, *3*, 2778.

(52) Huang, Y.; Zhang, W.; Zhai, H.; Li, C. *J. Mater. Chem. C* **2015**, *3*, 466.

(53) Dutta, P.; Kalita, B.; Gogoi, B.; Sarma, N. S. *J. Phys. Chem. C* **2015**, *119*, 17260.

(54) Kalita, A.; Subbarao, N. V. V.; Iyer, P. K. *J. Phys. Chem. C* **2015**, *119*, 12772.

4.6 Appendix

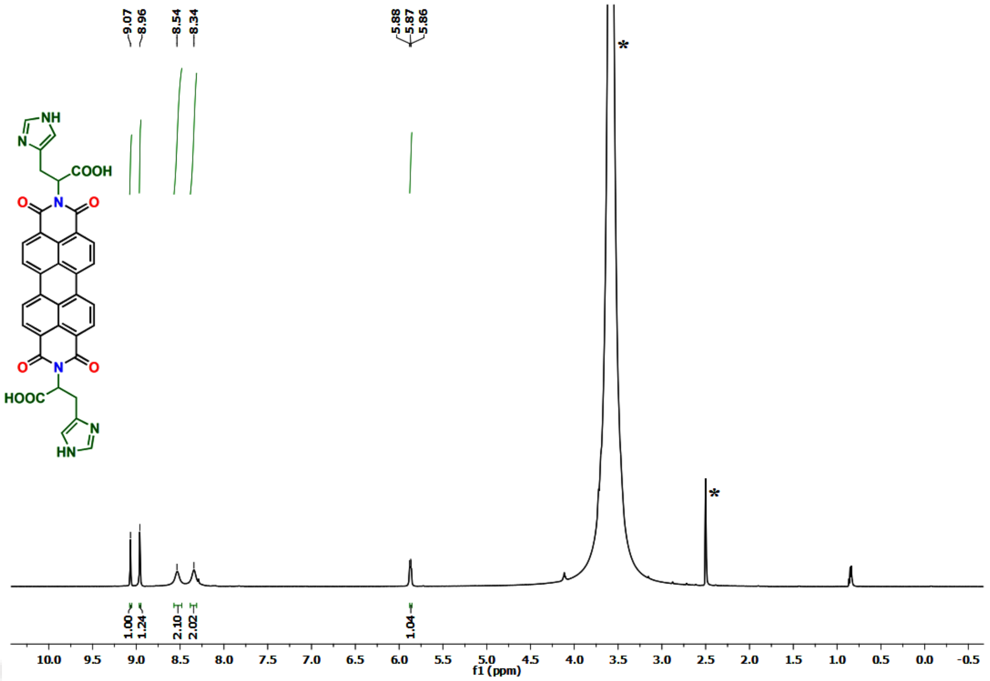

Figure A4.1 ^{1}H NMR (600 MHz, DMSO-d_6) spectra of PDI-HIS.

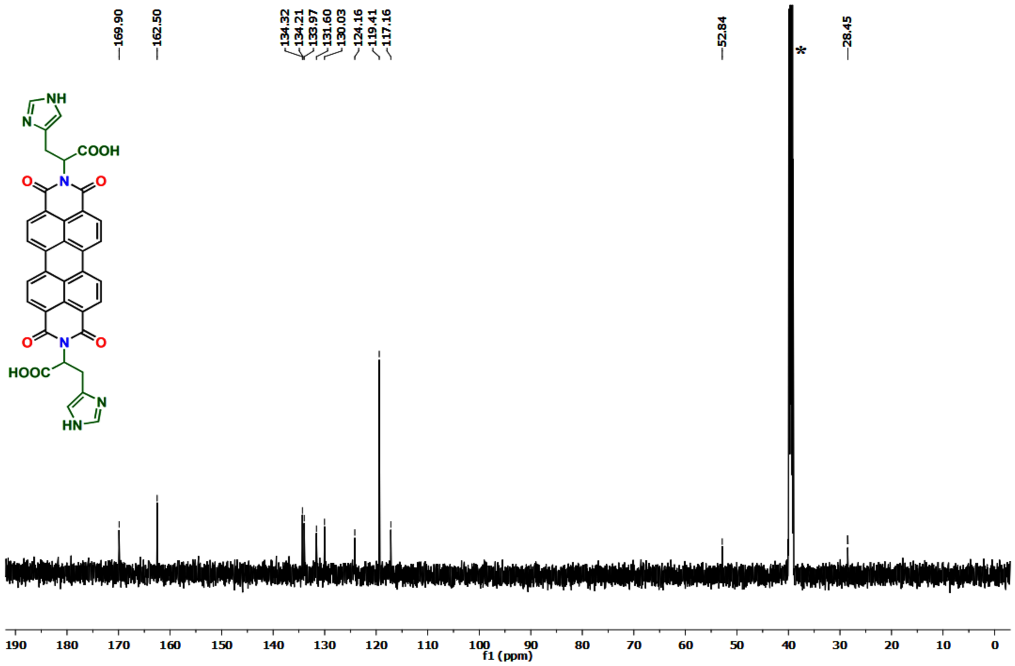

Figure A4.2 ^{13}C NMR (150 MHz, DMSO-d_6) spectra of PDI-HIS.

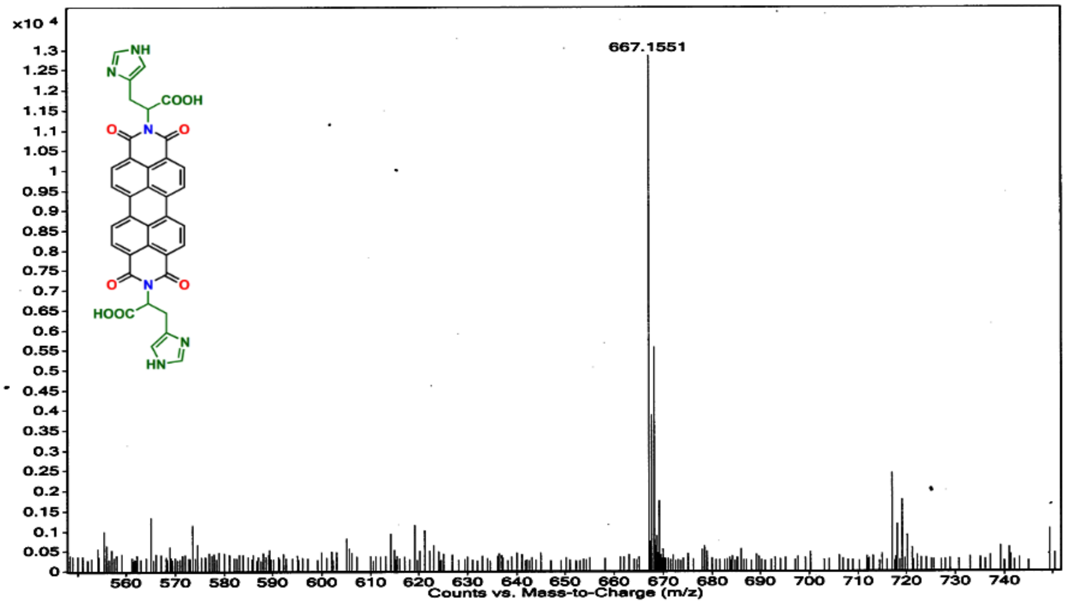

Figure A4.3 ESI-MS spectra of PDI-HIS.

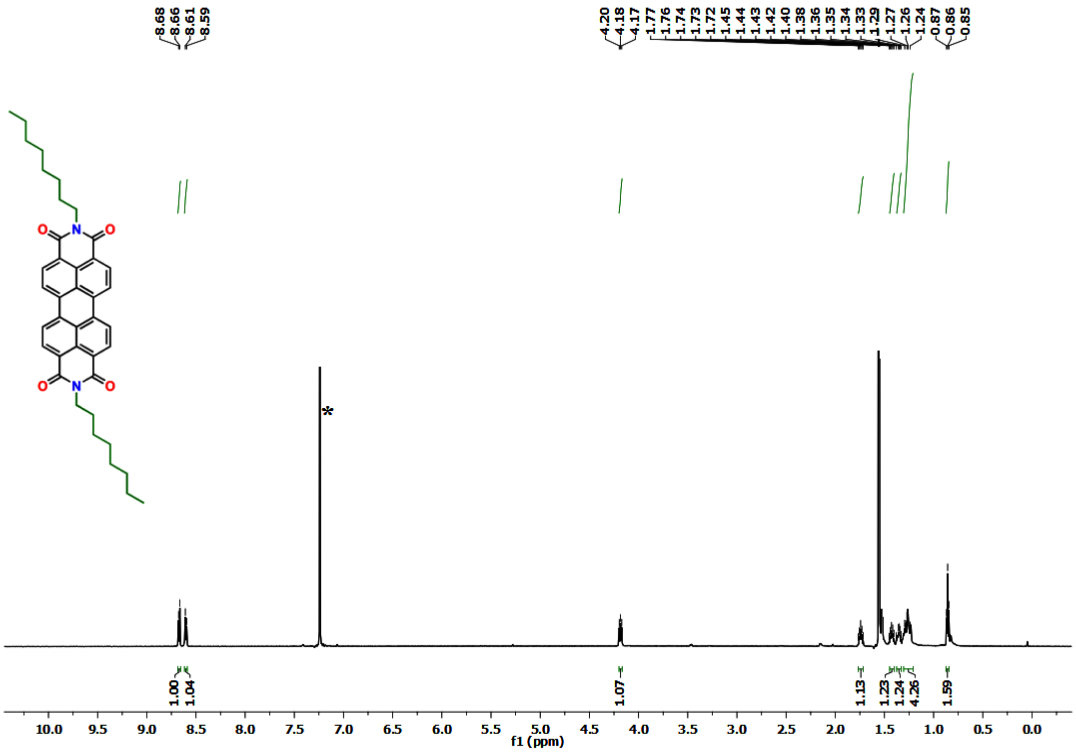

Figure A4.4 ^{1}H NMR (600 MHz, $CDCl_3$) spectra of PDI-n-Octyl .

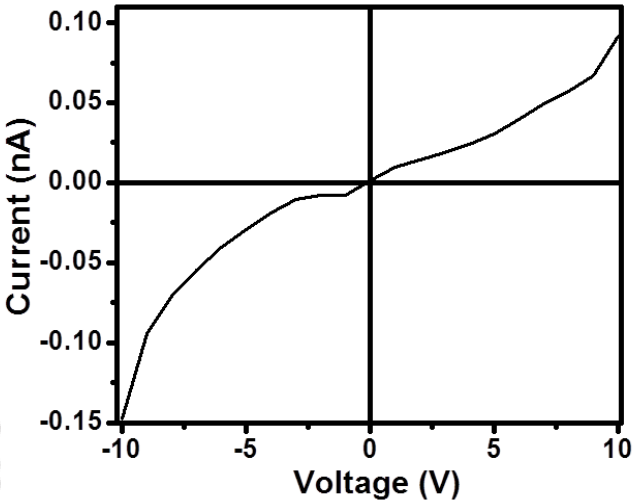

Figure A4.5 I-V characteristic of PDI-n-Octyl.

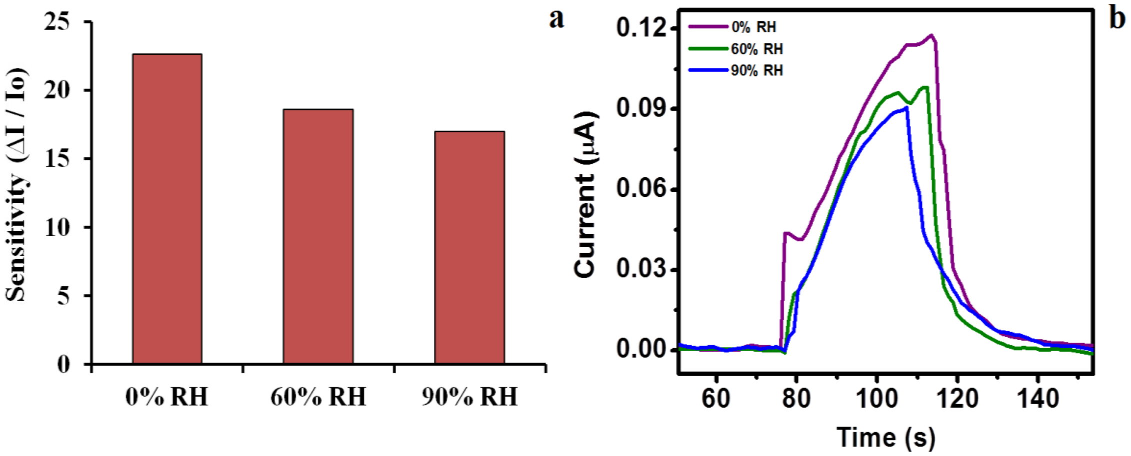

Figure A4.6 Current response with 0%, 60% and 90% relative humidity(RH) level.

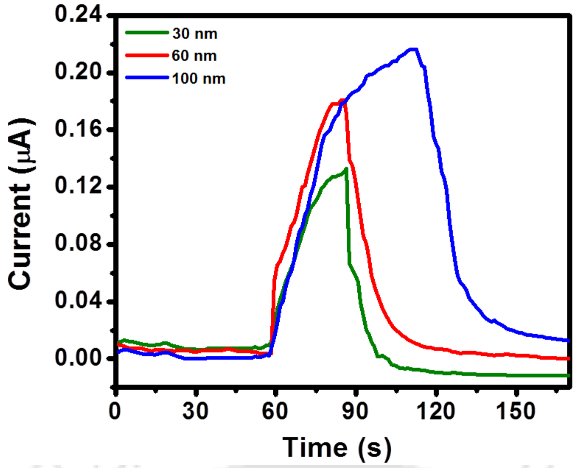

Figure A4.7 Current response observed after exposing 100 ppm NH_3 in three different devices with film thicknessess of 30, 60 and 100 nm, respectively.

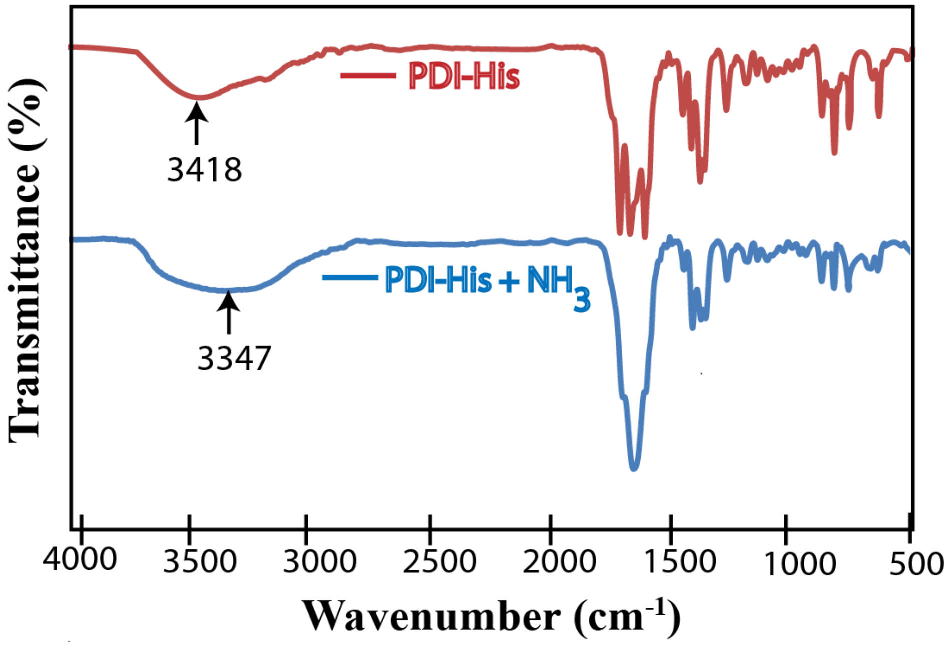

Figure A4.8 FT-IR spectra of PDI-HIS before and after exposure of NH_3 vapors.

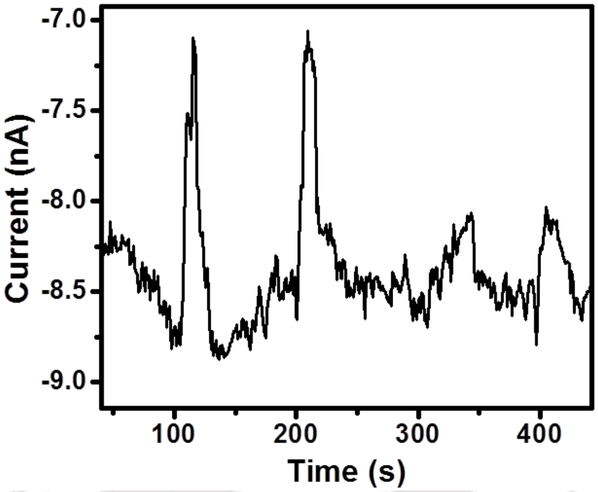

Figure A4.9 Sensing study of PDI-n-Octyl with 1000 ppm of NH_3.

Chapter 5

Anion-Exchange Induced Strong π-π Interactions in Single Crystalline Naphthalene Diimide for Nitroexplosive Sensing: An Electronic Prototype for Visual On-Site Detection

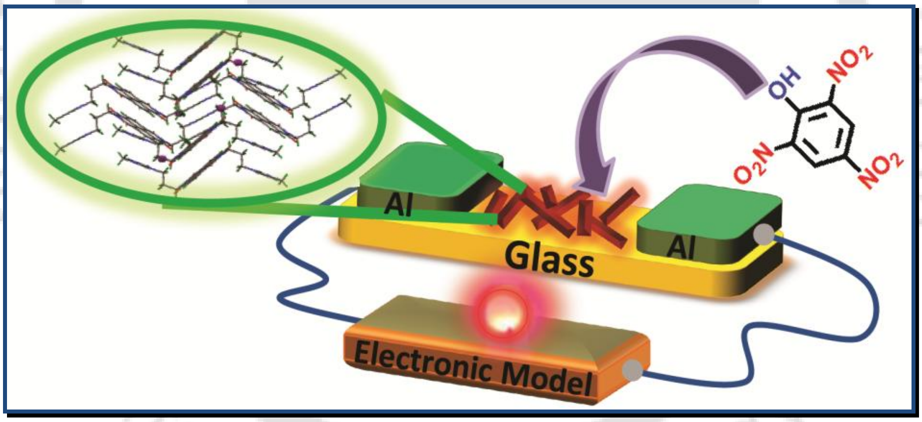

ACS Appl. Mater. Interfaces **2016**, *8*, 25326-25336.

Abstract

A new derivative of naphthalene diimide, N,N′-bis(3-imidazolium-1-ylpropyl)-naphthalenediimide diiodide (NDMI) was synthesized that displayed optical, electrical, and visual changes exclusively for the most widespread nitroexplosive and highly water soluble toxicant picric acid (PA) due to strong π-π interactions, dipole charge interaction, and a favorable electron transfer process facilitated by Coulombic attraction. The sensing mechanism and interaction between NDMI with PA is demonstrated via X-ray diffraction analysis, ^{1}H NMR studies, cyclic voltammetry and fluorescence spectroscopy. Single crystal X-ray structure of NDMI revealed the formation of self-assembled crystalline network assisted by non-covalent C−H····I interactions that get disrupted upon introducing PA as a result of anion exchange and strong π-π stacking between NDMI and PA. Morphological studies of NDMI displayed large numbers of single crystalline microrods along with some three-dimensional (3D) daisy-like structures which were fabricated on Al-coated glass substrate to construct a low-cost two terminal sensor device for realizing vapor mode detection of PA at room temperature and under ambient conditions. Furthermore, an economical and portable electronic prototype was developed for visual and on-site detection of PA vapors under exceptionally realistic conditions.

5.1 Introduction

Trinitrophenol/picric acid (TNP/PA), being a powerful explosive (stronger than TNT) and a highly water-soluble pollutant, has recently received considerable importance in the field of sensors pertaining to national security, homeland safety, and human health.[1-7] Existing PA detection systems rely on a wide range of instrument techniques,[8-12] like surface-enhanced Raman spectroscopy (SERS), gas chromatography-mass spectrometry (GC-MS), ion mobility spectrometry (IMS), X-ray diffraction, nuclear quadrupole resonance (NQR), cyclic voltammetry, etc., that are expensive and impractical for real time use. A wide variety of fluorescent probes based on organic conjugated polymers,[13-18] metal-organic frameworks (MOFs),[19-22] macrocycles/cages,[23-25] luminescent gels,[26] organic-inorganic hybrid materials,[27-32] dendrimers,[33] nanoparticles/dots,[34-37] etc., have also been reported primarily for the aqueous and/or solid phase detection of PA. However, most of these sensors are viable in organic solvents and incapable of detecting PA in complete aqueous media. Moreover, vapor mode detection of PA is highly challenging due to its extremely low vapor pressure (7.4×10^{-7} mm Hg) at room temperature. Another major drawback with most of the existing systems is the issue of selectivity due to the absence of appropriate receptors for PA. Thus, the development of a simple, rapid and cost-effective method or a convenient prototype for monitoring PA in aqueous as well as vapor mode with high selectivity is desirable to prevent growing terrorist threats as well as environmental protection due to its toxic nature.

Electronic devices fabricated on low cost substrates have recently attracted enormous attention owing to their multiple applications in the field of portable electronics.[38] The detection of analytes in such devices is based on the variation in electrical behavior of organic semiconductors through partial charge transfer or doping effect while the specificity for particular analyte can be achieved by incorporating suitable receptor sites.[39,40] In this context, some work has been done on the development of devices for monitoring traces of wide range of explosives.[41-45] However, developing an effective and portable organic semiconductor device to monitor PA vapors with high selectively and remarkable sensitivity remains intricate. This motivated us to develop an advanced portable sensing system capable of performing instant on-site detection of PA over a broad range of nitroexplosives. Among various small organic semiconductor materials, naphthalene diimide derivatives (NDIs) are exhaustively studied in the field of organic electronics owing to their excellent conducting properties.[46-49] Due to the presence of π- conjugated aromatic rings, they can also be utilized as efficient fluorescent probes for monitoring desirable species after modifications in either the core position (so-called bay position) or imide position with appropriate receptors.[50] Unlike other organic materials viz. metal-organic frameworks (MOFs), polymers, etc., NDIs are easier to synthesize and purify and are readily soluble in common organic solvents. Such characteristic features of NDIs make them ideal candidates for the development of sensitive probes utilizing both their fluorometric and conducting properties. Despite these multiple features, no attempts in designing NDI probes for the highly sensitive and selective detection of nitroexplosives especially PA either in aqueous or vapor mode has ever been reported, thereby providing enormous prospects to be explored. Cationic imidazolium groups were incorporated onto the imide position of NDI that facilitates the fluorometric detection of PA in 100% aqueous media via anion exchange and also promotes conductometric/visual detection via microrods fabricated two terminal sensor device/electronic prototype. To the best of our knowledge, this is the first practical protocol for the dual mode and on-site detection of nitroexplosive PA via strong π-π interactions, anion exchange, coulombic attraction and dipole charge interaction using self-assembled single crystalline naphthalene diimide probe.

Herein, we report the synthesis and characterization of an imidazolium appended naphthalene diimide (NDMI) for the dual mode detection of nitroexplosive PA in aqueous medium as well as vapor phase. NDMI displayed significant fluorescence quenching exclusively with PA in complete aqueous media as a result of anion exchange and strong π-π interactions, obtained for the first time between NDMI core and PA as evident via X-ray diffraction pattern and ^{1}H NMR studies of the NDMI-PA complex. Cyclic voltammetry indicates that electron transfer is another possible mechanism involved in the quenching process that subsequently enhanced the sensitivity of the probe. Morphological studies revealed that NDMI molecules exhibit three-dimensional (3D) daisy-like structures on a substrate due to the self-assembly of numerous single crystalline microrods formed as a result of favorable noncovalent C−H····I interactions. Vapor mode detection of PA at room temperature under ambient conditions was achieved using these NDMI microrods fabricated low-cost two terminal sensor devices that displayed drastic increment in its current intensity on exposure with PA vapors as a result of additional channel charge carriers at the interface. Finally, a simple, portable and cost-effective electronic device with a digital output (LED) for the safe, visual, and on-site detection of PA vapors was developed for the first time using NDMI.

5.2 Experimental

Caution! Nitroexplosives viz. TNT, RDX, and PA are highly explosive and should be handled sensibly in small amounts to prevent any explosion.

5.2.1 Materials and measurements

1,4,5,8-Naphthalenetetracarboxylic dianhydride, 1-(3-aminopropyl)imidazole, and nitroexplosives, viz. 2,4-dinitrophenol (2,4-DNP), 4-nitrophenol (4-NP), 2,6-dinitrotoluene (2,6-DNT), 2,4-dinitrotoluene (2,4-DNT), 4-nitrotoluene (4-NT), 2-nitrotoluene (2-NT), 1,3-dinitrobenzene (1,3-DNB), and nitrobenzene (NB), were obtained from Sigma-Aldrich and used as received. Picric acid (PA) was purchased from Loba Chemie. RDX and TNT were obtained from AccuStandard as their solutions. Methyl iodide purchased from HIMEDIA. All other reagents and chemicals were purchased from Merck, Alfa Aesar, etc. Milli-Q water and spectroscopic grade solvents were used for all the experiments. Components used in electronic prototype device were purchased from a local electronic market. ^{1}H NMR and ^{13}C NMR were recorded on a Bruker Ascend 600 spectrometer. Mass spectra were obtained using a Q-TOF ESI-MS instrument (model HAB 273). Emission spectra were recorded on a FluoroMax-4 spectrofluorometer. Single crystal X-ray analysis were performed on a BRUKER SMART APEX diffractometer, equipped with CCD area detector using Mo Kα radiation (λ=0.71073 A) at 296 K. The structures were solved by direct methods using SHELXL and were refined on F^2 by the fullmatrix least-squares technique using the SHELXL-97 program package. Structural illustrations were generated using MERCURY 3.3. Electrochemical measurements were carried out on a CH instruments model 700D series consisting of a three-electrode system, viz., Ag/$AgNO_3$ as the reference electrode, platinum wire as the counter electrode, and glassy carbon as the working electrodes. Tetra-n-butyl ammonium hexafluorophosphate (TBAP) in acetonitrile solution (0.1 M) and ferrocene were used as a supporting electrolyte and internal reference respectively at a scan rate of 50 mV/s under an inert atmosphere. The thickness of the deposited films on glass substrates were optimized using a Dektat-150 profilometer. Field emission scanning electron microscope (FESEM) images were recorded on a Sigma Carl ZEISS scanning electron microscope.

Microscope images were captured using Leica DM 2500P polarizing optical microscope fitted with QICAM FAST1394 camera. Circuit wizard software was used to simulate and design the prototype. All the electrical characterizations of the devices were carried out at room temperature under ambient conditions using a Keithley 4200-SCS semiconductor parameter analyzer.

5.2.2 Synthesis of N, N′-bis(3-imidazol-1-ylpropyl)-naphthalenediimide (NDIMZ)

The precursor compound NDIMZ was synthesized using an established method.[51] In brief, 1,4,5,8-naphthalenetetracarboxylic dianhydride (200 mg, 0.74 mmol) dissolved in 10 mL of dry DMF was heated at 90 °C under stirring conditions for 1h. To this, 3-(aminopropyl)imidazole (186 mg, 1.49 mmol) was added drop wise and continued to stir at 140 °C overnight. On cooling, the brown colored reaction mixture was extracted with $CHCl_3/H_2O$ thrice. The combined organic layer was evaporated to dryness and the product was purified by washing repeatedly with methanol. Yield=186 mg, 52%. ^{1}H NMR (600 MHz, DMSO-d_6, δ ppm): 8.63 (s, 4H), 7.65 (s, 2H), 7.20 (s, 2H), 6.85 (s, 2H), 4.09-4.04 (m, 4H), 2.13-2.08 (m, 4H). ^{13}C NMR (150 MHz, DMSO-d_6, δ ppm): 163.44, 137.84, 131.04, 128.90, 127.00, 126.80, 119.92, 44.73, 38.44, 29.78.

5.2.3 Synthesis of N, N′-bis(3-imidazolium-1-ylpropyl)-naphthalenediimide diiodide (NDMI)

NDIMZ (100 mg, 0.21 mmol) and methyl iodide (excess) were stirred at room temperature (RT) for 2 days in an argon atmosphere to get brown colored precipitate. Excess methyl iodide was then removed using a rotary evaporator, and the remaining precipitate was washed with $CHCl_3$ to obtain pure NDMI as solid product. Yield=123 mg, 93%. ^{1}H NMR (600 MHz, DMSO-d_6, δ ppm): 9.08 (s, 2H), 8.69 (s, 4H), 7.77 (s, 2H), 7.68 (s, 2H), 4.29-4.27 (t, 4H), 4.11-4.09 (t, 4H), 3.83 (s, 6H), 2.25-2.21 (m, 4H). ^{13}C NMR (150 MHz, DMSO-d_6, δ ppm): 163.04, 136.73, 130.57, 126.52, 126.33, 123.68, 122.33, 46.99, 37.28, 35.87, 28.32. ESI-MS, m/z (%): Calc. for $C_{28}H_{28}IN_6O_4$+: 639.1217 (100), found: 639.1236 (100).

5.2.4 Synthesis of NDMI-PA complex

PA (27 mg, 0.117 mmol) dissolved in MeOH was added dropwise to the mixture of NDMI (25 mg, 0.039 mmol) in MeOH/H_2O (8:2). The yellow colored precipitate was immediately formed which was isolated using centrifuge and washed repeatedly with CH_3OH to obtain the desired product. Yield=18 mg, 62%. ^{1}H NMR (600 MHz, CD_3CN, δ ppm): 8.72 (s, 4H), 8.57 (s, 2H), 7.59 (s, 2H), 7.47 (s, 2H), 7.36 (s, 4H), 4.28.4.25 (t, 4H), 4.20.4.18 (t, 4H), 3.84 (s, 6H) 2.33.2.28 (m, 4H). ESI-MS, m/z (%): Calc. for $C_{34}H_{30}N_9O_{11}$+: 740.2065 (100), found: 740.2070 (100).

5.2.5 Crystallization procedure for NDMI and NDMI-PA

The orange colored solid compound NDMI (5 mg) was dissolved in a mixture of MeOH/H_2O (8:2) and kept for slow evaporation at room temperature to get block-shaped crystals. The as synthesized NDMI-PA complex was dissolved in a mixture of CH_3CN/DMF (9:1) at room temperature to obtain crystals suitable for X-ray analysis.

5.2.6 Preparation of stock Solutions

For fluorescence based sensing studies, the stock solution of NDMI (1 mM), various nitroaromatics (1 mM) viz. PA, NB, 4-NP, 2,4-DNP and derivatives of aldehydes, amines, acids (1 mM), etc., were prepared in Milli-Q water, respectively. Similarly, stock solution (1 mM) of 2,4-DNT, 2,6- DNT, 2-NT, 4-NT, and 1,3-DNB were prepared in HPLC grade THF. NaCl salt solutions of various concentrations were prepared in Milli-Q water. Nitroexplosives viz. RDX and TNT were obtained as their solutions in 1:1 CH_3CN:MeOH mixture and diluted as desired.

5.2.7 Stern-Volmer plot and detection limit calculations

To study the quenching efficiency, a Stern-Volmer (SV) plot was obtained as F_0/F vs [Q], where F_0 is the initial emission intensity of NDMI and F indicates the emission intensity after adding quencher molecule [Q] i.e. PA. The curve demonstrates the linear fitting at lower quencher concentration with good correlation coefficient value 0.9928. The slope of the curve represents Stern-Volmer constant (K_{SV}). To determine the limit of detection (LOD), different NDMI solutions (16.7 μM) each containing variable concentrations of PA (1.7, 3.3, 5.0, 6.7, 8.3, and 10 μM) in HEPES buffer (10 mM, pH = 7) was subjected to fluorescence measurement by exciting at 360 nm. A curve was plotted between the change in emission intensity and concentration of PA. LOD value was then calculated using the known equation:

$$LOD = 3\sigma/S$$

Where, σ denotes standard deviation of emission intensity of NDMI in the absence of PA and S represents the slope of the curve.

5.2.8 Device fabrication and testing

To realize an economical sensor device, microscopic glass slides (1 cm × 2 cm) were used as substrates and cleaned in 3:1 mixture of H_2SO_4:H_2O_2 (piranha solution) followed by washing with deionized water. The cleaned substrates were then dried under vacuum at 100 °C for 1 h. Here, 100 nm thick strips of aluminum (Al) electrodes were deposited onto the substrates by thermal evaporation under high vacuum ($<10^{-6}$ mbar) using masking to obtain a channel with ~30 μm length (L) and ~1500 μm width (W). From 1 mM methanolic solution of NDMI, a volume of 5 μL was drop-casted on the channel between the electrodes over a controlled area. Several drop casted devices were then kept under vacuum condition and employed for vapor mode sensing after optimization using a home-built chamber. Prior to detection, various nitroaromatics (2,4-DNP, 4-NP, 2,6-DNT, 2,4-DNT, 4-NT, 2-NT, 1,3-DNB, NB, and PA) were kept for 2 days in airtight round-bottom flasks to ensure complete saturation over the area of headspace. The vapors of each nitroaromatics were injected into the chamber using airtight syringe after dilution to desired concentration by air. The concentration of vapors were calculated using the equation:[52]

$$\text{saturation concentration (ppm)}=\text{vapor pressure (VP) (mm Hg)}/760 \text{ mm of Hg } 10^6$$

where VP represents vapor pressure[53] of various nitroexplosives used.

5.2.9 Development of an electronic prototype

An electronic prototype for instant on-field detection of PA vapors was developed using simple and affordable electronic components (PCB board, resistors, IC, LED, battery, etc.) commonly available in the market. The prototype is primarily based on variation in the resistance of the device connected to the circuit after introducing PA vapors. The subsequent change in the voltage was further amplified and used to glow a suitable red light emitting diode (LED) that helps in visual detection of PA vapors.

5.3 Results and discussion

5.3.1 Synthetic scheme of NDMI

The synthetic scheme for cationic NDMI molecule is shown in **Scheme 5.1**. The as synthesized precursor molecule NDIMZ was subjected to N-methylation to obtain cationic NDMI in 93% yield. The products were well characterized by NMR and ESI-MS (**Figure A5.1-A5.5**). Cationic imidazolium groups attached onto the side chains augments the solubility of NDMI in aqueous solution and provides remarkable selectivity for PA detection without the interference of any other nitroexplosives. Due to the excellent solubility of NDMI in aqueous environment (where the solubility of PA is also very high), it has a strong tendency to interact with PA with high selectivity via simple anion exchange unlike NDIMZ; hence, NDMI was chosen for all sensing experiments.

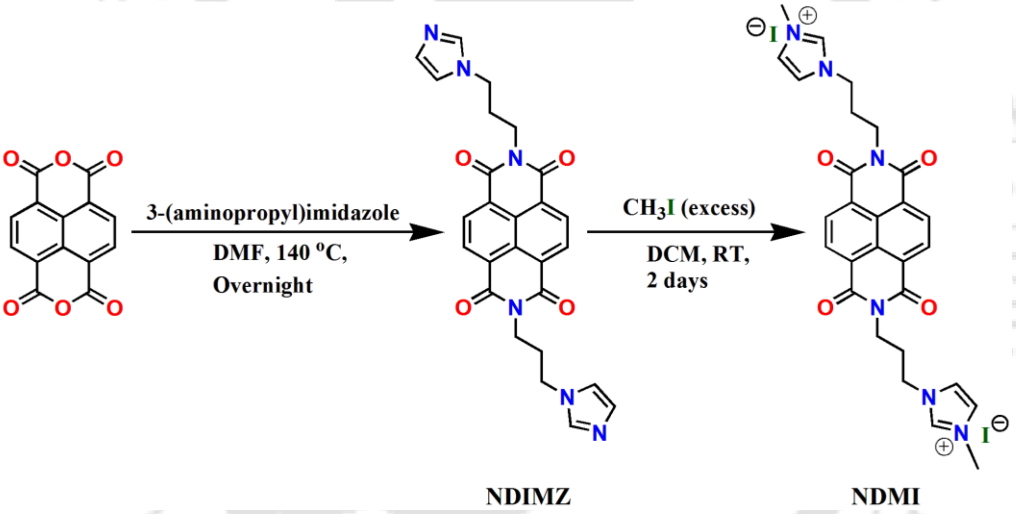

Scheme 5.1 Synthetic scheme of NDMI.

5.3.2 Structure elucidation

The cationic molecule NDMI was successfully crystallized to obtain rod-shaped crystals that were characterized by X-ray crystallographic analysis to confirm its shape, structure and molecular arrangement (**Figure 5.1a).** The crystal data set for NDMI (CCDC no. 1438645) and relevant parameters are provided in **Table A5.1**. Single crystal X-ray diffraction studies revealed that NDMI molecule crystallizes in the monoclinic crystal system with a P21/c space group. Packing arrangement of the crystal indicates that iodide anion acts as a bridge between different NDMI molecules and leads to the formation of dense self-assembled crystalline network facilitated by favorable noncovalent C−H····I interactions **(Figure A5.6).**

Note that the intermolecular π-π distance between the adjacent naphthalene units as calculated through shortest $\pi_{centroid}$-$\pi_{centroid}$ was found to be as large as ~8 Å **(Figure 5.1b)** indicating absence of π-π stacking interactions between the NDMI molecules. Thus, the iodide counter anion is believed to play a vital role in self-assembling NDMI with PA and provide the single crystalline network structures.

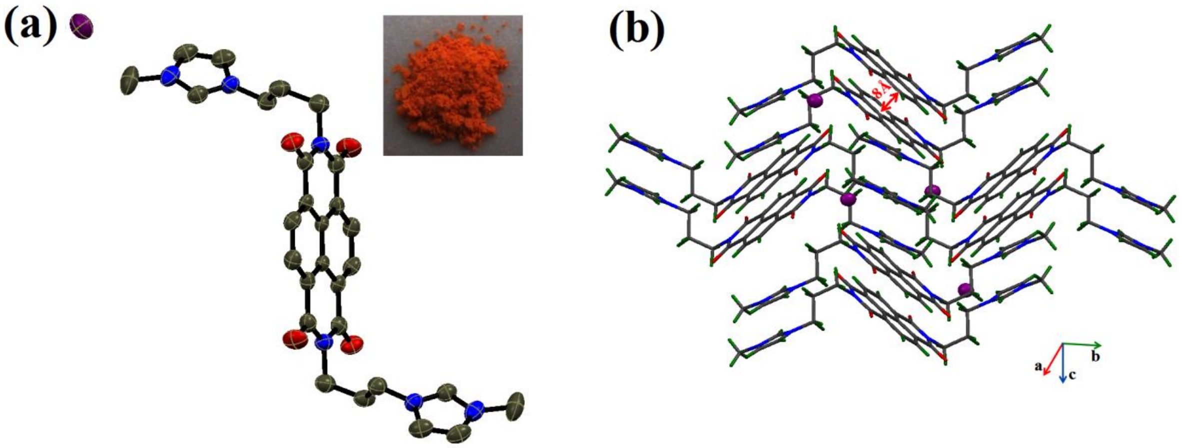

Figure 5.1 (a) ORTEP diagram of NDMI with 50% probability ellipsoid (H atoms are omitted for clarity). Inset: Color of NDMI observed with the naked eye. (b) Packing diagram of NDMI indicating intermolecular π-π distance (shortest $\pi_{centroid}$-$\pi_{centroid}$) of ~8 Å.

5.3.3 Aqueous mode detection

In addition to the strong explosive nature of PA in dry state, it is also a severe environment pollutant that can easily contaminate aquatic system owing to its high solubility in water and can cause serious health effects on humans and marine life. Considering the environmental issues, the photophysical properties of NDMI were first utilized to monitor the traces of PA in aqueous medium. The photoluminescence spectra of NDMI in water exhibited strong bands with emission maxima (λ_{em}) at 393, 414, and 438 nm, upon excitation (λ_{ex}) at 360 nm at room temperature. Sensing experiments were performed in both water as well as HEPES buffer (pH=7, 10 mM), and the results were found comparable. The fluorescence quenching titration was performed by introducing different concentration of PA to the solution of NDMI (16.67 μM). An efficient fluorescence quenching of ~96% (**Figure 5.2a**) of NDMI occurred after adding 67 μM of PA. The Stern-Volmer constant (K_{SV}) (inset of **Figure 5.2a**) and LOD (**Figure A5.7**) were found to be 58589 M^{-1} and 34.8 ppb, respectively, indicating very high sensitivity of NDMI for PA in aqueous media. Such high K_{SV} and low LOD has been reported for the first time using NDI derivative in complete aqueous media. To investigate

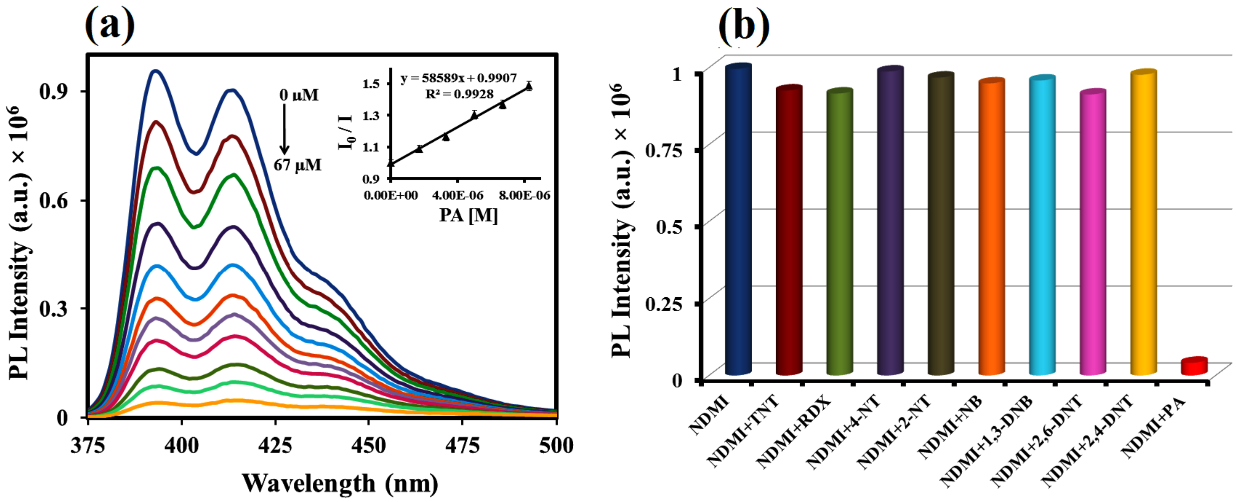

Figure 5.2 (a) Emission spectra of NDMI (16.7 µM) with various concentrations of PA in HEPES buffer (pH = 7, 10 mM). Inset: Stern-Volmer plot at lower PA concentration. (b) Bar diagram showing the effect of various other nitroexplosives (200 µM) on the emission of NDMI (16.7 µM).

the interference by other nitroaromatics on the sensing process by NDMI, quenching studies were performed with 2,6-DNT, 2,4-DNT, 4-NT, 2-NT, 1,3-DNB, NB, TNT and RDX both in HEPES buffer (pH=7, 10 mM) as well as methanol. Interestingly, these nitroaromatics did not significantly affect the emission of NDMI even at much higher concentrations (**Figure 5.2b**). The fluorescence quenching efficiency with PA was then monitored in the mixture of these nitroanalytes as well as various other functional group containing molecules (**Figure A5.8**). Remarkably, NDMI displayed significant fluorescence response toward PA even in the presence of these competing analytes in aqueous media. These results clearly indicate that NDMI probe can efficiently monitor PA in natural water systems without the interference of any other similar analytes.

5.3.4 Effect of ionic strength on PA sensing

To elucidate the effect of ionic strength on PA sensing by NDMI, the fluorescence quenching studies were performed in the solutions of different salt concentrations (0, 0.2, 0.4, 0.6, 0.8 and 1M). It was observed that an increment in the ionic strength of the solution reduces the quenching efficiency (**Figure A5.9**) which is in good agreement with the weak electrostatic interaction[54,55] between the positively charged NDMI and negatively charged PA molecules. This further confirmed the proposed anion exchange mechanism involved in the sensing of PA. Note that quenching efficiency was still ~65% in the presence of 1 M NaCl which indicates that this system can detect PA even at relatively high electrolyte concentrations in the aqueous media.

5.3.5 Complexation studies and sensing mechanism: X-ray diffraction, ^{1}H NMR, and ESI-MS

To comprehend the plausible sensing mechanism, we studied the interaction between NDMI and PA molecules via single crystal X-ray diffraction. The NDMI-PA complex was successfully crystallized to obtain rod-shaped single crystals that confirmed the formation of 1:1 complex between NDMI and PA **(Figure 5.3a).** The data set for the NDMI-PA complex (CCDC no. 1444382) and related parameters is presented in **Table A5.1**. The NDMI-PA complex crystallizes in triclinic crystal system with $\overline{P}1$ space group. The packing arrangement of the NDMI-PA crystal clearly indicates the existence of one picrate ion per NDMI via exchange of one iodide anion from the parent molecule (**Figure 5.3b**).

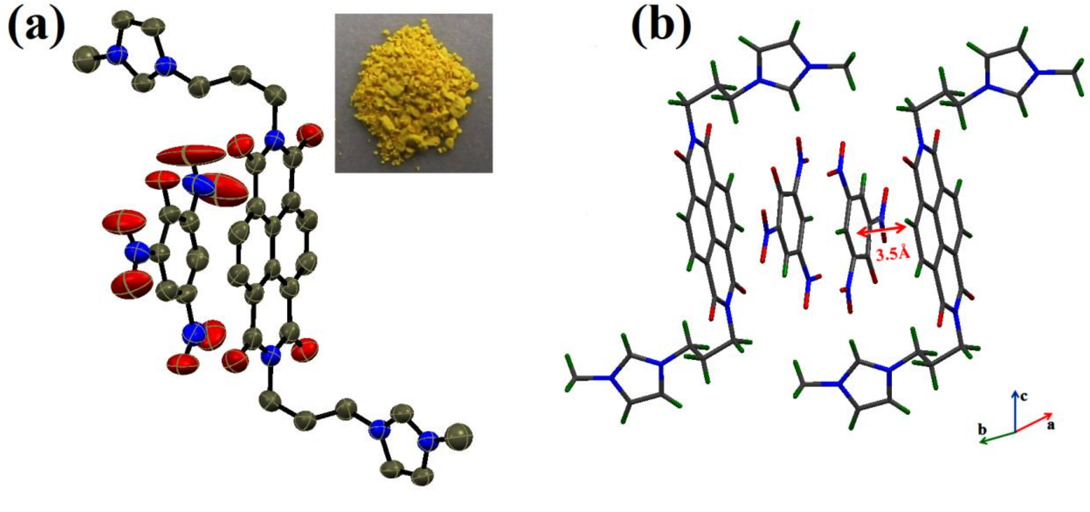

Figure 5.3 (a) ORTEP diagram of the NDMI-PA complex with 50% probability ellipsoid (H atoms are omited for clarity). Inset: Color of the NDMI-PA complex observed by the naked eye. (b) Packing diagram of the NDMI-PA complex indicating intermolecular π-π distance (shortest $\pi_{centroid}$-$\pi_{centroid}$) of 3.5 A between aromatic cores of NDMI and PA.

Interestingly, NDMI and picrate molecules were found to be self-assembled in a cooperative fashion additionally via face-to-face intermolecular π-π interactions. The shortest $\pi_{centroid}$-$\pi_{centroid}$ distances between the respective aromatic rings in the NDMI-PA complex was calculated to be 3.5 Å that strongly favors the presence of π-π stacking interaction[56,57] unlike in the parent NDMI molecule (**Figure 5.1b**). Moreover, ^{1}H NMR spectrum of the NDMI-PA complex displayed significant up field shift (0.34 ppm) of PA aromatic protons after binding with NDMI due to the ring current effect that further confirms the strong interactions between NDMI and PA via π-π stacking (**Figure 5.4**). These studies conclude that the addition of PA to NDMI results in strong π-π stacking via favorable electrostatic interactions that subsequently leads to the quenching of fluorescence of NDMI molecules in water.

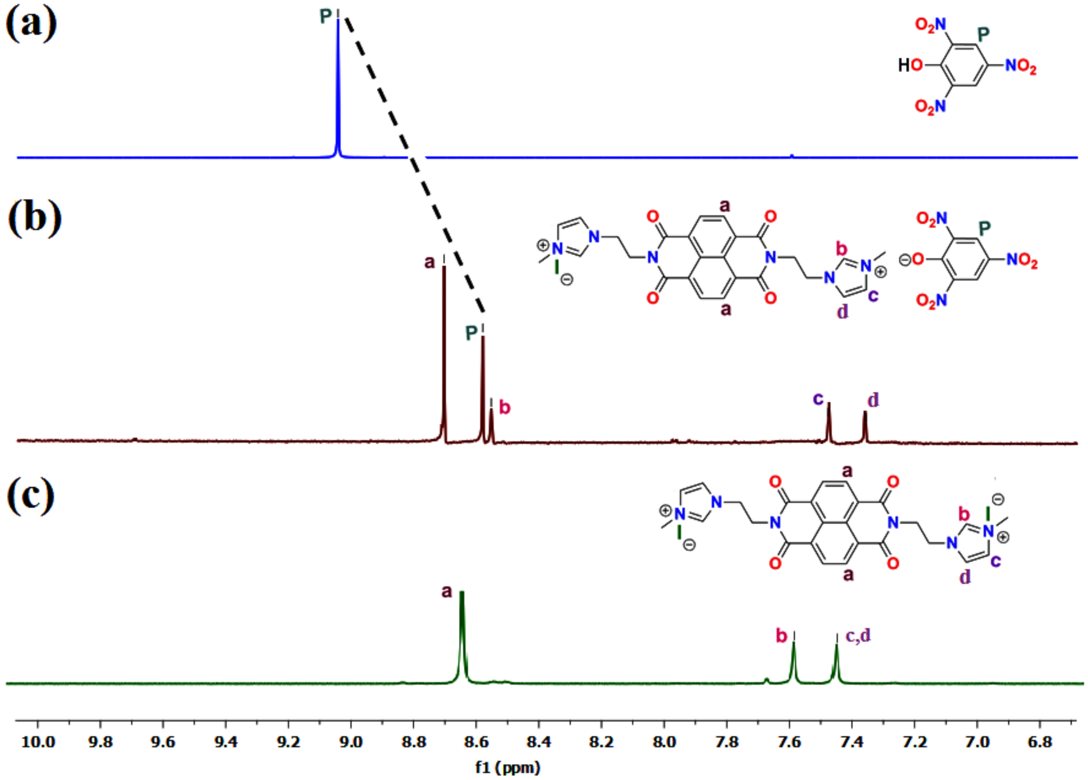

Figure 5.4 Partial ^{1}H NMR spectra of (a) picric acid (CD_3CN, 600 MHz), (b) the NDMI-PA complex (CD_3CN, 600 MHz), and (c) NDMI (DMSO-d_6, 600 MHz) indicating the formation of host-guest complex and π-π interactions.

In addition to the ^{1}H NMR, the formation of 1:1 complex between NDMI and PA was also confirmed by ESI-MS (**Figure A5.11**). Although the structure of few PA probes has been elucidated earlier via single crystal X-ray method, the structure of complex, i.e., probe assembled with PA via anion exchanged strong π-π stacking, has remained elusive thereby evading proof of the complex formation mechanism.[58,59] Hence, X-ray diffraction study of NDMI-PA complex not only provided valuable insights into the type of interaction that imparted the high selectivity to the probe but also assisted in deducing the sensing mechanism proficiently.

5.3.6 Electrochemical measurements

Electron transfer is one of the most common phenomenon to be involved in fluorescence quenching process with nitroexplosives. To explore the possibility of electron transfer processes in the NDMI system, the highest occupied molecular orbital (HOMO) level and lowest unoccupied molecular orbital (LUMO) level of NDMI molecule was obtained via cyclic voltammetry studies (**Figure 5.5a**, see details in Appendix). It is evident that there is a possibility of ground state electronic charge transfer from the HOMO of the picrate,[60] to the LUMO of NDMI molecule, resulting in an efficient fluorescence quenching (**Figure 5.5b**). Moreover, the HOMO levels of other nitroexplosives,[60-62] are significantly lower than the LUMO level of NDMI, thereby discarding the possibility of electron transfer. Thus, the occurrence of an additional electron transfer process in the quenching mechanism may also be the reason for the astonishing sensitivity and remarkable selectivity of the probe NDMI toward PA.

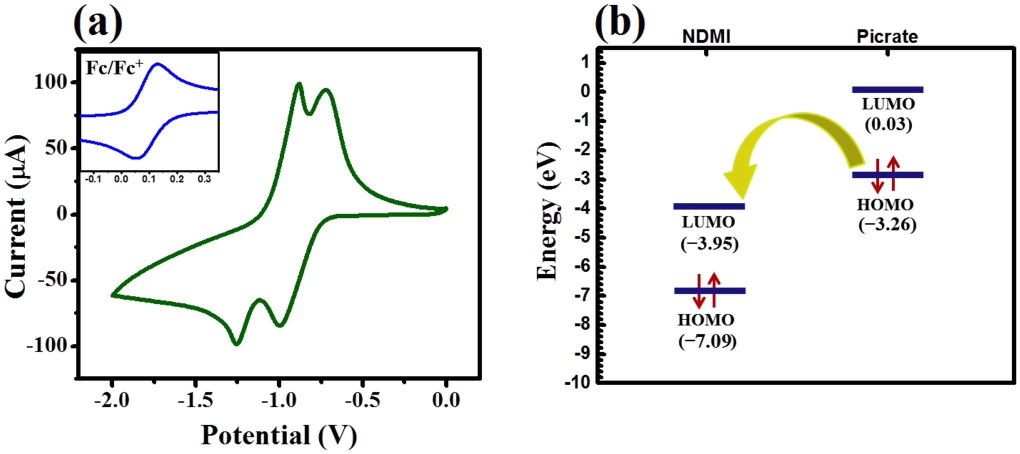

Figure 5.5 (a) Cyclic voltammogram (CV) of NDMI film obtained on glassy carbon electrode with a scan rate of 50 mV/s. Inset: CV of ferrocene. (b) Pictorial representation of possible electron transfer from HOMO of picrate to the LUMO of NDMI.

5.3.7 Control studies

Since, Coulombic attraction plays a vital role in sensing process, control experiments were also performed using other nitroaromatics possessing polar –OH groups viz. 4-NP and 2,4-DNP. The order of quenching was found as 4-NP < 2,4-DNP < PA which are in good agreement with their dissociation abilities in aqueous solution (**Figure A5.12**). Thus, more favorable electrostatic interaction is expected between cationic NDMI and PA that subsequently results in higher signal response compared to 4-NP and 2,4-DNP.

5.3.8 Vapor mode detection

Napthalenedimide derivatives comprising of π-electron rich cores have been extensively used as organic semiconducting materials due to their numerous features viz. tunable optoelectronic properties, excellent chemical, thermal, photo stabilities and molecular self-assembly behavior. Distinct micro/nanostructures of such materials enable efficient transport of electrons, photons, and excitons due to size confinement effect. FESEM and optical microscope images of drop-casted NDMI on a substrate revealed the formation of a cluster of microrods along with 3D flower-like structures due to self-association of individual rods (**Figure 5.6**).

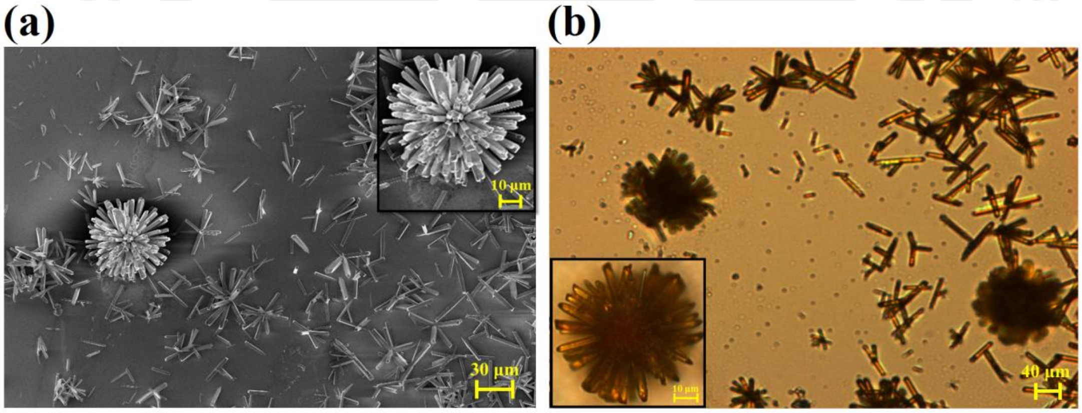

Figure 5.6 (a) FESEM and (b) optical microscope images of drop-casted NDMI on a substrate revealed the formation of large number of microrods along with some 3D flowerlike structures. Insets: Magnifying image of selected daisy-like structures.

To explore this distinct feature of NDMI for vapor mode sensing experiments, a two terminal sensor device was fabricated by growing these microrods on Al deposited inexpensive glass substrates. For current vs voltage i.e. I-V measurements, the device was kept in a test chamber and connected to a Keithley 4200 SCS semiconductor parameter analyzer. By sweeping the voltage from -10 to +10 V, the I-V characteristic of the sensor device was recorded, revealing a nonlinear nature of the curve due to the semiconducting behavior of NDMI (**Figure 5.7a).** To explore the vapor mode sensing response of NDMI fabricated sensor device toward PA, various concentrations of PA were systematically introduced by controlling the volume of vapors (**Figure 5.7b**). After injecting 584 ppt of PA vapors into the chamber, the sensor device displayed significant increment in output current signal with a very short response time (8s). Upon turning off the PA source, current intensity recovered to its initial level with a slightly higher recovery time (12s) (**Figure A5.13**). The quantification was then performed by introducing various concentrations of PA vapors into the test chamber. The current response increased linearly with increasing concentration of PA vapors (**Figure 5.7b**). Furthermore, the recyclability of the device was checked by exposing a certain concentration of PA vapors (260 ppt) continuously after definite interval of time into the testing chamber. Almost similar enhancement in current intensity (**Figure 5.7c**) was monitored after each exposure confirming the feasibility of the sensor device for real-time applications. To calculate LOD, a calibration curve was constructed by plotting the maximum current intensity against the concentration of PA vapors (**Figure A5.14**). The curve demonstrates a linear relationship with the correlation coefficient (R^2) value of 0.9844. The LOD value was found to be 2.92 ppt which is exceptionally high and very unique among all the reported methods for PA sensing in vapor mode. **(Table A5.2)**

In organic semiconductor based sensor devices, the interaction between the sensing film and analyte molecules usually occurs via adsorption and/or diffusion of the analyte vapors onto the surface of the film. The nature of such interactions may be dipole-dipole, dipole-charge, acid-base, Coulombic, hydrogen bonding, etc. This leads to the variation in majority charge carriers and subsequently current through the formation of possible charge transfer complex.[64-66] Furthermore, the self-assembled well-organized nano/microstructured network in such semiconductor device facilitates the pathways for efficient charge transport due to high surface area for analyte molecules. The increase in current intensity of the NDMI sensor device after introducing PA vapors can be attributed to the additional channel charge carriers induced by the dipole-charge interaction and/or electrostatic interaction. Since, PA has a dipole moment with partial negative charge on its oxygen atom due to the presence of a polar −OH group,[67] it can orient itself onto the surface of the film in a cooperative manner via dipole-charge as well as electrostatic interaction. These partial negative charges can induce an equal density of positive charges at the interface that drastically increase the ionic conductivity and subsequently the current. However, other nitroaromatics did not display significant enhancement in the current intensity of the sensor device (except 4-NP and 2,4-DNP which showed ~40% and ~30% response compared to PA). Such anomalous behavior can be ascribed to the absence of polar −OH groups in these nitroaromatics that promote dipole-charge as well as electrostatic interaction between NDMI and analyte at the interface.

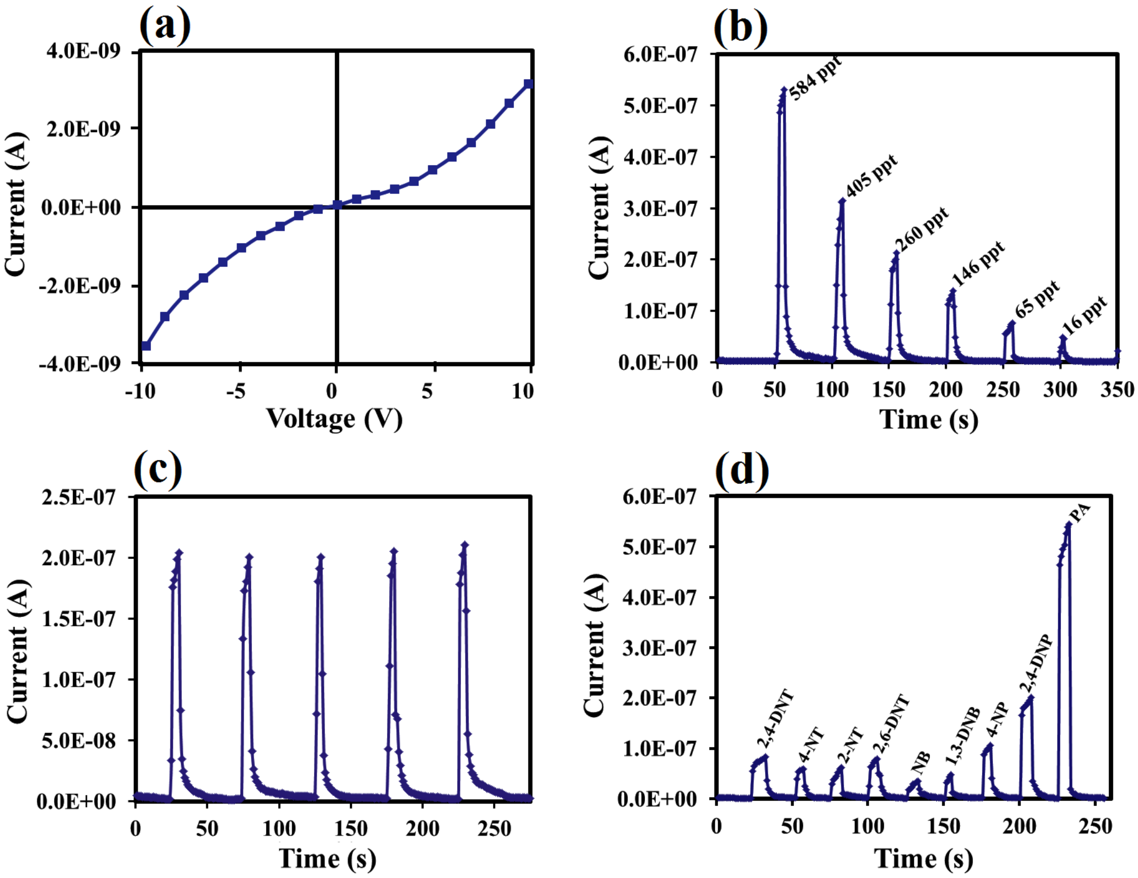

Figure 5.7 (a) Current-voltage (I-V) characteristic curve of NDMI on sweeping the voltage from −10 to +10 V. (b) Sensing response of the device with variable concentration of PA (584-16 ppt). Argon was purged after each injection to completely recover the original current of the device. (c) Repeatability test of the device with 260 ppt of PA. (d) Selectivity studies of NDMI with various nitroaromatics (500 ppb) and nitrophenols (584 ppt).

To elucidate the selectivity of the sensor device, analogous sensing experiments were carried out by exposing the vapors of various other nitroaromatics (**Figure 5.7d**). Remarkably, the responses of the sensor device to other analytes were comparatively lower or insignificant even at much higher concentrations compared to PA, confirming the efficiency of this NDMI device for practical purposes under realistic conditions.

5.3.9 Visual detection using an electronic prototype

The circuit diagram of the sensor module used for the detection of PA vapors is presented in **Figure 5.8a**. The circuit is a combination of comparator and amplifier using LM324 OPAMP (Operational Amplifier) IC. The first stage of the circuit (OA-1) is a comparator in which the voltage at the inverting terminal is kept fixed. The second stage (OA-2) represents an amplifier whose output is fed to the non-inverting terminal of OA-1. The amplifier stage is configured in such a way that its output voltage is inversely proportional to the resistance of the device. This amplifier stage is required due to very high operative resistivity range of the device (detection channel), which is apparent from the I-V characteristics. Thus, to accommodate such a high resistivity value in a potential divider configuration using commercially available resistors, the corresponding change in voltage needs to be amplified for detection. As the resistance of the device decreases in the presence of the analyte, we obtain two different voltages: V_{o2} (in the absence of PA) and V_{o2}' (in the presence of PA) at the output terminal of OA-2. The corresponding amplified value V_{3+} at the non-inverting terminal of OA-1 varies accordingly. The voltage V_{2-} at the inverting terminal of OA-1 is set by means of a potential divider circuit to maintain the relation V_{3+} (in absence of analyte) < V_{2-} < V_{3+} (in the presence of analyte) which is the required condition for this prototype to work. Once it is fulfilled, the presence of analyte vapor (PA) is indicated by the glowing of the red light emitting diode (LED_{on}) (**Figure 5.8b and 5.8b**). Voltage V_{2-} determines the threshold limit, or in other words, the sensitivity of the circuit, i.e., the minimum concentration of analyte vapors the circuit can detect. The threshold limit set for the current prototype was 260 ppt. This threshold can be changed or optimized accordingly by changing the combination of the potential divider circuit attached with it. The components used in the fabrication of this simple, low-cost, and portable miniature prototype are easily accessible from the marketplace and provides one of its kind, handy and economic detection platform for the on-site detection of PA. Thus, the present device prototype can be installed and used for the rapid on-site detection of PA vapors under ambient conditions at various places such as busy markets, bus and train stations, airports, and industrialized locations or carried by security personnel at desired locations for repeated use.

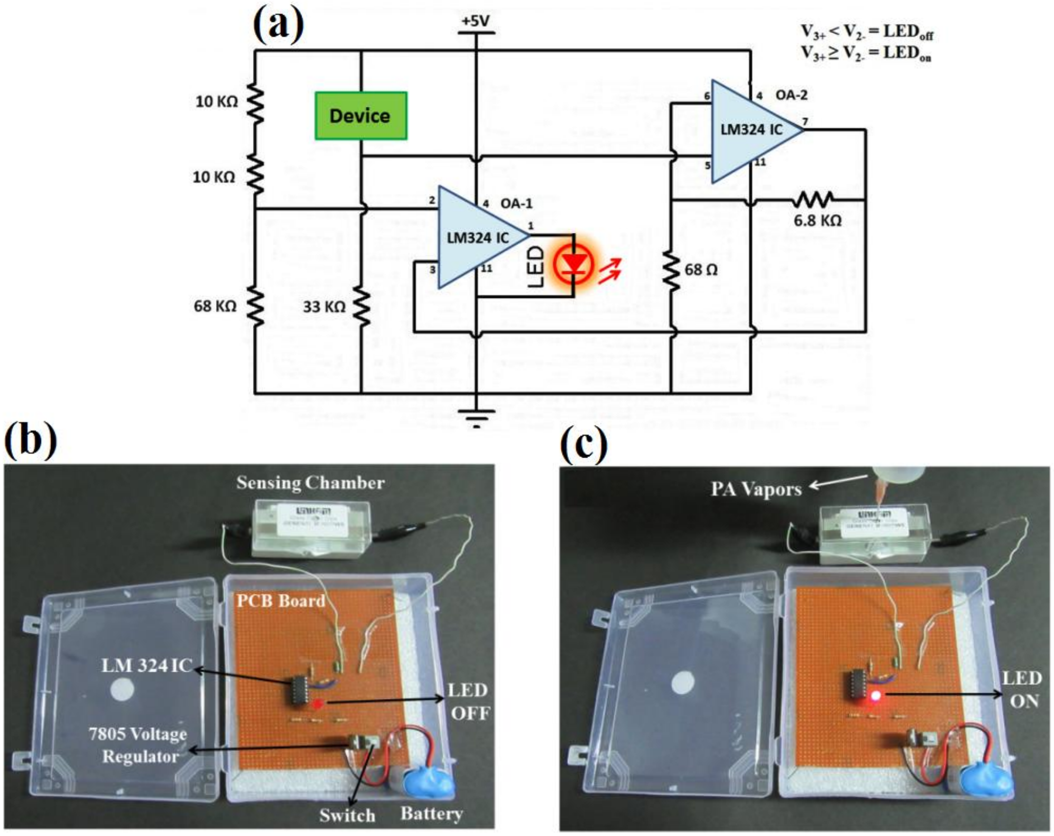

Figure 5.8 (a) Circuit diagram of the electronic prototype obtained using circuit wizard simulator. Digital photographs of electronic prototype snapped (b) before (LED_{off} state) and (c) after exposure of PA vapors (LED_{on} state).

Using this semiconductor NDMI probe, the dual mode detection of PA in solution state (PL spectroscopy) as well as in vapor phase (two terminal electronic devices with electrical/LED output), is demonstrated for the first time. This NDMI probe shows remarkable selectivity and sensitivity by forming stable complexes with picrate molecules in water and self-assembled in a co-operative fashion via face-to-face intermolecular π-π interactions with very short $\pi_{centroid}$-$\pi_{centroid}$ distances of 3.5 Å between the respective aromatic rings in the NDMI-PA complex confirming the presence of π-π stacking interaction and efficient anion exchange. Such dual mode detection of any analyte using a semiconducting probe is a rare example seldom reported in literature previously thereby providing newer direction in developing efficient probes in the future for onsite detection of explosive materials.

5.4 Conclusion

In summary, the dual mode detection of most widespread nitroexplosive and highly water-soluble toxicant picric acid (PA) is achieved for the first time using an imidazolium incorporated naphthalene diimide, NDMI both in solution state (fluorescence spectroscopy) as well as in vapor phase (two terminal electronic device with electrical/LED output), with detection limit levels of ppt. High sensitivity and remarkable selectively is attributed to Coulombic attraction, dipole-charge interaction, anion exchange, strong π-π stacking and favorable electron transfer as revealed via single crystal X-ray structures of NDMI and NDMI-PA complex, ^{1}H NMR studies, cyclic voltammetry and ESI-MS. Self-assembled microrods of NDMI were fabricated on a simple two-terminal device to realize highly sensitive vapor mode detection of PA. Finally, a cost-effective and portable electronic prototype is developed for visual and instant on-site detection of PA vapors under very realistic conditions. These unique features of NDMI make this protocol unique and practical to prevent worldwide terrorist threats and monitoring environmental pollution rapidly.

5.5 References

(1) Sun, X.; Wang, Y.; Lei, Y. *Chem. Soc. Rev.*, **2015**, *44*, 8019.

(2) Shanmugaraju, S.; P. S. Mukherjee, P. S. *Chem. Eur. J.*, **2015**, *21*, 6656.

(3) Salinas, Y.; Martinez-Manez, R.; Marcos, M. D.; Sancenón, F.; Costero, A. M.; Parra, M.; Gil, S. *Chem. Soc. Rev.*, **2012**, *41*, 1261.

(4) Riskin, M.; Tel-Vered, R.; Willner, I. *Adv. Mater*., **2010**, *22*, 1387.

(5) Shanmugarajua, S.; Mukherjee, P. S. *Chem. Commun*., **2015**, *51*, 16014.

(6) Akhavan, J. *Chemistry of Explosives, Royal Society of Chemistry*, 2nd edn, 2004.

(7) Wollin, K.-M.; Dieter, H. H. *Arch. Environ. Contam. Toxicol*., **2005**, *49*, 18.

(8) Sylvia, J. M.; Janni, J. A.; Klein, J. D.; Spencer, K. M. *Anal. Chem*., **2000**, *72*, 5834.

(9) Walsh, M. E. *Talanta* **2001**, *54*, 427.

(10) Hill, H. H.; Simpson, G. *Field Anal. Chem. Technol*., **1997**, *1*, 119.

(11) Ostafin, M.; Nogaj, B. *Measurement* **2007**, *40*, 43.

(12) Krausa, M.; Schorb, K. *J. Electroanal. Chem*., **1999**, *461*, 10.

(13) Rochat, S.; Swager, T. M. *ACS Appl. Mater. Interfaces* **2013**, *5*, 4488.

(14) Sancheza, J. C.; Trogler, W. C. *J. Mater. Chem*., **2008**, *18*, 3143.

(15) Palma-Cando, A.; Scherf, U. *ACS Appl. Mater. Interfaces* **2015**, *7*, 11127.

(16) Palma-Cando, A.; Brunklaus, G.; Scherf, U. *Macromolecules* **2015**, *48*, 6816.

(17) Dong, W.; Fei, T.; Palma-Cando, A.; Scherf, U. *Polym. Chem*., **2014**, *5*, 4048.

(18) Räupke, A.; Palma-Cando, A.; Shkura, E.; Teckhausen, P.; Polywka, A.; Gorrn, P.; Scherf, U.; Riedl, T. *Sci. Rep*., **2016**, *6*, 29118.

(19) Hu, Z.; Deiberta, B. J.; Li, J. *Chem. Soc. Rev*., **2014**, *43*, 5815.

(20) Zhang, C.; Sun, L.; Yan, Y.; Li, J.; Song, X.; Liu, Y.; Liang, Z. *Dalton Trans*., **2015**, *44*, 230.

(21) Nagarkar, S. S.; Joarder, B.; Chaudhari, A. K.; Mukherjee, S.; Ghosh, S. K. *Angew. Chem. Int. Ed*., **2003**, *52*, 2881.

(22) Qin, J.; Ma, B.; Liu, X.-F.; Lu, H.-L.; Dong, X.-Y.; Zang, S.-Q.; Hou, H. *J. Mater. Chem. A* **2015**, *3*, 12690.

(23) Ghosh, S.; Gole, B.; Bar, A. K.; Mukherjee, P. S. *Organometallics* **2009**, *28*, 4288.

(24) Wang, M.; Vajpayee, V.; Shanmugaraju, S.; Zheng, Y.; Zhao, R. Z.; Kim, H.; Mukherjee, P. S.; Chi, K. W.; Stang, P. J. *Inorg. Chem*., **2011**, *50*, 1506.

(25) Sandhu, S.; Kumar, R.; Singh, P.; Mahajan, A.; Kaur, M.; Kumar, S. *ACS Appl. Mater. Interfaces* **2015**, *7*, 10491.

(26) Kartha, K. K.; Sandeep, A.; Praveen, V. K.; Ajayaghosh, A. *Chem. Rec*., **2015**, *15*, 252.

(27) Salinas, Y.; Manez, R. M.; Jeppesen, J. O.; Petersen, L. H.; Sancenon, F.; Marcos, M. D.; Soto, J.; Guillem, C.; Amorós, P. *ACS Appl. Mater. Interfaces* **2013**, *5*, 1538.

(28) Salinas, Y. Y.; Agostini, A.; Esteve, E. P.; Máñez, R. M.; Sancenon, F.; Marcos, M. D.; Soto, J.; Costero, A. M.; Gil, S.; Parra M.; Amorósf, P. *J. Mater. Chem. A* **2013**, *1*, 3561.

(29) Bhalla, V.; Kaur, S.; Vij, V.; Kumar, M. *Inorg. Chem*., **2013**, *52*, 4860.

(30) Bhalla, V.; Gupta, A.; Kumar, M.; Rao, D. S. S.; Prasad, S. K. *ACS Appl. Mater. Interfaces* **2013**, *5*, 672.

(31) Vij, V.; Bhalla, V.; Kumar, M. *ACS Appl. Mater. Interfaces* **2013**, *5*, 5373.

(32) Mukherjee, S.; Desai, A. V.; Manna, B.; Inamdar, A. I.; Ghosh, S. K. *Cryst. Growth Des*., **2015**, *15*, 4627.

(33) Shaw, P. E.; Chen, S. S. Y.; Wang, X.; Burn, P. L.; Meredith, P. *J. Phys. Chem. C* **2013**, *117*, 5328.

(34) Zhang, K.; Zhou, H.; Mei, Q.; Wang, S.; Guan, G.; Liu, R.; Zhang, J.; Zhang, Z. *J. Am. Chem. Soc*., **2011**, *133*, 8424.

(35) Xu, S.; Lu, H. *Chem. Commun*., **2015**, *51*, 3200.

(36) Huang, J.; Gu, J.; Meng, Z.; Jia, X.; Xi, K. *Nanoscale* **2015**, *7*, 15413.

(37) Sun , X.; He, J.; Meng, Y.; Zhang, L.; Zhang, S.; Ma, X.; Dey, S.; Zhao, J.; Lei, Y. *J. Mater. Chem. A* **2016**, *4*, 4161.

(38) Chen, P. C.; Sukcharoenchoke, S.; Ryu, K.; Gomez de Arco, L.; Badmaev, A.; Wang, C.; Zhou, C. *Adv. Mater*., **2010**, *22*, 1900.

(39) Roberts, M. E.; Sokolov, A. N.; Bao, Z. *J. Mater. Chem*., **2009**, *19*, 3351.

(40) Kalita, A.; Hussain, S.; Malik, A. H.; Subbarao, N. V. V.; Iyer, P. K. *J. Mater. Chem. C* **2015**, *3*, 10767.

(41) Huang, J.; Dawidczyk, T. J.; Jung, B. J.; Sun, J.; Mason, A. F.; Katz, H. E. *J. Mater. Chem*., **2010**, *20*, 2644.

(42) Kong, H.; Jung, B. J.; Sinha, J.; Katz, H. E. *Chem. Mater*., **2012**, *24*, 2621.

(43) Gogoi, B.; Paul, N.; Chowdhury, D.; Sarma, N. S. *J. Mater. Chem. C* **2015**, *3*, 11081.

(44) Kong, H.; Sinha, J.; Sun, J.; Katz, H. E. *Adv. Funct. Mater*., **2013**, *23*, 91.

(45) Zu, B.; Guo, Y.; Dou, X. *Nanoscale* **2013**, *5*, 10693.

(46) Wang, C.; Dong, H.; Hu, W.; Liu, Y.; Zhu, D. *Chem. Rev.*, **2012**, *112*, 2208.

(47) Kalita, A.; Subbarao, N. V. V.; Iyer, P. K. *J. Phys. Chem. C* **2015**, *119*, 12772.

(48) Dey, A.; Kalita, A.; Iyer, P. K. *ACS Appl. Mater. Interfaces* **2014**, *6*, 12295.

(49) Meng Q.; Hu, W. *Phys. Chem. Chem. Phys*., **2012**, *14*, 14152.

(50) Bhosale, S. V.; Jani, C. H.; Langford, S. J. *Chem. Soc. Rev.*, **2008**, *37*, 331.

(51) Jiang, J. J.; Yan, C.; Pan, M.; Wang, Z.; Deng, H. Y.; He, J. R.; Yang, Q. Y.; Fu, L.; Xu, X. F.; Su, C. Y. *Eur. J. Inorg. Chem*., **2012**, *2012*, 1171.

(52) Malik, A. H.; Hussain, S.; Kalita, A.; Iyer, P. K. *ACS Appl. Mater. Interfaces* **2015**, *7*, 26968.

(53) Ewing, R. G.; Waltman, M. J.; Atkinson, D. A.; Grate, J. W.; Hotchkiss, P. J. *Trends Anal. Chem*., **2013**, *42*, 35.

(54) Janiak, C. A. *J. Chem. Soc., Dalton Trans*. **2000**, *2000*, 3885.

(55) Chen, P. Y.; Zhang, L.; Zhu, S. G.; Cheng, G. B. *Crystals* **2015**, *5*, 346.

(56) Chowdhury, A.; Mukherjee, P. S. *J. Org. Chem*., **2015**, *80*, 4064.

(57) Peng, Y.; Zhang, A.-J.; Dong, M.; Wang, Y.-W. *Chem. Commun.*, **2011**, *47*, 4505.

(58) Sandanaraj, B. S.; Demont, R.; Aathimanikandan, S. V.; Savariar, E. N.; Thayumanavan. S. *J. Am. Chem. Soc.*, **2006**, *128*, 10686.

(59) Sandanaraj, B. S.; Bayraktar, H.; Krishnamoorthy, K.; Knapp, M. J.; Thayumanavan, S. *Langmuir* **2007**, *23*, 3891.

(60) Hussain, S.; Malik, A. H.; Afroz, M. A.; Iyer, P. K. *Chem. Commun*., **2015**, *51*, 7207.

(61) Roy, B.; Bar, A. K.; Gole, B.; Mukherjee, P. S. *J. Org. Chem.*, **2013**, *78*, 1306.

(62) Dutta, P.; Saikia, D.; Adhikary, N. C.; Sarma, N. S. *ACS Appl. Mater. Interfaces* **2015**, *7*, 24778.

(63) Lasitha, P.; Prasad, E. *RSC Adv*., **2015**, *5*, 41420.

(64) Zhang, C.; Chen, P.; Hu, W. *Chem. Soc. Rev*., **2015**, *44*, 2087.

(65) Duarte, D.; Dodabalapur, A. *J. Appl. Phys*., **2012**, *111*, 044509.

(66) Torsi, L.; Magliulo, M.; Manoli, K.; Palazzo, G. *Chem. Soc. Rev.*, **2013**, *42*, 8612.

(67) Jeong, Y. T.; Cobb, B. H.; Lewis, S. D.; Dodabalapur, A.; Lu, S.; Facchetti, A.; Marks, T. J. *Appl. Phys. Lett*., **2008**, *93*, 133304.

5.6 Appendix

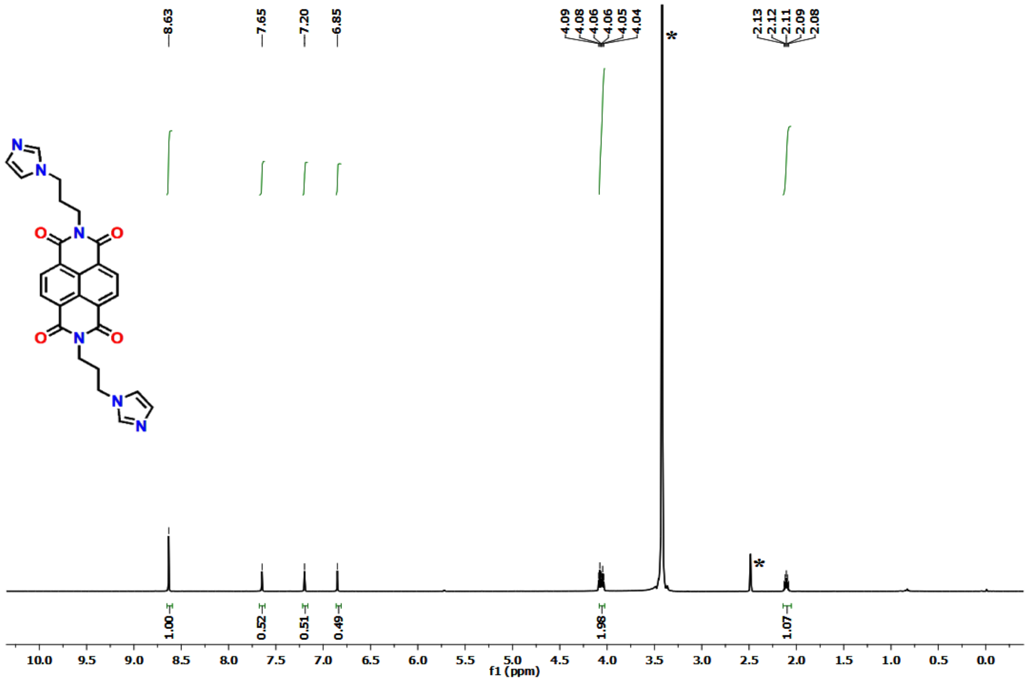

Figure A5.1 ^{1}H NMR (600 MHz, DMSO-d_6) spectra of NDIMZ.

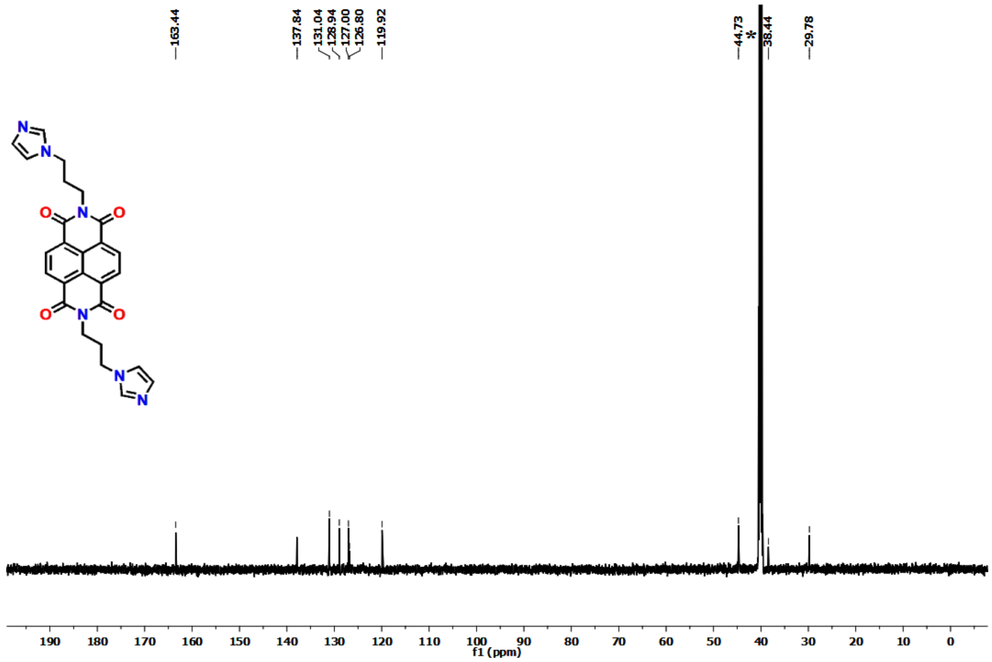

Figure A5.2 ^{13}C NMR (150 MHz, DMSO-d_6) spectra of NDIMZ.

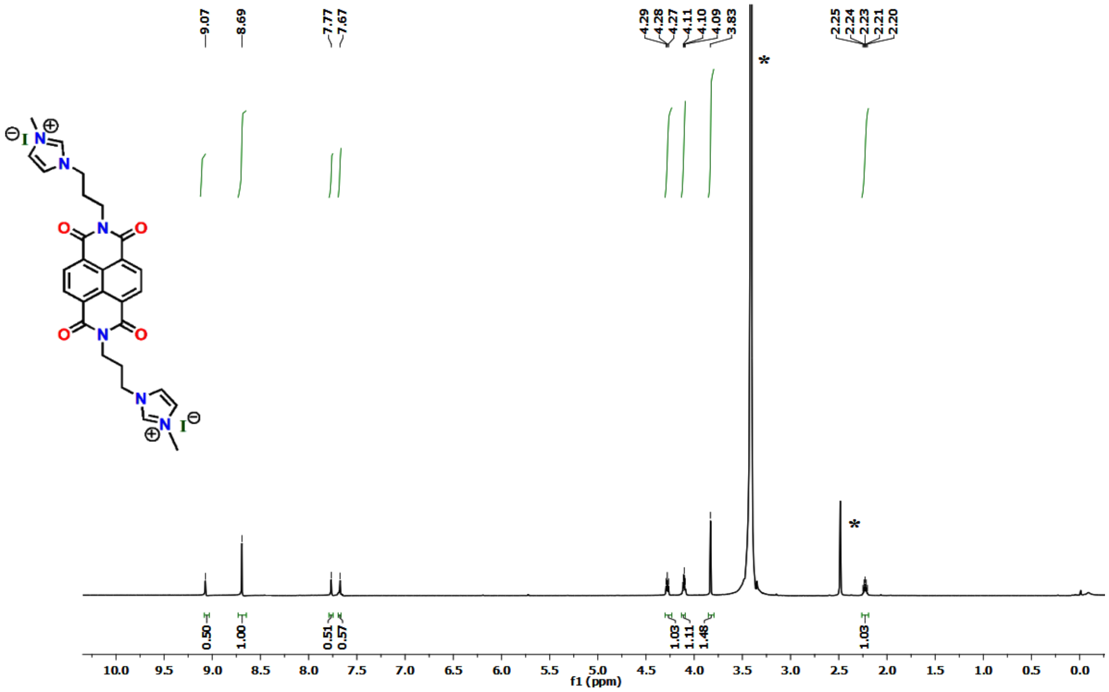

Figure A5.3 ^{1}H NMR (600 MHz, DMSO-d_6) spectra of NDMI.

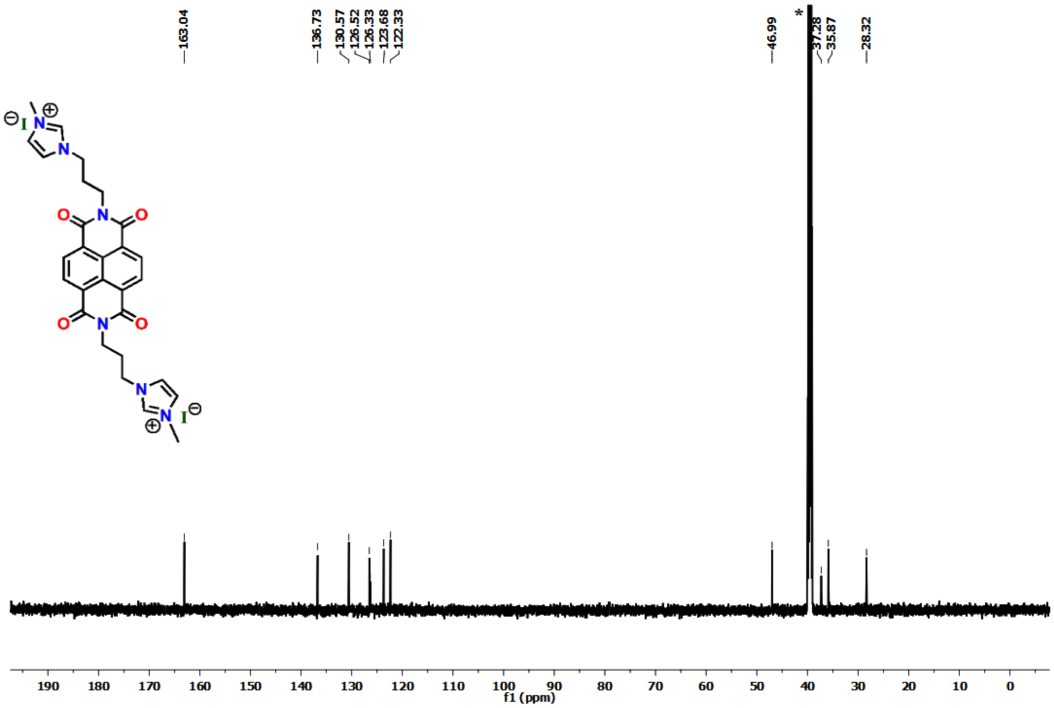

Figure A5.4 ^{13}C NMR (150 MHz, DMSO-d_6) spectra of NDMI.

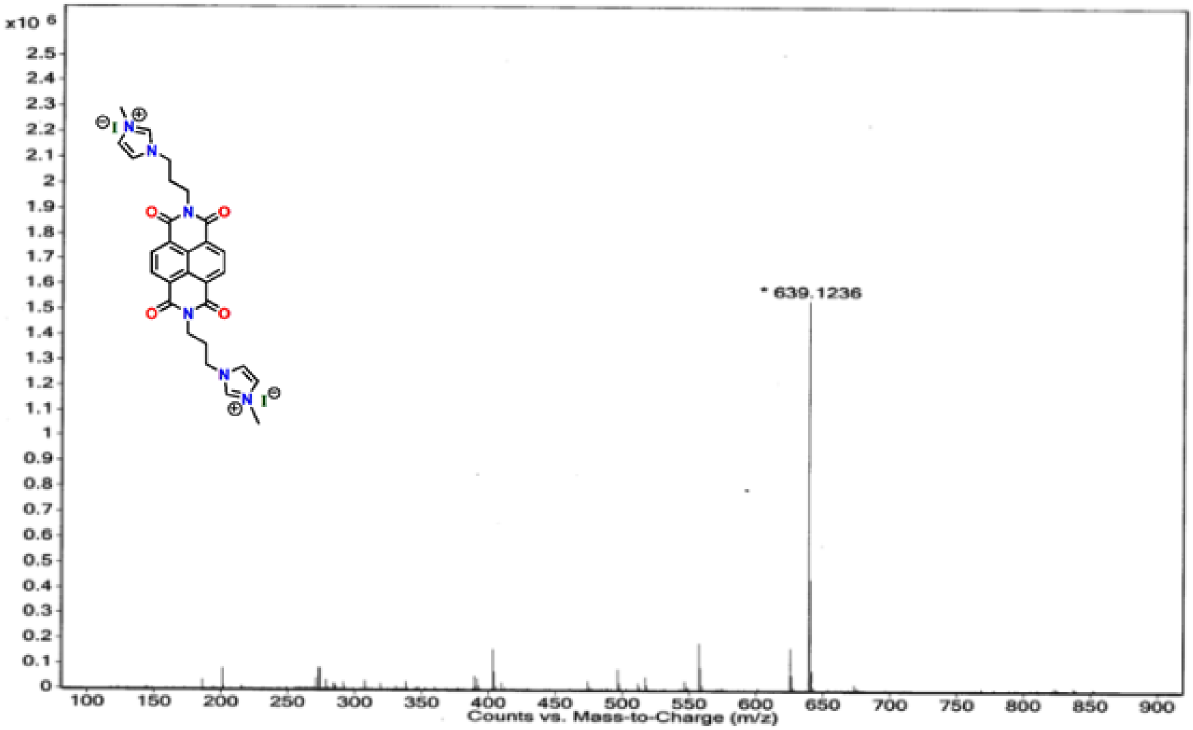

Figure A5.5 ESI-MS spectra of NDMI.

Table A5.1. Crystallographic data from single crystal XRD.

Identification code	**NDMI**	**NDMI-PA complex**
Empirical formula	C28 H28 I2 N6 O4	C40 H32 N12 O18
Formula weight	766.36	968.78
Temperature/K	296(2)	296(2)
Wavelength/ Å	0.71073	0.71073
Crystal system	monoclinic	Triclinic
Space group	P 21/c	P-1
a/ Å	8.0011(6)	10.2706(6)
b/ Å	13.7926(10)	10.4147(6)
c/ Å	13.6850(10)	11.7961(12)
α/°	90	101.167(5)

β/°	103.864(5)	98.645(5)
γ/°	90	119.207(3)
V/ Å^3	1466.22(19)	1035.40(14)
Z	2	1
μ (mm^{-1})	2.189	0.126
D, g cm^{-3}	1.736	1.554
F(000)	752.0	462
Theta range for data collection	2.12-28.39°	1.84-25.50°
Total no. of reflections	3494	3709
Goodness-of-fit on F^2	0.883	1.118
R1 [I > 2σ(I)]	0.0398	0.0745
wR2 [I > 2σ(I)]	0.0789	0.2414

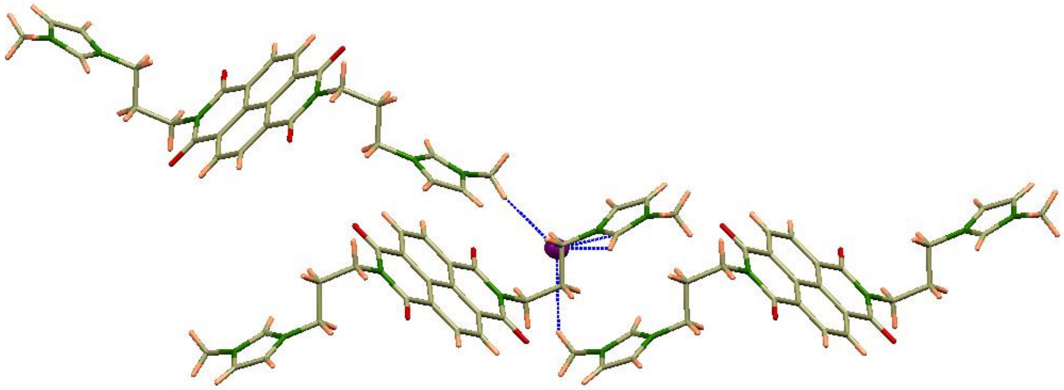

Figure A5.6 Packing arrangement of NDMI crystals showing C−H····I interactions.

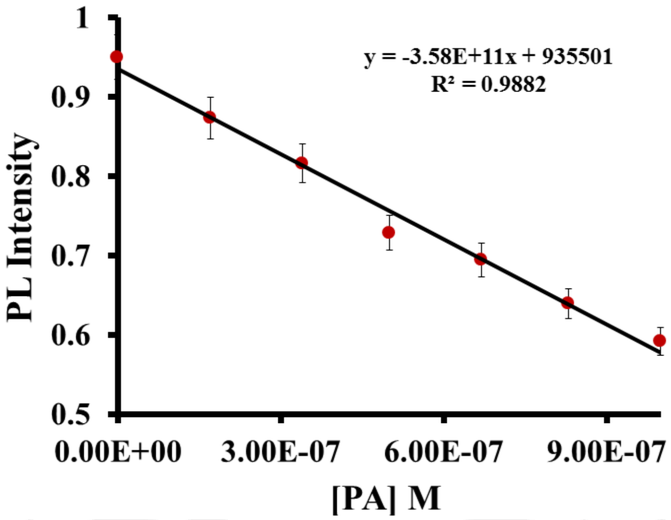

Figure A5.7 Detection limit plot of PA in aqueous media.

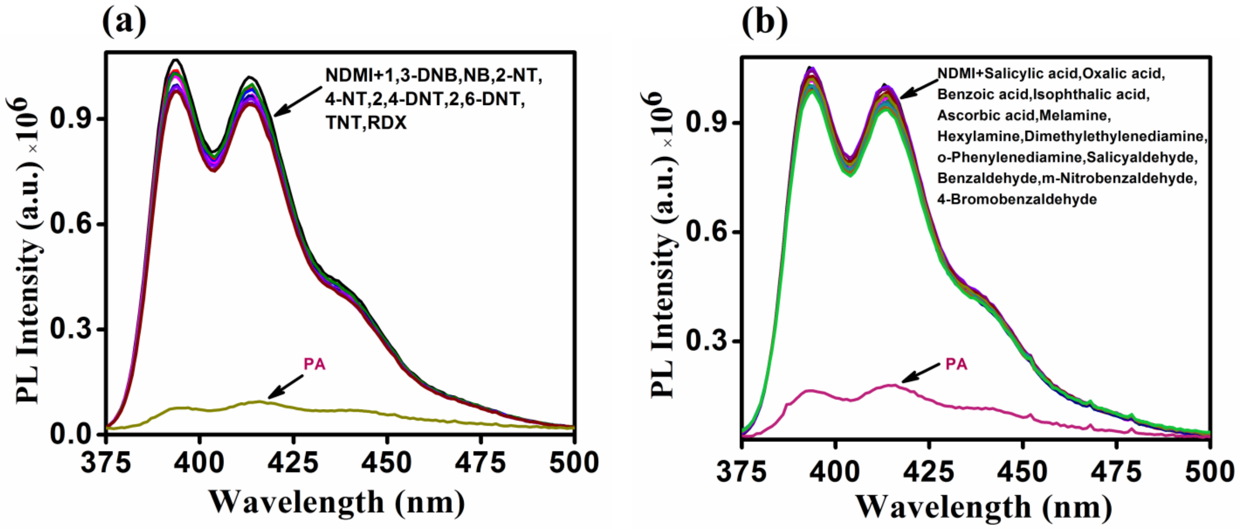

Figure A5.8 Fluorescence quenching of NDMI (16.7 µM) with PA (67 µM) in the presence of various other (a) nitroaromatics and (b) competing analytes like aldehydes, amines, acids etc. (200 µM).

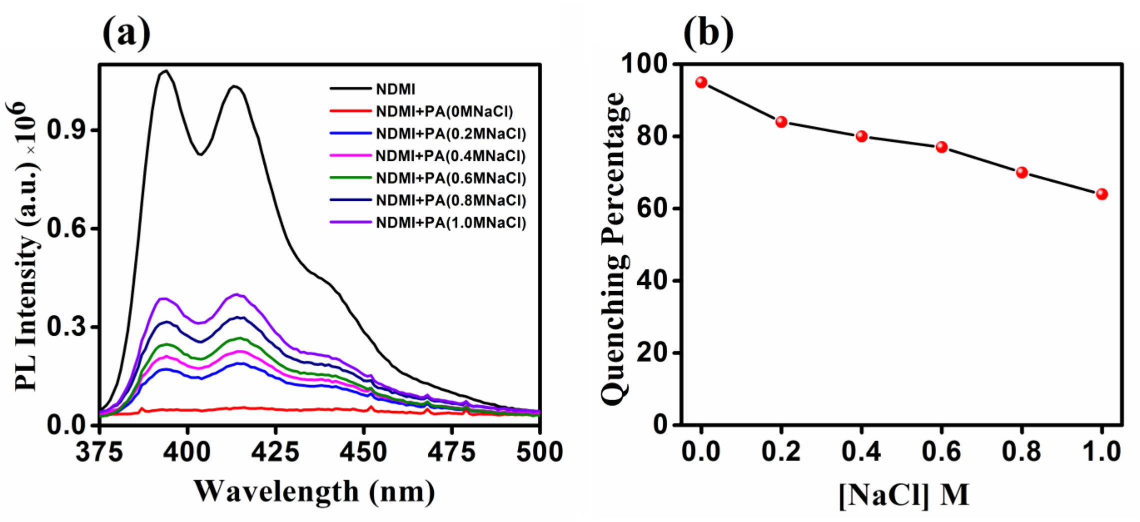

Figure A5.9 (a) Fluorescence quenching of NDMI (16.7 μM) with PA (67 μM) in salt solutions of different concentrations. (b) The effect of ionic strength on the quenching efficiency.

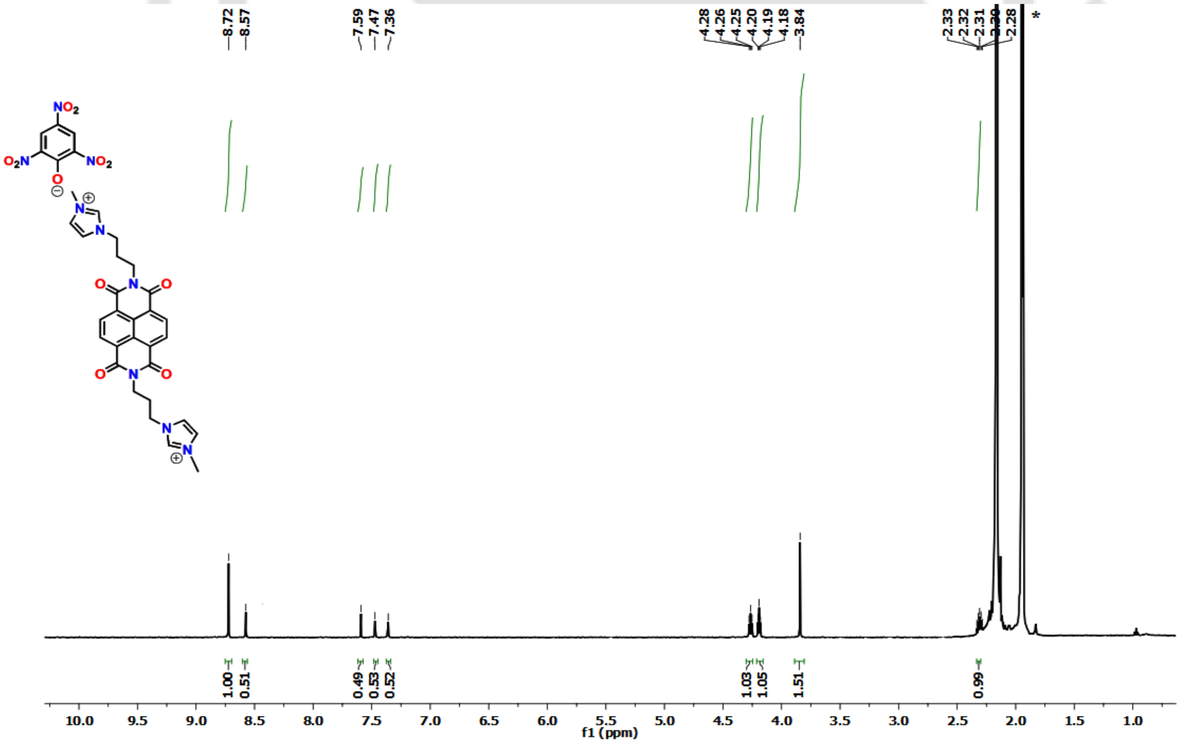

Figure A5.10 ^{1}H NMR (CD_3CN, 600 MHz) spectra of NDMI-PA complex.

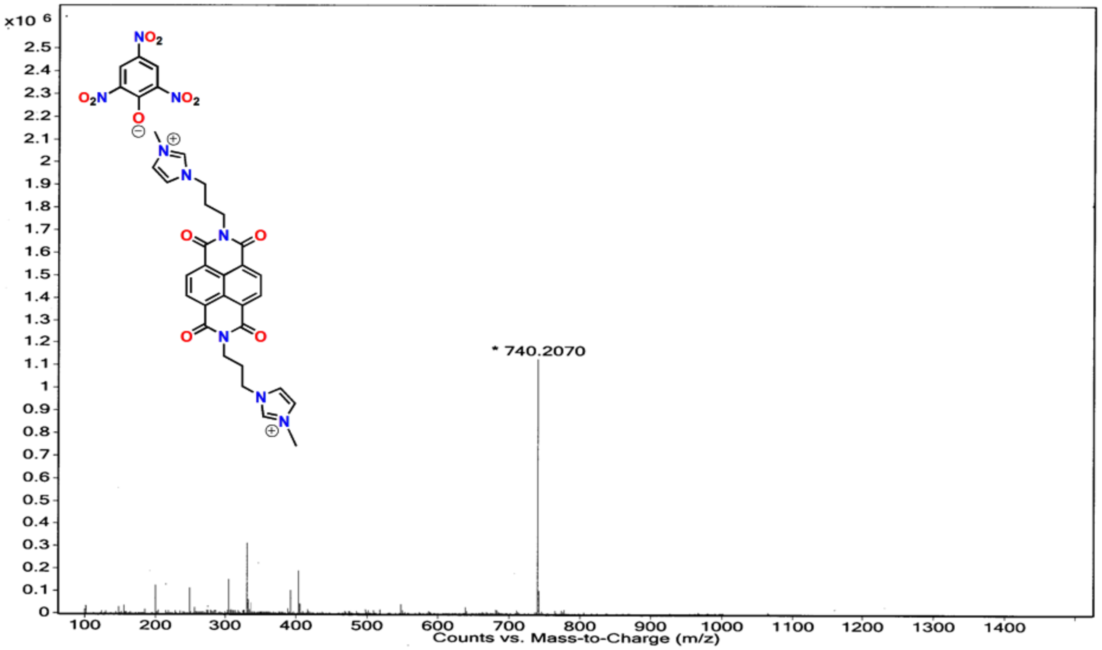

Figure A5.11 ESI-MS spectra of NDMI-PA complex.

Electrochemical Calculations:

The detailed calculations are summarized as follows:

The LUMO energy level was estimated based on the following equation

E_{LUMO} (eV)=–($E_{\mathrm{red\ onset}}$+4.8)=–($E_{\mathrm{pc\text{-}onset}}$–$E_{\mathrm{Fc}}$+4.8)

E_{Fc}=0.13+0.055/2=0.093 eV

The HOMO level was calculated based on the optical band gap obtained from absorption onset measurements

E_{LUMO}=–(4.8+$E_{\mathrm{pc\text{-}onset}}$–$E_{\mathrm{Fc}}$)=–(4.8–0.75–0.093)=–3.95 eV

($E_{\mathrm{g}}^{\mathrm{optical}}$=1240/$\lambda_{\mathrm{opt\text{-}onset}}$ eV=1240/395 eV= 3.14 eV)

E_{HOMO}=E_{LUMO}–$E_{\mathrm{g}}^{\mathrm{optical}}$=–3.95 –3.14=–7.09 eV

E_{g}=E_{LUMO}–E_{HOMO}=3.14 eV

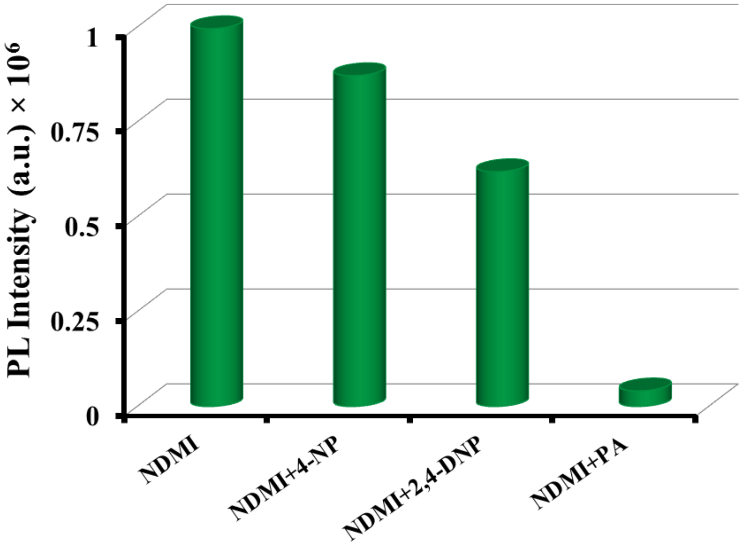

Figure A5.12 Fluorescence quenching observed in NDMI (67 μM) with different nitrophenols (16.7 μM).

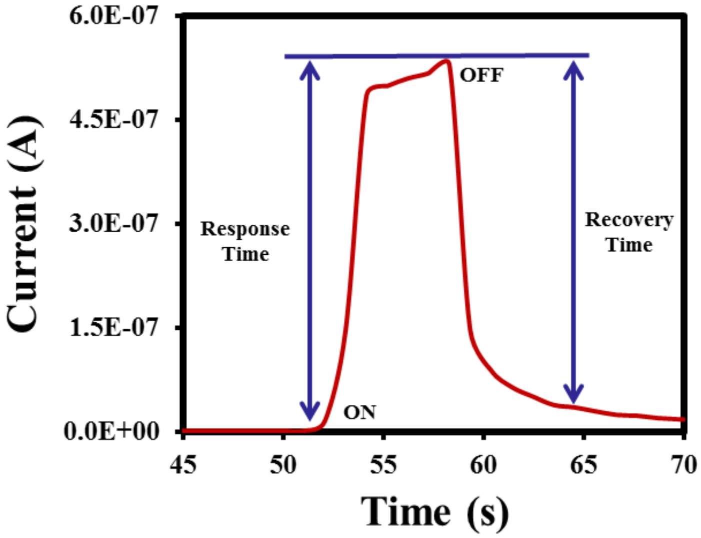

Figure A5.13 Response and recovery time of NDMI fabricated sensor device.

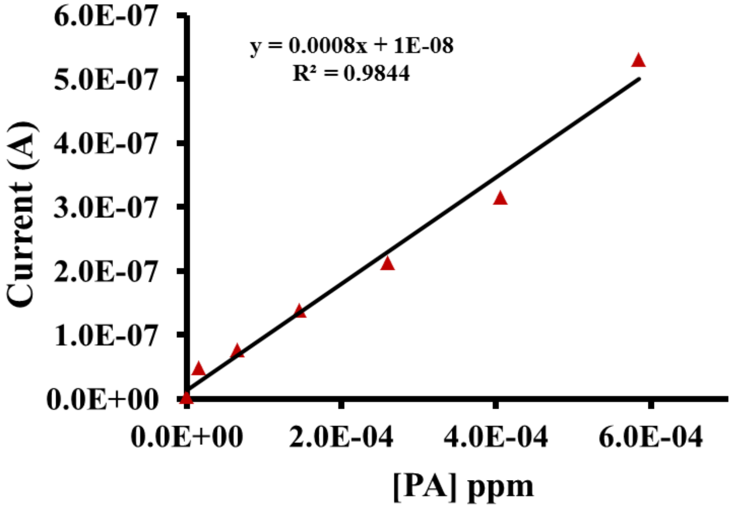

Figure A5.14 Detection limit plot for PA in vapor phase.

Table A5.2. Comparative study with various types of PA probes reported recently.

Publication	**Sensing material**	**Sensing mechanism**	**Mode of detection**	**LOD (vapor mode)**
Present Work	***Single crystalline naphthalene diimide***	***π-π stacking, electron transfer and dipole charge/Coulombic interactions***	***Solution and vapor phase***	***2.92 ppt***
ACS Appl. Mater. Interfaces **2015**, *7*, 26968.	Conjugated polymer nanoparticles	PET, RET and doping	Solution, solid and vapor phase	Not reported
J. Mater. Chem. C **2015**, *3*, 11081.	Layer by layer polymers	Electron transfer	Vapor phase	6 ppb
ACS Appl. Mater. Interfaces **2016**, *8*, 5758.	Carbon dots	Variation in charge career density	Solution phase	-
J. Mater. Chem. A **2016**, *4*, 4161.	Carbon nanoparticles	PET and FRET	Solution phase	-
Cryst. Growth Des., **2015**, *15*, 4627.	Metal-organic framework	PET and FRET	Solution phase	-

ACS Sens., **2016**, *1*, 636.	Imprinted polymer	Charge-transfer	Solution phase	-
J. Am. Chem. Soc., **2015**, *137*, 15276.	TPE metallacycles	Steady-state interactions	Solution phase	-
Chem. Commun., **2015**, *51*, 8300.	Zn(II) metal-organic frameworks	PET and FRET	Solution phase	-
Nanoscale **2015**, *7*, 15413.	Polymer dots	PET and hydrogen bonding	Solution phase	
Analyst **2016**, *141*, 1091.	Ag nanoclusters	Electron transfer and FRET	Solution phase	-
Chem. Commun., **2015**, *51*, 7207.	Conjugated polyelectrolyte	Ground state electron transfer and RET	Solution and solid phase	-
J. Phys. Chem. B **2016**, *120*, 5063.	Amine molecular cages	Charge-transfer	Solution phase	-
J. Am. Chem. Soc., **2016**, *138*, 3302	Covalent organic frameworks	Not shown	Solution phase	-

The thesis entitled "***Design and Fabrication of Rylene Diimide Based Active Materials, Devices and Applications***" is divided into 5 chapters. After the introductory background in Chapter, Chapter 2 discussed the application of N, N'-bis(cyclohexyl)naphthalene diimide (NDI-CY2) derivative in Organic Field Effect Transistors (OFETs) showing the effect of inorganic/polymeric dual dielectric layers. Chapter 3 discussed the development of a new conjugated naphthalene diimide, N, N'-bis(methylcyclohexane)naphthalene diimide (NMeCy2) derivative and its application in the field of OFETs using trilayer dielectric system. Chapter 4 described the synthesis of a conjugated histidine functionalized Perylene Diimide (PDI-HIS) derivative and its application in the detection of ammonia (NH_3) vapors using two electrode device. Chapter 5 deals with the synthesis of a new conjugated N, N′-bis(3-imidazolium-1-ylpropyl)-naphthalenediimide diiodide (NDMI) derivative and its application in detection of potent nitroexplosive picric acid (PA) both in aqueous and in vapor phase. Chapter 5 also highlighted the development of electronic prototype for visual on-site detection of nitroexplosive PA vapors under exceptionally realistic conditions.

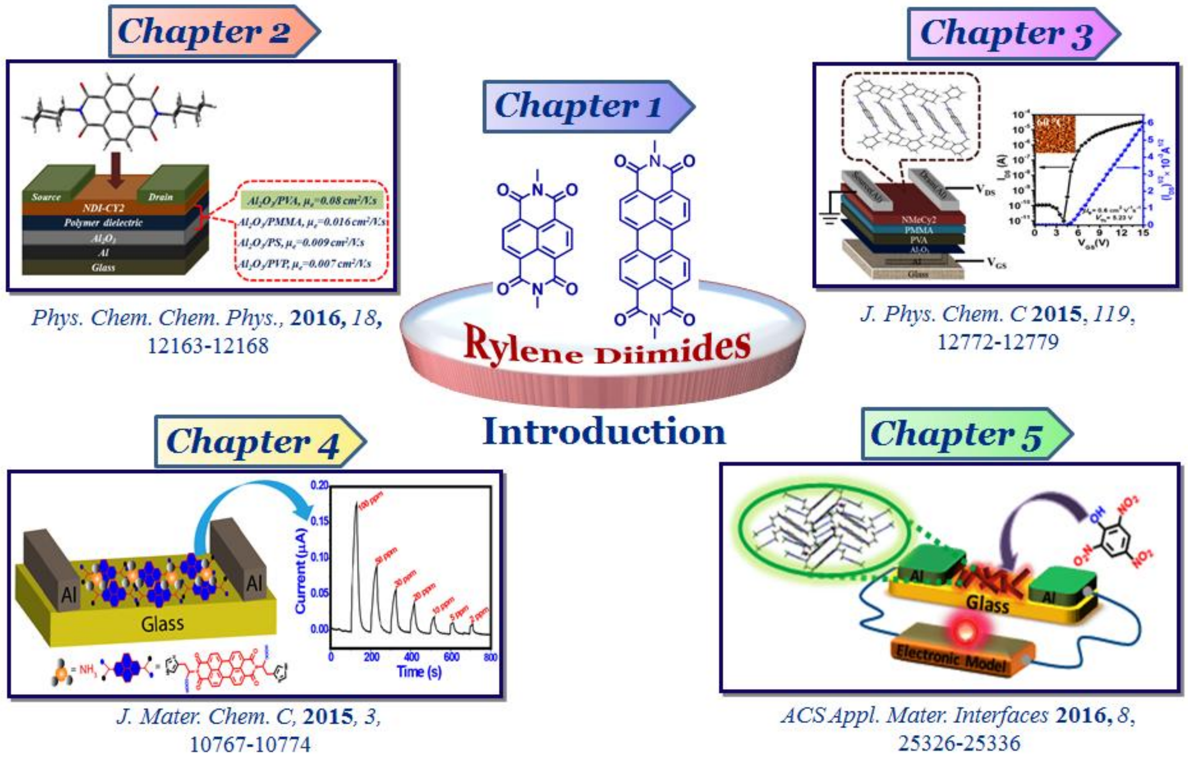

Phys. Chem. Chem. Phys., **2016**, *18*, 12163-12168

J. Phys. Chem. C **2015**, *119*, 12772-12779

J. Mater. Chem. C, **2015**, *3*, 10767-10774

ACS Appl. Mater. Interfaces **2016**, *8*, 25326-25336

1. Dey, A.; **Kalita, A.**; Iyer, P. K. High Performance n-channel Organic Thin Film Transistor Based on Naphthalene Diimide. *ACS Appl. Mater. Interfaces* **2014**, *6*, 12295-12301.

2. **Kalita, A.**; Subbarao, N. V. V.; Iyer, P. K. Large-Scale Molecular Packing and Morphology-Dependent High Performance Organic Field-Effect Transistor by Symmetrical Naphthalene Diimide Appended with Methyl Cyclohexane. *J. Phys. Chem. C* **2015**, *119*, 12772-12779.

3. **Kalita, A.**; Hussain, S.; Malik, A. H.; Subbarao, N. V. V.; Iyer, P. K. Vapor Phase Sensing of Ammonia at the Sub-ppm Level Using Perylene Diimide Thin Film Device. *J. Mater. Chem. C* **2015**, *3*, 10767-10774.

4. Malik, A. H.; Hussain, S.; **Kalita, A.**; Iyer, P. K. Conjugated Polymer Nanoparticles for the Amplified Detection of Nitroexplosive Picric Acid on Multiple Platforms. *ACS Appl. Mater. Interfaces* **2015**, *7*, 26968-26976.

5. Dey, A.; Singh, A.; **Kalita, A.**; Das, D.; Iyer, P. K. High Performance, Low Operating Voltage n-type Organic Field Effect Transistor based on Inorganic-Organic bilayer Dielectric System. *J. Phys. Condens. Matter* **2016**, *704*, 012017.

6. **Kalita, A.**; Dey, A.; Iyer, P. K. The Effect of Inorganic/Organic Dual Dielectric Layers on the Morphology and Performance of n-channel OFETs. *Phys. Chem. Chem. Phys.*, **2016**, *18*, 12163-12168.

7. **Kalita, A.**; Hussain, S.; Malik, A. H.; Barman, U.; Goswami, N.; Iyer, P. K. Anion-Exchange Induced Strong π-π Interactions in Single Crystalline Naphthalene Diimide for Nitroexplosive Sensing: An Electronic Prototype for Visual On-Site Detection. *ACS Appl. Mater. Interfaces* **2016**, 8, 25326-25336.

8. Malik, A. H; **Kalita, A.**; Iyer, P. K. Development of Well Preserved, Substrate-Versatile Latent Fingerprints by Aggregation Induced Enhanced Emission Active Conjugated Polyelectrolyte. *ACS Appl. Mater. Interfaces* **2017**, *9*, 37501-37508.

1. Presented poster in ***"Research Conclave 2017"*** organized by Students Academic Board (SAB), Indian Institute of Technology Guwahati during 16-19 March, 2017.

2. Attended ***"3rd National Workshop on NEMS/MEMS and Theranostics Devices"*** held at Centre for Excellence in Research and Development of Nanoelectronic Theranostic Devices under the aegis of Centre for Nanotechnology, Indian Institute of Technology Guwahati during 21-23 February, 2017.

3. Attended the full agenda of ***"ACS on Campus"*** organized at IIT Guwahati on 16 January 2017.

4. Presented poster in ***"International Conference on Functional Material, ICFM-2016"*** organized by Materials Science Centre, IIT Kharagpur during 12-14 December, 2016.

5. Delivered an oral talk in ***"National Conference on Recent Advances in Nonoscience and Nanotechnology, NCRANNT-2016"*** held at Department of Nanotechnology, NEHU, Shillong during 8-9 September, 2016.

6. Presented poster in ***"Reflux-2016"*** held at Department of Chemical Engineering, IIT Guwahati during 25-27 March, 2016.

7. Presented poster in ***"27th Materials Research Society of India (MRSI) Symposium on Advanced Materials for Sustainable Applications"*** held at CSIR-NEIST, Jorhat during 18-21 February, 2016.

8. Presented poster in ***"4th International Conference on Advanced Nanomaterials and Nanotechnology, ICANN-2015"*** conducted by Centre for Nanotechnology, Indian Institute of Technology Guwahati during 08-11 December, 2015.

9. Participated in ***"68th Annual Session of Indian Institute of Chemical Engineers, CHEMCON 2015"*** held at Indian Institute of Technology Guwahati during 27-30 December, 2015.

10. Participated in ***"Research Conclave 2015"*** organised by Students Academic Board (SAB), Indian Institute of Technology Guwahati during 23-26 March, 2015.

11. Presented poster in ***"National Conference on Advances in Polymer Science and Technology, APST-2015"*** organized by Asian polymer Association: North East Forum (APA:NEF) and IASST, Guwahati during 13 March, 2015.
12. Attended ***"2-Day Familiarization Workshop on Nanofabrication Technologies (INUP)"*** held at Tezpur University during 25-26 April, 2015 funded by the Dept of Electronics and Information Technology (DeitY), the Ministry of Communication and Information Technology (MCIT), Govt. of India.
13. Presented poster in ***"3rd International Conference on Advanced Nanomaterials and Nanotechnology, ICANN-2013"*** conducted by Centre for Nanotechnology, Indian Institute of Technology Guwahati during 1-3 December, 2013.